

Coherent Control  
of Electron Spin Dynamics  
in Nano-Engineered  
Semiconductor Structures



University of Groningen  
**Zernike Institute  
for Advanced Materials**

Zernike Institute PhD thesis series 2011-18

ISSN: 1570-1530

ISBN: 978-90-367-5106-3 (PRINTED VERSION)

ISBN: 978-90-367-5105-6 (ELECTRONIC VERSION)

The work described in this thesis was performed in the research group Physics of Nanodevices of the Zernike Institute of Advanced Materials at the University of Groningen, the Netherlands. It was supported with funding from the Zernike Institutes status as National Research Centre, and did profit from collaboration with projects funded through a Vidi grant from the Netherlands Organization for Scientific Research (NWO) and the national NanoNed and NanoLab NL initiatives.

Printed by: Proefschriftmaken.nl || Uitgeverij BOXPress, Oisterwijk

Cover design: Kateryna Naumova, <http://naumova.net>

Photo: Sergii Denega, <http://denega.net>

RIJKSUNIVERSITEIT GRONINGEN

Coherent Control  
of Electron Spin Dynamics  
in Nano-Engineered  
Semiconductor Structures

**Proefschrift**

ter verkrijging van het doctoraat in de  
Wiskunde en Natuurwetenschappen  
aan de Rijksuniversiteit Groningen  
op gezag van de  
Rector Magnificus, dr. E. Sterken,  
in het openbaar te verdedigen op  
maandag 3 oktober 2011  
om 12:45 uur

door

Sergii Zinoviyovych Denega

geboren op 24 juni 1983  
te Khmelnytskyi, Oekraïne

Promotor: Prof. dr. ir. C. H. van der Wal

Beoordelingscommissie: Prof. dr. J. A. Folk  
Prof. dr. B. Koopmans  
Prof. dr. ir. P. H. M. van Loosdrecht

*...to my parents and family*



# Contents

<b>1</b>	<b>Introduction</b>	<b>1</b>
1.1	Electron spin and polarization of light . . . . .	2
1.2	Motivation . . . . .	3
1.3	Outline of this thesis . . . . .	11
<b>2</b>	<b>Optical excitation and detection of electron spin coherence</b>	<b>15</b>
2.1	Introduction . . . . .	16
2.2	Optical transitions and selection rules . . . . .	16
2.3	The Kerr effect . . . . .	22
2.4	Balanced polarization bridge . . . . .	25
2.5	Measurement setup . . . . .	28
2.6	Measurement of the spin dephasing time ( $T_2^*$ ) . . . . .	31
2.7	Summary . . . . .	33
<b>3</b>	<b>Suppressed spin dephasing for 2D and bulk electrons in GaAs wires due to engineered cancellation of spin-orbit interaction terms</b>	<b>35</b>
3.1	Introduction . . . . .	36
3.2	Experimental realization . . . . .	36
3.3	Signatures of spin dephasing anisotropy for 2DEG and bulk electrons	38
3.4	Summary of numerical simulations . . . . .	43
3.5	Effect of external magnetic field on spin dephasing anisotropy . .	43
3.6	Effect of temperature and pump power on spin dephasing anisotropy	44
3.7	Conclusions . . . . .	46
<b>4</b>	<b>Spin-dephasing anisotropy for 2D electrons in a diffusive quasi-1D GaAs wire</b>	<b>49</b>
4.1	Introduction . . . . .	50
4.2	Method . . . . .	52

4.3	Results and discussion . . . . .	53
4.4	Conclusions . . . . .	57
<b>5</b>	<b>Spin-dephasing anisotropy for electrons in a quasi-1D GaAs wire without quantum confinement</b>	<b>59</b>
5.1	Introduction . . . . .	60
5.2	Spin-orbit coupling . . . . .	61
5.3	Method . . . . .	62
5.4	Results . . . . .	64
5.5	Conclusions . . . . .	70
<b>6</b>	<b>Ultrafast mapping of optical polarization states onto spin coherence of localized electrons in a semiconductor</b>	<b>73</b>
6.1	Introduction . . . . .	74
6.2	Experimental realization of bijective mapping . . . . .	75
6.3	Robustness of spin preparation . . . . .	79
6.4	Repeated preparation of a spin state . . . . .	81
6.5	Conclusions . . . . .	82
<b>7</b>	<b>Optical time-resolved study of the Landé <math>g</math> factor in <math>n</math>-doped GaAs materials</b>	<b>85</b>
7.1	Introduction . . . . .	86
7.2	Results . . . . .	88
7.3	Conclusions . . . . .	95
	<b>Summary</b>	<b>99</b>
	<b>Samenvatting</b>	<b>101</b>
	<b>List of publications</b>	<b>103</b>
	<b>Curriculum vitae</b>	<b>105</b>
	<b>Acknowledgements</b>	<b>107</b>

# Chapter 1

## Introduction

## 1.1 Electron spin and polarization of light

The electron spin and polarization of light belong to the most fundamental concepts that are used in the physical description of materials and radiation, and both have been intensively investigated ever since their discovery. Nevertheless, our understanding of the behavior spin and radiation –and their interaction– in materials and devices is far from complete, and modern technology does not yet use the full potential they offer. This thesis presents research that is part of a broad field that simultaneously aims at improving this fundamental understanding and realizing proof-of-principle demonstrations of new control schemes and functionalities that better exploit the electron spin and light polarization.

As often happens, the formal description and the name for spin and light polarization came later than the first experiments which could not be explained without these concepts. The name "polarization" for light was introduced by Etienne Louis Malus in 1808, while the first scientific description of an effect due to light polarization (double refraction) was already published by Danish mathematician Rasmus Bartholin in 1669 [1]. The current understanding of the phenomenon is formalized together with the electromagnetic theory of light. The polarization of electromagnetic waves is very widely used. However, optical communication mostly still uses the detection of light intensity, regardless its polarization. This means that in the ultimate limit of such an approach we can transmit one bit of information with one photon successfully transmitted through a network. It is a great achievement compared to what man could do a hundred years ago, but if the polarization states of the photon would be included, each transmitted photon could carry as many bits as one would be able to discriminate different polarization states. This can give a huge increase in the throughput of the network without an increase in the modulation frequencies.

The concept of spin was proposed by Uhlenbeck and Goudsmit [2, 3] in 1925, while the first experiments which needed the spin for their explanation include the observation of the anisotropic magnetoresistance [4] in 1857, and the famous experiment by Stern and Gerlach [5] in 1922. In the widespread information processing with electronics, the role of spin in electrical signals is similar to the role of polarization in optical signals. Here, information is mostly associated the presence or absence of charge or an electron current, regardless of its spin. The utilization of the intrinsic property of electron spin as being a superposition of two states would upscale one bit of useful information for a transmitted electron to a continuum. The practical limitation would be set by the ability of the detector

to discriminate between the different superpositions of spin states.

The quantum description of the interaction of light with matter connects these two concepts. An optical photon in a coherent superposition of polarization states is highly suited for transferring quantum information, while it can also have a selective coupling to the different spin states of conduction electrons in solid state. Altogether this makes this pair (optical photons and electron spins in solid state) a very promising candidate for the realization of new information processing schemes that have been proposed, such as spintronics and quantum information processing [6].

## 1.2 Motivation

The research presented in this thesis aimed at improving the understanding of, and abilities to control the evolution of spin ensembles in solid state systems. Various fundamental aspects of spin ensemble evolution like dephasing, decoherence, relaxation, diffusion and drift are addressed. All experiments use GaAs or GaAs/AlGaAs-based semiconductor materials with optical control and readout. These GaAs-based materials provide interesting test systems since they combine the highest available material quality, a very advanced level of possibilities for device processing and engineering, and strong optical transitions across the semiconductor bandgap that obey clear selection rules with respect to optical polarization and spin.

Such research with GaAs materials has for this reason already a rich history that goes back to the early days of advanced semiconductor processing about 50 years ago. Optical studies addressing spin were already carried out from the start, with very impressive results that were for example reviewed in the authoritative (and still widely cited) book *Optical Orientation* in 1984 [7]. Around 1995, the development [8] of the pulsed optical technique Time-Resolved Kerr Readout (TRKR, based on the magneto-optical Kerr effect) led to the discovery [9] that GaAs materials at the metal-insulator transition (due to a level of  $n$ -doping of about  $2 \times 10^{16} \text{ cm}^{-3}$ ) could show electron spin dephasing times in excess of 100 ns (about 2 orders of magnitude longer than reported till then). Around the same time new schemes for spintronics and quantum information processing were discovered [10]. Together, this stimulated further research aimed at understanding how engineering and controlling the electronic states and electron motion in GaAs materials and device structures could be used for applying coherent electron spin dynamics with a long coherence time, or even spin manipulation via interactions

with the material [10].

The work that is reported in this thesis aimed at answering questions and realizing proof-of-principle demonstrations at the forefront of this field. The mentioned TRKR technique is central in most of the experiments. In the course of this work, several experiments led to observations that pointed out that the fundamental understanding of the underlying physical mechanisms was –despite the large body of earlier work– in fact incomplete, or even to observations that were in conflict with the established descriptions. On these occasions the reported work aimed at characterizing and understanding these new observations. The remainder of this Section summarizes the questions that underly the work that is reported in this thesis. We used a variety of materials and device structures, with electron ensembles in the form of free bulk populations (3D) and localized donor electrons (0D). We also used materials with a two-dimensional electron gas (2DEG) in a quantum well, that were for some studies processed into quasi-1D wire structures.

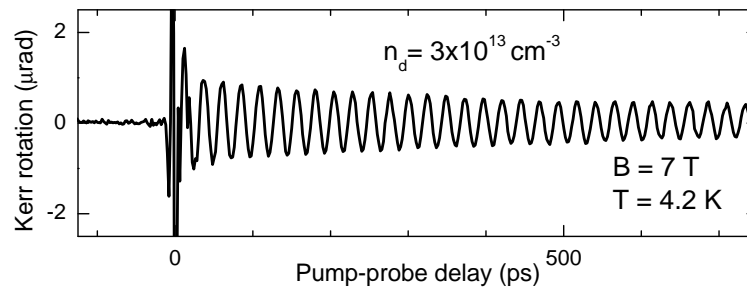


**Figure 1.1:** Typical example of a Time-Resolved Kerr Rotation trace, with Kerr rotation angle  $\theta_K$  (representing electron spin orientation) as a function of pump-probe delay  $t$ . The oscillatory character directly reflects spin precession about the applied magnetic field.

### Application of the TRKR technique

The mentioned Time-Resolved Kerr Readout (TRKR) technique is a stroboscopic method that directly measures the electron spin orientation along a certain direction with a time-resolution (about 1 ps) that is smaller than the timescales that govern the electron spin dynamics in semiconductors. The relevant processes here include spin precession in a magnetic field, spin dephasing, and electron-hole recombination. It is an optical pump-probe method with picosecond laser pulses that are tuned near resonance with transitions across the bandgap. The pump

pulse induces electron spin orientation along a certain direction in a sample. After a controlled delay  $t$  a probe pulse is reflected on this sample and the amount of polarization rotation (angle  $\theta_K$ ) that occurs during this reflection event is a direct measure for the amount of spin orientation at that moment. Typical results of such a TRKR experiment are shown in Fig. 1.1, and results of  $\theta_K$  as a function of delay  $t \geq 0$  are typically fit with the equation

$$\theta_K = A \exp\left(-\frac{t}{\tau}\right) \cos\left(\frac{|g|\mu_B B}{\hbar}t + \phi\right). \quad (1.1)$$

In this expression  $A$  is the initial amplitude,  $|g|$  is the g factor of the electrons,  $\mu_B$  is the Bohr magneton,  $B$  is the magnitude of the external magnetic field,  $\hbar$  is the reduced Planck constant, and  $\tau$  is the signal decay time. The cosine factor directly reflects spin precession about the external magnetic field at the angular Larmor frequency  $|g|\mu_B B/\hbar$ , with an initial phase  $\phi$ .

The format of TRKR signals as in Eq. 1.1 can be used to illustrate the potential of this method, while highlighting at the same time examples where fundamental understanding appeared less complete than we anticipated at the onset of this thesis work. There is in principle a wide range of knowledge available about the variation of  $|g|$  and  $\tau$  as a function of material composition, quantum confinement, kinetic energy, donor concentration, etc. This suggests that analysis of the observed values for  $|g|$  or  $\tau$  can be used to obtain time-resolved information about –for example– the location and displacement of electron ensembles in device structures made of layers with different g factors, such as GaAs/AlGaAs heterostructures. Our attempts along these lines were successful [11, 12], but also pointed to gaps in our basic understanding.

A first example of a fundamental aspect that is not fully understood is the initial phase  $\phi$  of the electron spin precession in Eq. 1.1. The conventional description of the TRKR method states that it prepares and detects spin orientation along the propagation direction of the laser pulses [9], which is typically identical for the pump and probe beams in a TRKR experiment. However, fitting of experimental results often requires using a non-zero value for the parameter  $\phi$ . This is widely applied, while it is often not clear why the amount of spin orientation does not show a maximum at the moment of preparation ( $t = 0$ ). We could extend such initial observations of nonzero  $\phi$  values to a study in which we could fully control arbitrary  $\phi$  values, in work on ensembles of localized electrons in GaAs samples with Si doping at very low concentration (donor-bound electron ensembles,  $n_{Si} < 10^{15} \text{ cm}^{-3}$ ).

A second example where the field did not yet provide a conclusive picture concerns the spin dephasing time for localized electrons in this type of material. The experimental reports differ from each other by as much as two orders of magnitude [13] and this indicates that it is for many experiments difficult to point out which electrons (free photo-induced electrons versus localized electrons) dominate the signal, and that results can depend on the probing method. With TRKR we looked into this with photon-energy and pump-intensity dependant measurements of the spin dephasing time.

A third aspect that turned out to be not fully established concerns the value  $|g|$  of the  $g$  factor in Eq. 1.1. For example, for bulk GaAs, nearly all of the established literature and textbooks report  $-0.44$  for the GaAs  $g$  factor, and the fact that it can obtain values closer to zero as a result of band filling, quantum confinement or excess kinetic energy. However, we observed with TRKR values as negative as  $-0.49$  in very pure GaAs samples with Si doping at  $n_{Si} = 2 \times 10^{16} \text{ cm}^{-3}$ , and could provide new insights for spin dynamics in this material at the metal-insulator transition.

Despite the fact that our TRKR studies forced us to look into these various fundamental questions, our work also generated proof-of-principle results which are potentially valuable for the applied fields of spintronics, and the emerging science of quantum information processing. These studies are further introduced below here.

### **Suppressed spin dephasing for mobile electrons in wire structures**

The first part of this thesis presents experiments and numerical simulations on suppressed spin dephasing for mobile electron spin ensembles in GaAs-based device structures. Spin dephasing for mobile electrons in GaAs is mainly due to spin-orbit (SO) interaction [14], which couples the spin precession of an electron to its motion. We used a GaAs/AlGaAs heterostructure, for which the strength of this spin-orbit interaction can be highly anisotropic with respect to the direction of electron motion. Interestingly, it can be engineered at a value close to zero for electrons that move along the  $[110]$  crystal direction. We investigated whether this could result in suppressed spin dephasing for wires that were nano-fabricated along this crystal direction (see Fig. 1.2). We considered the case of quasi-ballistically confined structures where the width of the wire is smaller than the electron's mean free path and the spin precession length, but larger than the width that gives strong quantum confinement. Whether electron ensembles in this regime (with frequent random momentum scattering within the ensemble)

could show suppressed spin dephasing was an open question.

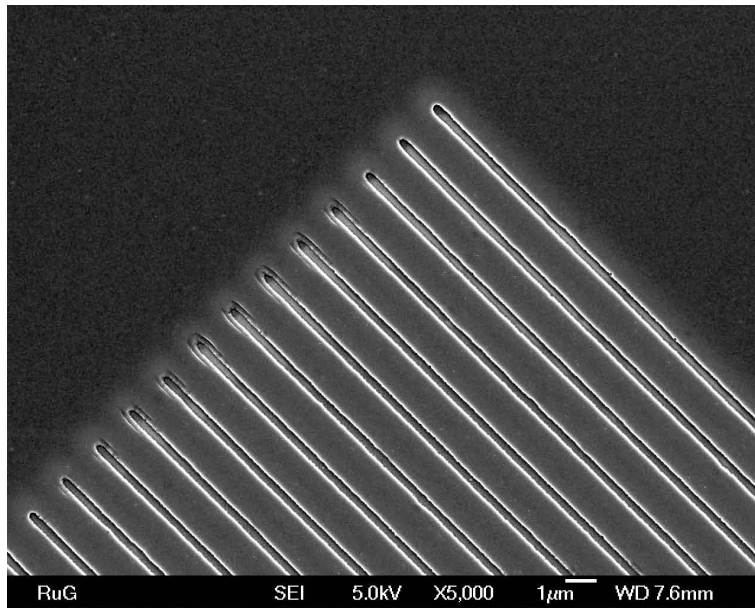


**Figure 1.2:** (a) Scanning electron microscope image of a GaAs/AlGaAs heterostructure with parallel wires of about  $1 \mu\text{m}$  width processed in its top layer. Such samples were used for investigating a suppression of spin dephasing for mobile electrons in wires structures.

Spin-orbit interaction occurs when an electron is moving in an electric field, which, due to Lorentz coordinate transformation, acts on the electron spin as an effective magnetic field. The nett effect for materials with a centrosymmetric crystal structure averages out, while the lack of such symmetry (typically the case for III-V semiconductors with a zincblende crystal structure) complicates the issue. In a material like GaAs it results in the presence of SO interaction which is determined by the crystallographic symmetries (Dresselhaus SO term [15]). If the band structure of the sample is modified such that its inversion symmetry is broken, an additional SO term will arise (Rashba SO term [16]). This occurs for example at the interface between two different layers, and is therefore relevant for quantum well systems. Together, these effects give an anisotropic SO interaction, which results in an enhanced dependency of spin precession on the motion of an electron.

Within this picture the random motion of electrons in an ensemble leads to rapid dephasing of the ensemble-averaged spin orientation. This is known as the D'yakonov-Perel' (DP) spin dephasing mechanism [17]. Wires with strong quan-

tum confinement, which allows electrons to move only in one direction, would suppress this DP dephasing, but the technical realization of such wires is in practice of little use since a weak level of disorder leads to strong electron localization. Our experimental study successfully demonstrated that the suppressed spin dephasing persists for mobile electrons with quasi-ballistic confinement. In this case, there is no quantization of the  $k$  vector in the transverse wire direction, but there is much more frequent scattering for electrons moving in this direction (on the system's edges) than for electrons moving along the wire. We studied the limits of this effect and possible implications for mesoscopic spin transport. In addition, we studied the difference between quasi-ballistic confinement for 2DEG and bulk electron ensembles. We support our experimental studies with numerical simulations.

These results can be extended to any other material with lack of inversion symmetry in the crystal structure, and are thus valuable for a wider scope of research in semiconductor spintronics.

### **Spin preparation and detection for localized electron spins**

The second topic addressed in this thesis is related to obtaining fully quantum coherent behavior for the interaction between electron spins and optical preparation and detection pulses. A roadmap for the field that studies quantum computation [6] discusses several possible implementations, and systems that have a natural way for coupling optical photons to stationary quantum bits (qubits) have an advantage if one aims to combine quantum computation with quantum communication. Besides the typical examples for this from the field of atomic physics, there are also several solid state systems that support a direct link between the quantum states of an electron spin and the polarization state of an absorbed or emitted photon. We focused on a few of the basic requirements in a research line that aims to realize quantum information processing with optical photons as mediators of information and electron spins as quantum registers. As for classical computation, these basic requirements concern the ability to prepare, manipulate, and detect the state of a computational bit fast and reliably [18].

In our study the stationary qubit was formed by the spin state of a donor-bound electron, localized at a Si donor site in low-doped  $n$ -GaAs ( $D^0$  system). These were addressed as a homogeneous ensemble. Earlier studies already demonstrated a long spin coherence time ( $> 20 \mu\text{s}$ ) for this system, in combination with the ability for ultrafast all-optical spin manipulation [19, 20, 21, 22, 23]. However, the spin preparation and spin detection were implemented via optical pumping,

photo-luminescence or spectroscopic techniques which are relatively slow. Preparation and detection with picosecond laser pulses was believed to be very difficult, given the complexity of the optically excited state that is addressed for such optical interactions. This optically excited state has several sub-levels with energy splittings that are smaller than the spectral width of short laser pulses, and this could hamper coherent spin preparation. However, our attempts to characterize the spin dephasing times for  $D^0$  systems with TRKR showed robust spin preparation and detection, and this initiated more detailed studies in this direction.

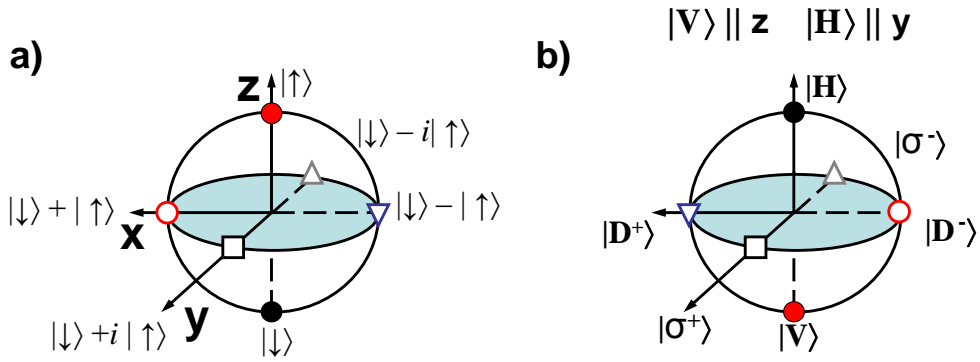


**Figure 1.3:** (Color) Bijective mapping of optical polarization states onto spin states. (a) Bloch-sphere representation for the electron spin. (b) Poincaré-sphere representation for optical polarization states. The common symbols in (a) and (b) illustrate the bijective mapping that was operated during the preparation of  $D^0$  spin states with picosecond laser pulses.

In this research, we focused on finding the right conditions for robust picosecond spin preparation and detection, with a bijective mapping of the quantum states of optical polarization onto  $D^0$  spin states and *vice versa* (see Fig. 1.3). Earlier work by Kosaka *et al.* had already explored this concept for non-equilibrium photo-electrons, where the coherence time for the electron spin was limited by electron hole recombination [24, 25]. We explored how this concept could be extended to spins of localized donor electrons in GaAs, which can show much longer coherence times. In particular, earlier work on  $D^0$  systems already demonstrated a ratio between the coherence time [22] and manipulation time [21] in excess of  $10^7$ . Our work added picosecond preparation and detection to the available operations for  $D^0$  spins. We thus expand a set of tools with a ratio between coherence time and operation time in excess of  $10^7$ . Achieving such a high ratio is one of

the essential steps on the roadmap for quantum computation research [6], since this is essential for investigating quantum error correction schemes. While our work thus brings us further on this road, we could not yet confirm that our new preparation and detection scheme is equivalent to a fast projective measurement, as is assumed in much of the theory for quantum error correction [18].

### Time-resolved study of the Landé g factor

The third and final part of this thesis concerns a detailed study of the earlier mentioned observation of g factor values in bulk GaAs as negative as  $-0.49$ , while most of the established literature assumes  $g \geq -0.44$ . The value  $-0.44$  was reported for low temperature (4.2 Kelvin) and low electron density by Weisbuch *et al.* (Ref. [26]) from 1977, and most references to the GaAs g factor value build on this seminal work.

The g factor governs the frequency of spin precession (angular Larmor frequency  $\omega_L$ ) in an external magnetic field  $B$ . For a free electron the g factor value is very close to 2 (in fact  $2.0023193043622$  with an uncertainty of  $1.5 \cdot 10^{-12}$ ). For electrons in a material it is altered by spin-orbit interaction. In the case of GaAs conduction electrons this is a strong effect, which even changes sign of the g factor (leading to the opposite direction of spin precession). A closer look reveals that the g factor does not have a fixed single value, but that it can be anisotropic [27, 28] and that it varies as a function of parameters like temperature and photo excitation density [29]. With the development of new time-resolved techniques it became possible to study the g factor in more detail [30], but the field is still not showing concensus on the values of this material parameter.

We used TRKR for a *time-resolved* analysis of the g factor values, as its value may change during kinetic energy relaxation of an electron. We also observe a connection between the background doping concentration and g factor values, and compared studies on *n*-GaAs samples where the donor states form a band with ultra-pure GaAs sample with extremely low levels of intentional *n*-doping. For all these materials we investigated the influence of the experimental conditions (power of optical pumping, laser wavelength etc.) on the apparent value of the g factor. This work showed that the g factors can indeed have a drifting value during transient TRKR signals, and that the values  $-0.49 < g < -0.44$  only occur for low-energy electrons in samples where the donor states form a band.

## 1.3 Outline of this thesis

The presentation of this research is organized as follows. *Chapter 2* gives a summary of the physical concepts that play a role, such as the optical selection rules for GaAs. This chapter also presents the experimental methods and the setup for TRKR measurements that was used in all of the experiments.

*Chapters 3* till *5* are devoted to the experimental and numerical studies of suppressed spin dephasing for mobile electrons in 2DEG and bulk GaAs wire structures. *Chapter 3* reports the experimental studies. The work compares the spin dephasing time for electrons in wires oriented along different crystal directions and for unconfined electrons in the same material, in external magnetic fields that range from 0 to 7 Tesla. The results show a suppressed spin dephasing for wires along the [110] crystal direction at low fields. Notably, the effect was observed both for electrons in a 2DEG layer and for photo-excited electrons in a bulk layer.

*Chapter 4* describes results from a numerical study of the suppressed spin dephasing for 2DEG electrons in quasi-1D wires. The model assumes 2DEG electrons which are laterally confined in an elongated strip of 1  $\mu\text{m}$  width and 200  $\mu\text{m}$  length (similar dimensions as the wires that were studied in the experiment). The electrons freely move inside the strip, and reflect on the walls. Inside the strip elastic scattering occurs with a probability that is determined by the mobility of the 2DEG. Between the scattering events the spin of each individual electron precesses about a field that is the sum of the external magnetic field and the spin-orbit field, which depends on the direction of electron motion. Thus, we can study how the ensemble-averaged spin orientation evolves and dephases as a function of time. To explore the limits of dephasing anisotropy and suppression of spin dephasing in such wire systems we vary the strength of the spin-orbit fields and the degree and orientation of the confinement.

In *Chapter 5* we present a numerical study that explores the possibility of observing a similar suppression of spin dephasing for electrons that are ballistically confined in a wire of bulk GaAs material. The approach is similar as for the 2DEG case, but now the electron ensemble is contained in a box of 1  $\mu\text{m}$  by 1  $\mu\text{m}$  and 200  $\mu\text{m}$  length. This modeling aims at providing an explanation for the observation of suppressed spin dephasing for electrons in a bulk GaAs layer in our experiments with wire structures, which was an unexpected result. We extend this study to exploring the difference between ballistic confinement of 2DEG electrons and photo electrons in a bulk layers. We find that wires of bulk

GaAs material can indeed also show suppressed spin dephasing, and this extends the prospects for using thin bulk layers for realizing spin transport in spintronic device structures.

*Chapter 6* reports the experimental results on the preparation and detection of spin states of localized electrons ( $D^0$  systems) with picosecond laser pulses. By addressing resonant transitions of the Zeeman-split  $D^0$  spin states to a donor-bound exciton state ( $D_0X$ ) with the TRKR technique we could prepare the  $D^0$  spins in a state that is purely determined by the polarization of the preparation pulse: The mapping between the Poincaré-sphere for optical polarization state and the Bloch-sphere for the electron spin state is bijective (Fig. 1.3). In combination with optically controlled spin echo [22] our results give prospects for achieving a  $10^7$  ratio between coherence and operation time for qubits that are based on  $D^0$  spins.

The final chapter, *Chapter 7*, presents our experimental results on characterization of the apparent g factor values which can be observed with TRKR measurements. We apply it to  $n$ -doped GaAs samples in a wide range of Si donor concentrations, from very low ( $3 \times 10^{13} \text{ cm}^{-3}$ ) to metal-to-insulator transition concentrations ( $2 \times 10^{16} \text{ cm}^{-3}$ ). We show that the g factor dependence on pump power has a very different character for samples where the donor concentration is sufficiently high for forming a donor band, as compared to samples with lower donor concentrations. For obtaining time-resolved information about the g factor we apply a wavelet analysis to the experimental TRKR data. This analysis was used for demonstrating how relaxation of the electron kinetic energy influences the apparent g factor.

## References

- [1] E. Bartholin, *Experimenta cristalli islandici* (Copenhagen, 1669).
- [2] G. Uhlenbeck, and S. Goudsmit, *Naturwissenschaften* **47**, 264 (1925).
- [3] G. Uhlenbeck, and S. Goudsmit, *Nature* **117**, 264 (1926).
- [4] W. Thomson, *Proc. R. Soc.* **8**, 546 (1857).
- [5] W. Gerlach, and O. Stern, *Zeit. Phys.* **9**, 349 (1922).
- [6] R. Huges, M. Boshier, *Quantum Computation Roadmap*, <http://qist.lanl.gov/>, (2004).

- 
- [7] *Optical orientation*, edited by F. Meier and B. P. Zakharchenya (Elsevier, Amsterdam, 1984).
- [8] J. M. Kikkawa, I. P. Smorchkova, D. D. Awschalom, *Science* **277**, 1284 (1997).
- [9] J. M. Kikkawa and D. D. Awschalom, *Phys. Rev. Lett.* **80**, 4313 (1998).
- [10] D. Bouwmeester, A. Ekert, and A. Zeilinger, *The Physics of Quantum Information*, (Springer, Berlin, 2000); S. A. Wolf, D. D. Awschalom, R. A. Buhrman, J. M. Daughton, S. von Molnár, M. L. Roukes, A. Y. Chtchelkanova and D. M. Treger, *Science* **294**, 1494 (2001); I. Zutic, J. Fabian, and S. Das Sarma, *Rev. Mod. Phys.* **76**, 323 (2004);
- [11] S. Z. Denega, T. Last, J. Liu, A. Slachter, P. J. Rizo, P. H. M. van Loosdrecht, B. J. van Wees, D. Reuter, A. D. Wieck, and C. H. van der Wal, *Phys. Rev. B* **81** 153302 (2010).
- [12] P. J. Rizo, A. Pugzlys, A. Slachter, S. Z. Denega, D. Reuter, A. D. Wieck, P. H. M. van Loosdrecht and C. H. van der Wal, *New J. Phys.* **12** 113040 (2010).
- [13] R. I. Dzhioev, K. V. Kavokin, V. L. Korenev, M. V. Lazarev, B. Ya. Meltser, M. N. Stepanova, B. P. Zakharchenya, D. Gammon, and D. S. Katzer, *Phys. Rev. B* **66**, 245204 (2002).
- [14] V. B. Berestetskii, E. M. Lifshitz, and L. P. Pitaevskii, *Quantum Electrodynamics* (Pergamon, New York, 1982), 2nd ed., Vol. 4.
- [15] G. Dresselhaus, *Phys. Rev.* **100**, 580 (1955).
- [16] Y. A. Bychkov and E. I. Rashba, *Sov. Phys. JETP*, **39**, 78 (1984).
- [17] M. I. D'yakonov and V. I. Perel', *Sov. Phys. Solid State* **13**, 3023 (1972).
- [18] M. A. Nielsen and I. L. Chuang, *Quantum Computation and Quantum Information* (Cambridge University Press, Cambridge, 2000).
- [19] Kai-Mei C. Fu, C. Santori, C. Stanley, M.C. Holland, and Y. Yamamoto, *Phys. Rev. Lett.* **95**, 187405 (2005).
- [20] Kai-Mei C. Fu, W. Yeo, S. Clark, C. Santori, C. Stanley, M. C. Holland, and Y. Yamamoto, *Phys. Rev. B* **74**, 121304(R) (2006).
- [21] Kai-Mei C. Fu, S. M. Clark, C. Santori, C. R. Stanley, M. C. Holland, and Y. Yamamoto, *Nature Phys.* **4**, 780 (2008).

- [22] S. M. Clark, Kai-Mei C. Fu, Q. Zhang, T. D. Ladd, C. Stanley, and Y. Yamamoto, *Phys. Rev. Lett.* **102**, 247601 (2009).
- [23] M. Sladkov, A. U. Choubal, M. P. Bakker, A. R. Onur, D. Reuter, A. D. Wieck, and C. H. van der Wal, *Phys. Rev. B* **82**, 121308(R) (2010).
- [24] H. Kosaka, H. Shigyou, Y. Mitsumori, Y. Rikitake, H. Imamura, T. Kutsuwa, K. Arai, and K. Edamatsu, *Phys. Rev. Lett.* **100**, 096602 (2008).
- [25] H. Kosaka, T. Inagaki, Y. Rikitake, H. Imamura, Y. Mitsumori, and K. Edamatsu, *Nature (London)* **457**, 702 (2009).
- [26] C. Weisbuch, and C. Hermann, *Phys. Rev. B* **15**, 816-822 (1977).
- [27] M. A. Hopkins, R. J. Nicholas, P. Pfeffer, W. Zawadzki, D. Gauthier, J. C. Portal and M. A. DiForte-Poisson, *Semicond. Sci. Technol.* **2**, 568, (1987).
- [28] H. Mayer and U. Rössler, *Phys. Rev. B* **44**, 90489051 (1991).
- [29] M. Oestreich and W. W. Rühle, *Phys. Rev. Lett.* **74**, 23152318 (1995).
- [30] J. Hübner, S. Döhrmann, D. Hägele, and M. Oestreich, *Phys. Rev. B* **79**, 193307 (2009).

## Chapter 2

# Optical excitation and detection of electron spin coherence

### Abstract

The present chapter introduces several of the physical and experimental concepts that are central in the investigations that are reported later in this thesis. The research used ultrafast optical excitation and detection of electron spin coherence, with readout based on the magneto-optical Kerr effect. This approach has its foundations in the spin-selective interactions between polarized light and electronic states in semiconductors. The chapter ends with an overview of the experimental setup and techniques that were used, with a discussion of several practical considerations.

## 2.1 Introduction

Light and matter interact in many ways. For example, for light in the visible range, some materials are transparent (glass), some are shiny (metals), while some others have color (natural oil is black). All these effects are also present for the wavelengths of light which are not visible for human eye. In this chapter we focus on the interaction of near-infrared light with GaAs-based structures. This involves optical transitions across the band gap of this material, and the physical processes accompanying the excitation of electrons between these bands.

## 2.2 Optical transitions and selection rules

Interband optical transitions in solids give a broad continuous absorption spectrum, in contrast to the absorption spectrum of isolated atoms which consists of discrete lines. In semiconductors there is a threshold for absorption due to the band gap, which is the gap between the valence band and the conduction band. The excitation of an electron from a valence band state to a conduction band state leaves an unoccupied state in the valence band, which is best described as the creation of a hole. Effectively the interband absorption process creates an electron in the final state and hole in the initial state and this may be treated as the creation of an electron-hole pair. Such an electron-hole pair can only be created in case the excitation photon energy  $\hbar\omega \geq E_g$ , where  $E_g$  is the band gap. A small modification to this rule comes from the fact that the electron-hole pair can be created in the form of an exciton, where the electron and hole are in a bound state with binding energy  $E_X$ . Such excitons can be created when the excitation photon energy  $\hbar\omega = E_g - E_X$ .

The strength of an optical absorption is determined by the quantum mechanical transition rate  $W_{i \rightarrow f}$  for exciting an electron from an initial state  $|i\rangle$  to a final state  $|f\rangle$ . This transition rate is given by Fermi's golden rule:

$$W_{i \rightarrow f} = \frac{2\pi}{\hbar} |M|^2 g(\hbar\omega) \quad (2.1)$$

The transition rate is determined by two factors: the matrix element  $M$  and the joint density of states  $g(\hbar\omega)$ . While both are important to have a non-zero transition rate and therefore absorbance, their presence in this formula has a different physical meaning. A non-zero joint density of states for a certain  $\hbar\omega$  means that there are states which have energy difference equal to  $\hbar\omega$ . This is

automatically satisfied if the photon energy of the optical field is equal to the energy difference between electronic states in the two bands.

The origin of polarization-dependant optical selection rules is contained in the matrix element:

$$M = \langle i | H' | f \rangle \quad (2.2)$$

Here  $H'$  is the Hamiltonian term that describes the perturbation by the optical field that is applied to the system. In the dipole approximation  $H' = e\vec{r} \cdot \vec{E}_0$ , where  $\vec{E}_0$  is the electric field of the excitation light and  $\vec{r}$  the electron position. For obtaining the selection rules for the optical transitions it is useful to describe the electron quantum states and the polarization states of light in terms of spherical harmonics  $Y_l^{\pm m}$ , where  $m$  and  $l$  are the quantum numbers of the state. In this notation  $l$  refers to the orbital momentum quantum number and  $m$  represents the momentum projection quantum number [1].

This approach reveals that the angular parts of the electronic Bloch wavefunctions determine which transitions have non-zero values when evaluating equation (2.2), and this governs the selection rules: For electric-dipole allowed transitions  $\Delta l = \pm 1$  and  $\Delta m = \pm 1$  or  $0$ . Generally speaking, other processes such as magnetic-dipole and electric-quadrupole transitions are also possible, but their transition rates are typically much smaller and in the systems under consideration for this thesis they are mostly negligible. Using optical transitions, it is possible to create spin polarization in the material. This process is called optical orientation and it has been extensively studied theoretically and experimentally [2].

### 2.2.1 Optical orientation of conduction band electrons in GaAs

GaAs and GaAs-based heterostructures are the most widely applied material in optical studies of semiconductors [3]. The band structure of GaAs near the  $\Gamma$ -point (electronic wavenumbers near  $k = 0$ ) is shown in Fig. 2.1. The energy bands are here parabolic with an effective mass for the electrons in the conduction band that is much smaller than that of the holes in the valence band. The band gap at  $T = 0$  K is  $E_g = 1.519$  eV and the split-off band is separated from top of the valence band by  $\Delta = 0.34$  eV. During the transitions between the bands, the electronic wavenumber  $k$  does not change since the photon momentum is much smaller than the electronic momentum values.

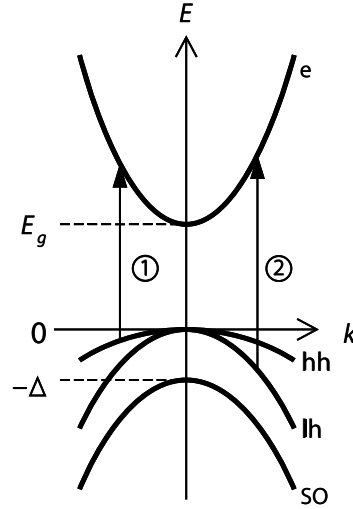


**Figure 2.1:** The band structure of GaAs near  $k = 0$ . In this diagram the energy  $E = 0$  is assigned to the top of the valence band, and  $E = E_g$  then corresponds to the bottom of the conduction band. Four bands are shown: the electron conduction band (e), the heavy hole band (hh), the light hole band (lh) and the split-off band (so). Transitions 1 and 2 are from the heavy hole and light hole bands, respectively. Transitions from the split-off band are possible, but not relevant for the work in this thesis (therefore not shown). Figure adopted from Ref. [4].

### Optical orientation of conduction electrons in GaAs

The selection rules for optical transitions from heavy-hole states and light-hole states to conduction band states in bulk GaAs are summarized in Fig. 2.2. In a geometry where the spin quantization axis is parallel to the light propagation a photon with right circular polarized light  $\sigma^+$  (positive helicity) carries an angular momentum of  $+\hbar$  in the direction of light propagation, and a left circular polarized photon  $\sigma^-$  (negative helicity) carries an angular momentum of  $-\hbar$ . Consequently, with –for example–  $\sigma^+$  light the only allowed transitions are those that change the electronic angular momentum with  $1 \cdot \hbar$ . This yields two allowed transitions, for which the strength (amplitude of the matrix element) differs a factor 3 (the  $-3/2$  to  $-1/2$  transition is 3 times stronger than the  $-1/2$  to  $+1/2$  transition). Accounting for this difference in transition strength, we can calculate the spin polarization  $P$  for electrons in the conduction band that results from excitation with  $\sigma^+$  light:

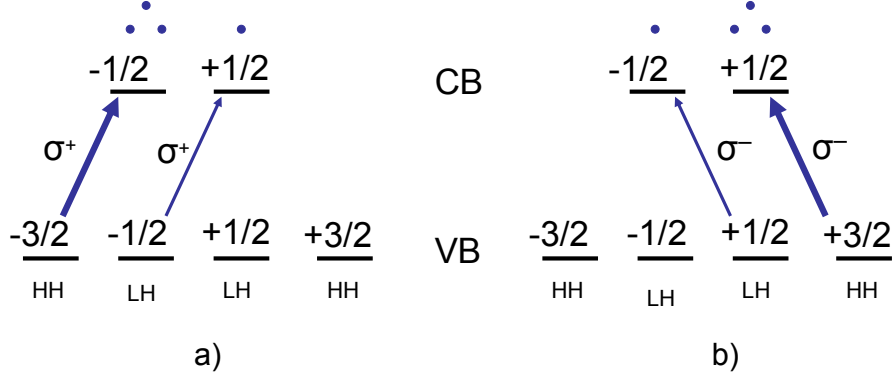


**Figure 2.2:** The selection rules for interband transitions in GaAs for  $\sigma^+$  (a) and  $\sigma^-$  (b) polarizations of light. The conduction band (CB) states have  $s_{1/2}$  character ( $j = \frac{1}{2}$ ) and are labeled with  $m = \pm\frac{1}{2}$ . The highest valence band (VB) states have  $p_{3/2}$  character ( $j = \frac{3}{2}$ ), and are labeled with  $m = \pm\frac{3}{2}$  (heavy holes) and  $m = \pm\frac{1}{2}$  (light holes). The dots above the conduction band states indicate the strength of the non-zero transitions. The transitions from the split-off band are not shown.

$$P = \left| \frac{n_{\uparrow} - n_{\downarrow}}{n_{\uparrow} + n_{\downarrow}} \right| = \frac{1}{2} \quad (2.3)$$

In the case of GaAs structures with confined electronic states (as for example a quantum well system) the degeneracy between the heavy holes and light holes for  $k = 0$  is lifted and the energy needed to excite transitions starting at these levels will no longer be the same [5]. However, the polarization selection rules and the relative transition strengths do not change.

This technique can be used with an external magnetic field (setting the spin quantization axis) parallel to the propagation direction of light. This is known as the Faraday geometry, and in this case the optical orientation technique creates spin polarization that is aligned with the spin-up and spin-down quantization. In this thesis, we mostly report work with a magnetic field (again setting the spin quantization axis) orthogonal to the propagation direction of light. This is known as the Voigt geometry. With ultrashort laser pulses (which have a Heisenberg uncertainty in the photon energy that is larger than the electronic Zeeman splittings), the optical selection rules during the pulse can be applied along the quantization axis that is defined by the propagation direction of light ( $x$ -direction). Consequently, optical orientation then results in spin polarization into a well-defined state that is orthogonal the magnetic field ( $z$ -direction). Such

states are coherent quantum superpositions of spin-up  $|\uparrow\rangle_z$  and spin-down  $|\downarrow\rangle_z$ . For example, the state  $|\uparrow\rangle_x = |\uparrow\rangle_z + |\downarrow\rangle_z$  and  $|\downarrow\rangle_x = |\uparrow\rangle_z - |\downarrow\rangle_z$ . In this case there is spin coherence, and the spins start to precess about the applied magnetic field as soon as they are prepared in the spin-oriented state.

In this description, optical orientation is created for non-equilibrium carriers in the conduction band which will disappear again at the electron-hole recombination rate. For a pure intrinsic GaAs sample the spin coherence can not live longer than the electron-hole recombination time (which is about 300 ps for bulk GaAs at low temperature). The spin coherence can live longer if there is a mechanism for transferring the spin coherence to longer lived states. An interesting example of this can occur with low-doped  $n$ -GaAs materials [6]. In that case electron-hole recombination can occur with the electrons that were already present from doping, such that a fraction of the spin orientation can now live much longer than the electron-hole recombination time.

As a general rule for the experiments on  $n$ -GaAs the hole spin coherence is much shorter lived than electron spin coherence (due to valence band mixing [7]) and therefore does not contribute significantly to the electron spin signal.

### **$\Lambda$ -scheme with localized electrons in $n$ -doped GaAs**

The optical generation of spin polarization in semiconductors is not limited to the generation spin polarized electrons in the conduction band. In the case of  $n$ -doped GaAs with donor concentrations below  $10^{15} \text{ cm}^{-3}$  the donor electrons are at low temperature localized at the donor sites ( $D^0$  systems). We used such materials with Si dopants. At these low doping concentrations the wave-functions of neighboring donor electrons do not overlap. This allows to treat these electrons as an ensemble of non interacting electrons in hydrogen-like orbits, which have a  $1s$ -type ground state at 5.8 meV below the bottom of the conduction band.

In the presence of a magnetic field this two-fold degenerate (due to spin) ground state of the  $D^0$  electron will be split by  $E_{Zeeman} = g_e \mu_B B$ , where  $g_e \approx -0.42 \pm 0.02$  [8, 9] is the  $g$  factor of the  $D^0$  electron in GaAs,  $\mu_B = 5.79 \cdot 10^{-5} \text{ eV/T}$  is the Bohr magneton and  $B$  is the magnitude of the external magnetic field.

These  $D^0$  systems have a hydrogen-like excitation spectrum to states as  $2s$ ,  $2p$  etc., but these excitations have small energies on the order of the 5.8 meV ionization energy. However, they also have localized optical excitations. This concerns a transition to a complex with an electron-hole pair bound at the donor site in addition to the original electron. This is the donor-bound trion system ( $D^0X$  system, often also referred to as the neutral donor-bound exciton complex).

The  $D^0 - D^0X$  optical transition has an energy that corresponds to the band gap minus the exciton binding energy and the binding energy between the exciton and the  $D^0$  system (this energy description neglects the fine structure).

The  $D^0$  to  $D^0X$  transitions in the presence of a magnetic field form a three level ( $\Lambda$ -type) system (see Fig. 2.3) which is an interesting platform for optically manipulating the quantum coherence between the  $|\uparrow\rangle$  and  $|\downarrow\rangle$  states of the  $D^0$  electron.

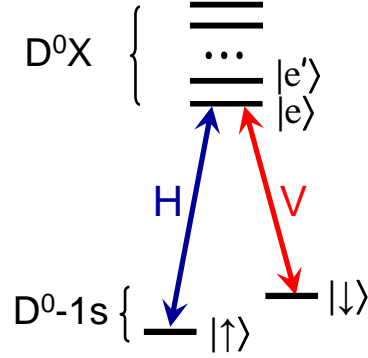


**Figure 2.3:** Energy levels of the  $D^0 - D^0X$  system and optical transitions which correspond to the excitation of a donor-bound exciton  $D^0X$ , in an external magnetic field. The  $D^0$  system is a localized donor electron with a ground state in the form of a hydrogen-like  $1s$  orbital. There is a Zeeman splitting between its two spin states  $|\uparrow\rangle$  and  $|\downarrow\rangle$ . The  $D^0X$  complex consists of an exciton that is bound to the  $D^0$  system and has multiple levels. In a magnetic field, the lowest level  $|e\rangle$  couples to the  $D^0$  spin states with transitions that couple to orthogonal optical polarizations. V stands for vertical (linear polarization along the direction of the external magnetic field) and H stands for horizontal (linear polarization orthogonal to the direction of the external magnetic field)

Polarization dependent transmission spectroscopy on  $D^0$  systems [10] revealed that transitions from  $|\downarrow\rangle$  and  $|\uparrow\rangle$  to the lowest level  $|e\rangle$  of the  $D^0X$  complex couple to orthogonal optical polarizations. In the basis where spin quantization axis is linked to the direction of the external magnetic field and with light propagation orthogonal to the external magnetic field (Voigt geometry) the transitions of interest couple to two orthogonal linear polarizations: The transition from  $|\uparrow\rangle$  to  $|e\rangle$  couples to horizontally polarized light (perpendicular to the magnetic field direction) and the transition from  $|\downarrow\rangle$  to  $|e\rangle$  couples to vertically polarized light (along the magnetic field direction).

It has been shown that within this system it is possible to achieve control over the  $D^0$  spin state by using coherent population trapping (CPT) [11] and electromagnetically induced transparency (EIT) [10]. Fast manipulation of the  $D^0$  spin state was also shown by using red-detuned optical pulses [8].

While the application potential for such three-level  $\Lambda$ -type systems for quantum information purposes and non-linear optics is well established for atomic ensembles [12], this particular semiconductor implementation of a three-level system received less attention till now. The complexity of the excited state complex (Fig. 2.3) allows one to use the developed techniques and methods for three-level systems only in the limit where the spectral width of the control fields is smaller than the level splittings in the  $D^0X$  complex. This strongly limits the spectral width of the excitation light and practically prohibits the use of ultrashort (picosecond range) laser pulses for preparation and readout of the  $D^0$  spin state with the TRKR technique. In *Chapter 6* we review this statement and provide experimental results which show the contrary. The combination of ultrafast (picosecond) spin preparation and the previously developed techniques for ultrafast spin manipulation gives the donor-bound electron system a great prospect for being used as a platform for quantum information schemes.

## 2.3 The Kerr effect

The Magneto-Optical Kerr Effect (MOKE) is one in a family of magneto- and electro-optical effects where applying a magnetic or electric field to a material turns it optically active (affecting the polarization of transmitted and reflected light). The same effects can occur due to a polarization which is present in the material itself. These effects are known since 19th century, but got renewed attention with the development of ultrafast pulsed Ti:Sapphire lasers, which made it possible to study the magnetization dynamics and spin polarization dynamics on very short timescales. For this purpose the Kerr effect and Faraday effect are the two most used at this stage in the scientific community. They are complementary, since the Kerr and Faraday effect are associated with reflected and transmitted light, respectively. Depending on the sample structure (total transmission of the sample) one of them will be preferable. The experiments described in this thesis used the Kerr effect for a time-resolved study of electron spin coherence in GaAs-based materials.

For analysis of the Kerr effect it is useful to distinguish three different geometries, which depend on the relative orientation of the incident (probing) light and

the magnetic moment  $\vec{M}$  in sample. They are presented in Fig. 2.4.

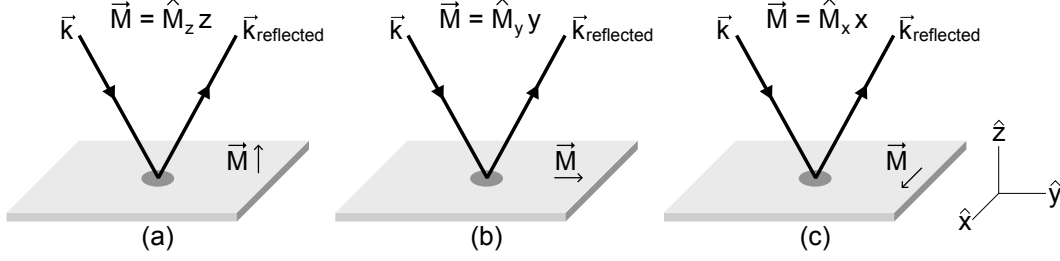


**Figure 2.4:** The three different geometries that are considered for describing the magneto-optical Kerr effect. (a) Polar. (b) Longitudinal. (c) Transverse.

We will concentrate on the Kerr effect where probing occurs with light that is initially linearly polarized. The optical activity induced by the Kerr effect results in a rotation of the polarization of light during the reflection on the sample. This is often called Kerr rotation and quantified by the Kerr rotation angle  $\Theta_k$ . In principle the Kerr effect can also change the degree of ellipticity of the light polarization. Both effects together can be described by the complex Kerr rotation, and is then represented in the following form:

$$\tilde{\Phi}_k = \Theta_k + i\Psi_k \quad (2.4)$$

Here  $\Theta_k$  is the orientation angle of the polarization ellipse and  $\Psi_k$  is the ellipticity angle (see the inset in Fig. 2.5).

For an arbitrary incidence angle  $\phi$  the three different measurement geometries (as shown in Fig. 2.4) give the following real Kerr rotations  $\Theta_k^{s,p}$  (for details see the Ref. [13]). The expressions are given for the  $s$  or  $p$  polarizations (where  $p$  is linear polarization parallel to the plane that is defined by the direction of light propagation and a vector normal to the reflecting surface, and  $s$  is orthogonal to  $p$ ):

(i) The polar Kerr effect:

$$\Theta_k^{s,p} = \text{Im} \left( \frac{\eta^2 \left[ \sqrt{\eta^2 - \sin^2 \phi} \mp \sin \phi \tan \phi \right]}{(\eta^2 - 1)(\eta^2 - \tan^2 \phi)} \cdot Q \right) \quad (2.5)$$

(ii) The longitudinal Kerr effect:

$$\Theta_k^{s,p} = \text{Im} \left( \frac{\eta^2 \sin \phi \left[ \sin \phi \tan \phi \pm \sqrt{\eta^2 - \sin^2 \phi} \right]}{(\eta^2 - 1) (\eta^2 - \tan^2 \phi) \sqrt{\eta^2 - \sin^2 \phi}} \cdot Q \right) \quad (2.6)$$

(iii) The transverse Kerr effect (results only in the intensity change):

$$\delta_p = \frac{\Delta I}{I} = -\text{Im} \left( \frac{4 \eta^2 \tan \phi}{(\eta^2 - 1) (\eta^2 - \tan^2 \phi)} \right) \quad (2.7)$$

Here  $\eta = n_2/n_1$  is the ratio between the complex refractive index of the two adjacent media. The upper sign is for the case of probing with light that has  $s$  polarization and the lower is for the case of  $p$  polarization.  $Q$  is the magneto-optical parameter (or Voigt parameter), which is proportional to the magnetization or spin polarization. The ellipticity angles for the polar and longitudinal geometry can be obtained from Eq. (2.5) and Eq. (2.6) by taking the real part ( $Re$ ) instead of the imaginary part ( $Im$ ). Since  $|\eta| > 1$  and  $\phi$  is small for the experiments described in this thesis, one can see that the polar Kerr effect is the strongest and the longitudinal effect is the weakest one.

The above discussion of the Kerr effect is presented in terms of a generic macroscopic magneto-optical parameter  $Q$ , in a formalism that is useful for assessing the magnitude of the various Kerr signals that can be obtained in different geometries. For the studies in this thesis, however, it is useful to describe here the link to a microscopic picture that relates to the optical transitions in Fig. 2.2. In this picture [2], measuring the rotation from the polar Kerr effect with an initially linearly polarized light pulse is equivalent to measuring an unequal filling of the spin-up and spin-down conduction bands. That is, such an unequal filling gives rise to a difference in the absorption coefficient for  $\sigma^+$  (a) and  $\sigma^-$  laser light that is near resonance with transitions to these states. Through the Kramers-Kronig relation, this also gives rise to a difference in the refractive index for  $\sigma^+$  and  $\sigma^-$  light. Such a difference in the refractive index gives a rotation of the linear probe polarization upon reflection on an interface of the sample, given that the linear polarization is a superposition of  $\sigma^+$  and  $\sigma^-$  light. This picture helps to visualize the process, while for the full understanding of the measured data incorporation of all optical effects which may occur in the sample is important.

The observed Kerr rotation angle is changing sign when tuning the probe laser from red detuned to blue detuned with respect to exact resonance on a certain optical transition, and it is in fact zero when tuned to exact resonance. When

detuning it further (either red or blue) the Kerr rotation goes to zero, since the interaction strength of light and matter is decreasing [13]. Semiconductor systems often have a continuous band of optical transitions rather than a spectrum with isolated optical transitions. However, since the transitions near the band edge dominate the optical response this dependence on detuning is also observed in most III-V semiconductor systems.

## 2.4 Balanced polarization bridge

The typical value of the observed Kerr rotation angle in experiments that probe spins near the bottom of the conduction band in III-V semiconductors is on the order of tens of micro-radians. Although the absolute value of the Kerr angle is less important and the time evolution of it is the focus of the current study, it is crucial to have the necessary precision in the experimental setup.

The most precise method for measuring the rotation of the polarization plane of light is based on a balanced photodetector scheme (also known as polarization bridge). It allows to separate the measurement of ellipticity and rotation and it is (in first order) linear to the spin polarization (magnetization) in the sample.

Figure 2.5 schematically shows the setup with balanced photodetectors used for measurement of polarization rotation. The beam of light after reflection on the sample is split into two beams with orthogonal polarization with a Wollaston prism, such that each detector only detects the  $s$  or  $p$  component (in the basis linked to the Wollaston prism). The  $\lambda/2$ -plate before the Wollaston prism is rotating the polarization of the light such that in the basis of the Wollaston prism the  $s$  and  $p$  components have the exact same intensities if there is zero spin polarization in the sample. This procedure of balancing the detection scheme is done before any spin polarization is induced in the sample. Using the  $\lambda/2$ -plate for balancing is very practical since it allows balancing the detector contributions while the optical paths of the beams remain unchanged (so that the alignment of the setup remains untouched and intact).

In the absence of spin polarization in the sample along the direction of light propagation (the component of spin polarization to which the light is sensitive for the polar Kerr effect) the difference between the signals from both detectors is now zero. The intensities of light in the two beams to the detectors become different when there is spin polarization in the sample.

When only accounting for the polarization change in light that is linear with the amount of spin polarization in the sample, the complex Kerr rotation can be

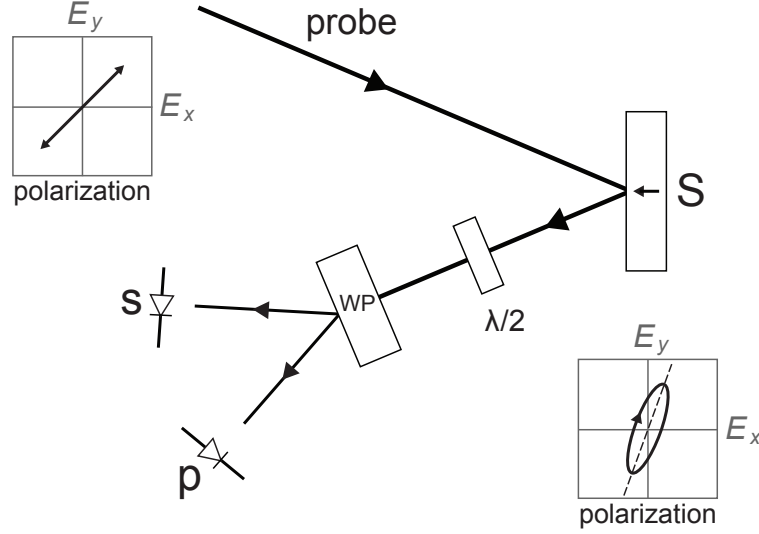


**Figure 2.5:** Schematic drawing of the polarization bridge with balanced photodetectors. The probe beam (initially linearly polarized) acquires a Kerr rotation and ellipticity due to interaction with a spin polarized region in the sample (S). The half-wave ( $\lambda/2$ ) plate brings the polarization to the basis of a Wollaston prism (WP), in which the photodetectors give a balanced signal for zero spin polarization in the sample (*i.e.* zero signal after subtraction).

described with a rotation matrix  $R$  in the Jones formalism for describing light polarization [14]:

$$R = \begin{pmatrix} \cos \tilde{\Phi}_k & -\sin \tilde{\Phi}_k \\ \sin \tilde{\Phi}_k & \cos \tilde{\Phi}_k \end{pmatrix} \quad (2.8)$$

where  $\tilde{\Phi}_k$  is the complex Kerr rotation as defined in Eq. (2.4). The Jones vector for the probe light in the basis of the Wollaston prism, for the case of zero Kerr rotation after reflection (*i.e.* the signal that defines zero after balancing) can be expressed as:

$$\vec{E} = \begin{pmatrix} E^s \\ E^p \end{pmatrix} = \begin{pmatrix} 1 \\ 1 \end{pmatrix} \quad (2.9)$$

After acquiring a non-zero Kerr rotation  $\tilde{\Phi}_k$  (assumed to be small,  $|\tilde{\Phi}_k| \ll \pi$ ), the polarization of the beam is transformed and the two measured components (with the  $s$  and  $p$  detector) are no longer equal in intensity:

$$\vec{E}_{measured} = \begin{pmatrix} \cos \tilde{\Phi}_k & -\sin \tilde{\Phi}_k \\ \sin \tilde{\Phi}_k & \cos \tilde{\Phi}_k \end{pmatrix} \begin{pmatrix} 1 \\ 1 \end{pmatrix} \approx \begin{pmatrix} \tilde{\Phi}_k - 1 \\ \tilde{\Phi}_k + 1 \end{pmatrix} \quad (2.10)$$

The photodetectors (see Fig. 2.5) measure the  $s$  and  $p$  components separately, and the Kerr signal is obtained by subtracting the  $s$  and  $p$  signals:

$$I_{measured} = I_p - I_s \propto |\vec{E}_{measured}^p|^2 - |\vec{E}_{measured}^s|^2 \quad (2.11)$$

This results in a final signal being proportional to the real Kerr rotation  $\Theta_k$ , and not sensitive to the ellipticity change (complex Kerr rotation is substituted as defined in Eq. (2.4)):

$$I_{measured} \propto |\tilde{\Phi}_k + 1|^2 - |\tilde{\Phi}_k - 1|^2 = [(\Theta_k + 1)^2 + \Psi_k^2] - [(\Theta_k - 1)^2 + \Psi_k^2] = 2\Theta_k \quad (2.12)$$

A setup that measures  $\Theta_k$  in this manner can be easily modified into one that measures the change in ellipticity. A quarter-wave-plate should then be placed before the Wollaston prism (which is equivalent to adding an additional rotation matrix with angle of  $\pi/4$  in Eq. (2.10)). The measured signal is then proportional to the ellipticity, and not sensitive to Kerr rotation:

$$I_{measured} \propto 2\Psi_k \quad (2.13)$$

This technique with balanced photodetectors, where the signal spin signal comes from a difference measurement, cancels out intensity fluctuations and many other experimental fluctuations, such that it is at the same time a very sensitive and a robust method. It allows one to measure very precisely a very small rotation of the light polarization. In our setup the typical accuracy was  $\approx 10$  nrad.

If the sample has a few layers which could contribute to the Kerr rotation, or in case that the area of interest is not homogeneously spin polarized, the measured signal is a superposition of these various contributions (which can also come with opposite signs). In such a case the resulting Kerr signal is complicated and requires a very careful and precise analysis. An example of such a situation is discussed in more detail in *Chapter 3*.

The Kerr effect can be used to measure all three components of magnetization (spin polarization) in a sample, but this requires changing the experimental setup for measuring each component. However, with an external magnetic field that precesses the spin polarization it is also possible to observe all three components. Alternatively, one can in certain cases exploit the optical selection rules and measure the spin polarization in different direction simply by selecting different probe polarizations. An interesting example of such a case is demonstrated and analyzed in *Chapter 6*.

## 2.5 Measurement setup

Figure 2.6 presents a schematic diagram of the experimental setup. It is optimized for operating the Time-Resolved Kerr Rotation (TRKR) method for detecting spin coherence that was already introduced in *Chapter 1*. Essential to this method is that a pump pulse creates spin coherence, which is then detected with a probe pulse after a controllable delay. A pulsed Ti:Sapphire laser (Coherent, model Chameleon Ultra) is used to generate both pump and probe pulses (tunable wavelength  $\lambda$ , 150 fs pulses with  $\sim 7$  nm spectral width, at 80 MHz repetition rate). They can be spectrally narrowed to  $\Delta\lambda = 1.2$  nm with tunable liquid-crystal Fabry-Perot interferometric filters (LCFP). This increases the pulse durations to about 1 ps. This is either applied at the place marked LCFP 1, or separately for pump and probe at the places marked LCFP 2 and LCFP 3. This allows to switch between single- and two-color pump-probe experiments while only using a single laser, and without too much changes to the setup. The single-color experiments can also be performed without LCFP filters in the setup in case a time resolution well below 1 ps is desired, or when applying the LCFP compromises the optical pulse energies that can be used too much.

After collimation the principle beam is split into a pump and probe beam. The time delay pump and probe pulses is controlled with a retroreflector mounted on a computer-controlled mechanical delay line, which is positioned in the pump beam (since it is preferable to have a very stable beam path for the probe beam onto the detectors). Area 3 in Fig. 2.6 is for some experiments used for creating two pump pulses per probe pulse. The delay between the two pump pulses is then controlled with a hand-controlled mechanical delay line. This is realized by splitting the pump beam into two beams, which are aligned to fully overlap again after additional path length for one of the two beams. Such double pump pulses were used for the experiments on spin preparation for  $D^0$  systems (*Chapter 6*).

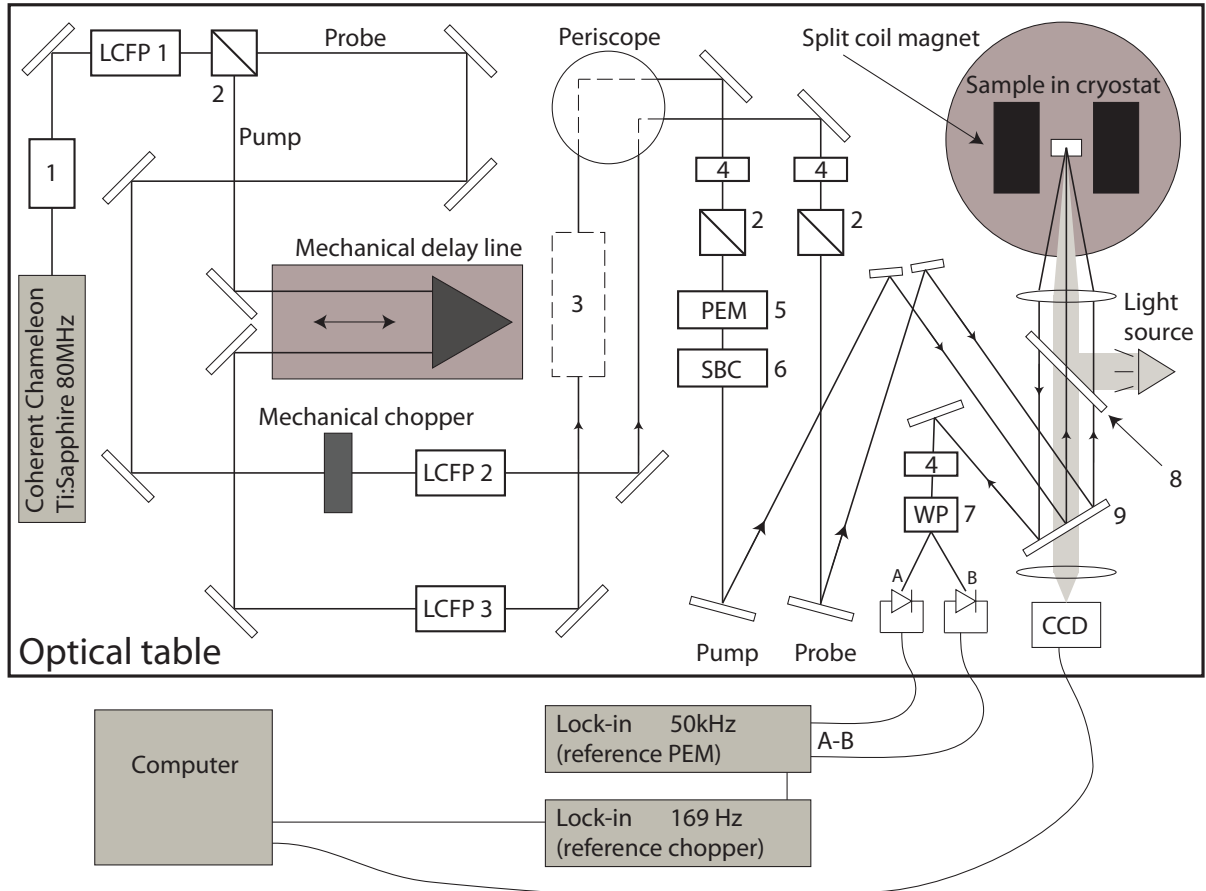


**Figure 2.6:** Schematic representation of the experimental setup. 1 - Collimator; LCFP - Liquid crystal Fabry-Perot filters (experiments either used none, nr. 1 alone, or the pair nr. 2 and 3); 2 - Polarizers and polarizing beam splitters; 3 - Area for adding a second pump pulse (used in *Chapter 6*); 4 -  $\lambda/2$  plate; 5 - Photo-Elastic Modulator (PEM); 6 - Soleil-Babinet Compensator; 7 - Wollaston Prism; 8 - Glass plate; 9 - Dielectric mirror with polished back side; A,B - photodetectors. Iris, neutral density filters and beam pick-off points for measuring spectra and are not shown for simplicity.

The periscope is adjusting the height of the beam path in the left and the right parts of the optical table (from laser height to cryostat height). All optical components in the beam path after the periscope are mounted on a sliding breadboard (excluding the cryostat) for practical purposes. In the pump and probe beams  $\lambda/2$  plates and polarizers are defining and purifying the polarization states of the beams. After this point, all mirror reflections in the optical scheme use rather sharp angles (not too far from normal-incidence). This is necessary for

preserving the polarization upon reflection (our tests showed that the polarization preserving properties of the dielectric mirrors used depend on the angle of incidence).

The pump beam is directed on mirror 9 in such a way that pump beam follows the optical axis of the confocal microscope that is formed by the two lenses in between the cryostat and the CCD camera in Fig. 2.6. An incoherent light source and glass plate 8, together with mirror 9 facilitate imaging of the sample in the cryostat, with ability to observe the pump and probe focal spots on the sample at the same time. Mirror 9 is a dielectric mirror with a polished back surface. It is slightly transparent for the laser beams, while it allows visible light to propagate through it without significant distortions. This combination of the confocal microscope for visible light and the focusing scheme for the laser beams allows one to see the sample during the aligning procedures, and to also check the position of the pump and probe spots and their overlap on the sample.

The probe beam is aligned on mirror 9 just to side of the pump beam (which is central on the mirror). Thus, after reflecting on the sample the probe can be picked up again with mirror 9 and further guided to the  $\lambda/2$  plate and the Wollaston prism that are part of the balanced scheme for detecting polarization rotation.

A Photo-Elastic Modulator (PEM) in combination with a Soleil-Babinet compensator (SBC) are used to manipulate the polarization of the pump beam. A SBC is a variable wave plate which allows to achieve any possible retardation and the PEM is used to modulate the pump polarizations at a frequency of 50 kHz between two orthogonal polarizations (sinusoidal modulation between fully orthogonal states). Such modulation can be used in a lock-in detection scheme, but also avoids constantly pumping the same electron spin polarization. Such constant pumping may lead to dynamic nuclear polarization effects [6], which is should be circumvented for detailed studies of the electron g factor and spin dephasing time.

The PEM modulation is in most of our TRKR experiments central in a lock-in detection scheme that strongly improved the signal-to-noise ratio of the Kerr signals. Many experiments also used a double modulation scheme, realized by modulating the probe beam intensity as well with a mechanical chopper at a frequency around 169 Hz. Thus, we can use cascaded detection of a double modulated signal. Alternatively, the chopper can be operated at a sub-harmonic frequency of the PEM (*e.g.* at  $f_C = 50/16$  kHz), with direct lock-in detection of a side band at  $f_C$  from the PEM frequency. Such double modulation schemes are

essential for single-color TRKR experiments where a portion of the reflected pump light is unintentionally incident on the photo detectors, despite the geometric separation from the probe path. This mainly occurs with samples that have a rough or structured surface.

The sample is placed in the cryostat (Oxford Spectromag, 2 to 300 Kelvin while applying a field in the range from 0 to  $\pm 7$  Tesla), such that a split coil superconducting magnet will generate a magnetic field in the plane of the sample, and light propagation is orthogonal to the sample. It is very useful to be able to do measurements at different spots on a sample, without the need to spend much time and efforts on realigning the whole beam path to and from the sample. For this purpose we have designed and made a sample holder in the cryostat where we can use piezo positioners from Attocube Systems AG, Germany (see Fig. 2.7). This also improves the ability to compare the TRKR signals from different areas of a sample. Such a design allows one to move the sample in the focal plane, such that virtually no re-adjustments are needed for the optical components after sample displacement. It also simplifies the alignment procedure by allowing corrections on  $\theta$ , since optimal TRKR detection is achieved with the sample normal to the pump beam.

## 2.6 Measurement of the spin dephasing time ( $T_2^*$ )

The presented setup is designed to characterize and quantify the dynamics of spin polarization in GaAs-based structures and devices. As discussed in the above, the generation (via optical orientation) and detection (via Kerr-rotation measurement) of spin polarization and spin coherence is done by means of short optical pulses.

Most of the TRKR experiments reported in this thesis include measurements in a magnetic field, with the setup in Voigt geometry. In this case the spins are prepared in a state that is orthogonal to the applied field, and start to precess immediately after initialization. The measured Kerr signal then show oscillations as a function of pump-probe delay that directly reflect coherent spin precession, with a transient signal envelope (loss of Kerr signal to zero) that directly reflects spin dephasing or loss of Kerr signal due to electron-hole recombination (more in general it can also be due to electrons leaving the probe volume via transport). An example of such a trace was presented in Fig. 1.1, and its mathematical form

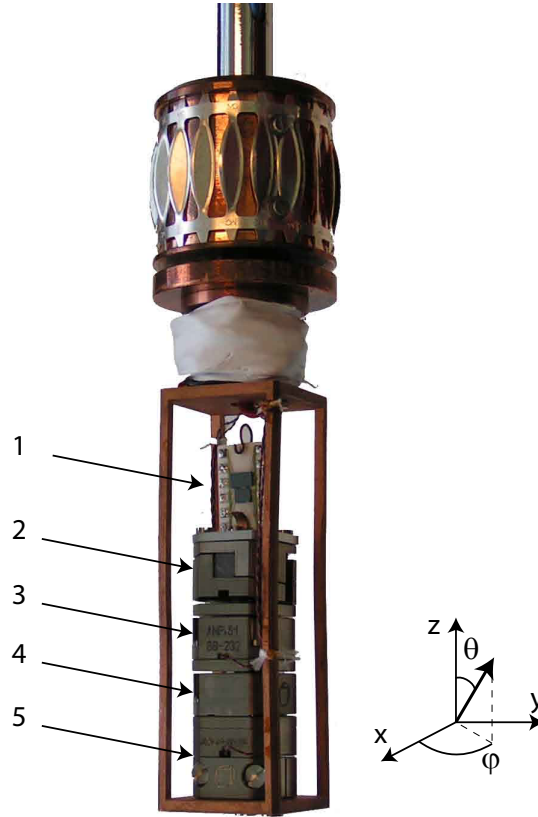


**Figure 2.7:** Photo of the sample holder at the bottom of a sample stick that is inserted in the cryostat. 1 - Chip with two samples glued on it with varnish; Labels 2 to 5 refer to piezo positioners from Attocube Systems AG (Germany) for different degrees of freedom. 2 - Adjustments in  $\theta$ ; 3 - Adjustments in  $x$ ; 4 - Adjustments in  $y$ ; 5 - Adjustments in  $z$ . An adjustment in  $\varphi$  can be realized by rotating the whole sample stick.

is typically close to Eq. (1.1). Thus, working with a magnetic field in Voigt geometry has the advantage that TRKR gives an unambiguous fingerprint of spin coherence and allows for a direct determination of its decay time.

In this case, spin polarization is prepared in a state that is not parallel with the spin quantization axis. Thus, the method prepares spin coherence since the electrons are after the optical transition in well-defined quantum states that are also coherent with respect to each other. The coherence of individual electron spins will decay in time (over a  $1/e$  timescale that is known as the homogeneous spin decoherence time  $T_2$ ). However, the TRKR technique that we described here

measures the projection of spins along a certain axis, averaged over an ensemble (without applying a spin-echo technique). Thus, the spin coherence signal also goes to zero in case the coherent precessional dynamics of different spins acquires phases that differ more than  $\pi$  between individual spins in the ensemble. This is characterized by the  $1/e$  timescale  $T_2^*$ , which is known as the spin dephasing time or the inhomogeneous spin coherence time.

In zero field, the decay of a TRKR spin signal can be due to spin relaxation (at the timescale  $T_1$ ), pure spin decoherence and spin dephasing [15]. However, in semiconductors spin relaxation is typically much slower than spin decoherence and dephasing, and TRKR signals then typically decay at the timescale that is set by the minimum of  $T_2^*$  and the electron-hole recombination time.

## 2.7 Summary

We presented the realization of a setup for Time-Resolved Kerr Rotation (TRKR) measurements which can be used at temperatures from 2 to 300 Kelvin while applying a magnetic field with a value in the range from 0 to  $\pm 7$  Tesla. The shortest time resolution that can be achieved is about 150 fs. Spectral tuning of pump and probe pulses is possible, including the ability to switch between single-color and two-color pump-probe experiments. While the spatial resolution of the optical focusing on the sample is about 150 microns, the control over the sample positioning is on the sub-micron scale.

## References

- [1] C. Cohen-Tannoudji, B. Diu, and F. Laloë, *Quantum Mechanics* (John Wiley and Sons, 1977).
- [2] *Optical orientation*, edited by F. Meier and B. P. Zakharchenya (Elsevier, Amsterdam, 1984).
- [3] M. Cardona and P. Y. Yu, *Fundamentals of Semiconductors* (Springer-Verlag, 2001).
- [4] M. Fox, *Optical Properties of Solids* (Oxford University Press, New York, 2001).
- [5] J. Hübner and M. Oestreich, *Semicond. Sci. Technol.* **23**, 114006 (2008).
- [6] J. M. Kikkawa and D. D. Awschalom, *Phys. Rev. Lett.* **80**, 4313 (1998).

- [7] M. Oestreich, S. Hallstein, A. P. Heberle, K. Eberl, E. Bauser, and W. W. Rühle, *Phys. Rev. B* **53**, 7911 (1996).
- [8] K.-M. C. Fu, S. M. Clarck, C. Santori, C. R. Stanley, M. C. Holland, and Y. Yamamoto, *Nature Physics* **4**, 780 (2008).
- [9] S. Z. Denega, M. Sladkov, D. Reuter, A. D. Wieck, and C. H. van der Wal, arXiv:1103.4307 (2011).
- [10] M. Sladkov, A. U. Choubal, M. P. Bakker, A. R. Onur, D. Reuter, A. D. Wieck, and C. H. van der Wal, *Phys. Rev. B* **82**, 121308(R) (2010).
- [11] K.-M. C. Fu, C. Santori, C. R. Stanley, M. C. Holland, and Y. Yamamoto, *Phys. Rev. Lett.* **95**, 187405 (2005).
- [12] M. D. Lukin, *Rev. Mod. Phys.* **75**, 457 (2003).
- [13] A. K. Zvezdin and V. A. Kotov, *Modern Magneto-optics and Magneto Optical Materials* (Institute of Physics, London, 1997).
- [14] A. Gerrard and J. M Burch *Introduction to Matrix Methods in Optics* (Wiley, Ney York, 1975).
- [15] J. Fabian, A. Matos-Abiague, C. Ertler, P. Stano, and I. Zutic, *Semiconductor Spintronics*, *Acta Phys. Slov.* **57**, 565-907 (2007).

## Chapter 3

# Suppressed spin dephasing for 2D and bulk electrons in GaAs wires due to engineered cancellation of spin-orbit interaction terms

### Abstract

We report a study of suppressed spin dephasing for quasi-one-dimensional electron ensembles in wires etched into a GaAs/AlGaAs heterojunction system. Time-resolved Kerr-rotation measurements show a suppression that is most pronounced for wires along the [110] crystal direction. This is the fingerprint of a suppression that is enhanced due to a strong anisotropy in spin-orbit fields that can occur when the Rashba and Dresselhaus contributions are engineered to cancel each other. A surprising observation is that this mechanism for suppressing spin dephasing is not only effective for electrons in the heterojunction quantum well, but also for electrons in a deeper bulk layer.

---

This chapter is based on Ref. 4 on p. 103.

### 3.1 Introduction

For electron ensembles in semiconductor device structures the dominant mechanism for spin dephasing and spin relaxation is often due to spin-orbit interaction (SOI). A current challenge in the field of spintronics is therefore to obtain control over such relaxation, or to even turn SOI into a resource for spin manipulation [1]. GaAs/AlGaAs based heterostructures provide here an interesting platform. Besides high material quality and good optical selection rules, these materials can be engineered to have two types of SOI: Dresselhaus SOI, resulting from lack of inversion symmetry in the GaAs crystal structure, and Rashba SOI, effective when electrons are confined in a layer with bending of the conduction band [2]. Such SOI acts as a  $k$ -vector-dependent effective magnetic field on electron spins. Notably, the strength of these two effects can be tuned to exactly cancel each other [3, 4] for electrons with the  $k$  vector in [110] direction [Fig. 3.1(a)]. This notion is central in many proposals [5, 7, 6, 8, 9] that aim at suppressing spin relaxation effects. Work on unpatterned quantum-well areas with techniques that filter out signals from electrons with [110]  $k$  vectors confirmed reduced dephasing for these electrons [10, 11, 4].

We report here the observation that this cancellation of two SOI terms can directly result in suppressed spin dephasing for an entire electron ensemble in a wire along the [110] direction. Notably, this does not require that full quantum confinement restricts electron transport in the wire to the [110] direction. Instead, it concerns a strong enhancement of a motional-narrowing type effect that results from frequent scattering on the boundaries of quasi-one-dimensional (1D) wires [12, 13, 14] that can—with further tuning—suppress spin dephasing by several orders of magnitude [15, 16]. Quasi-1D systems are here defined as having the wire width too wide for 1D quantum confinement, but smaller than the spin precession length (ballistic travel distance during which spins precess an angle  $\pi$  in the sum of spin-orbit fields and external magnetic field). In addition, the wire width should not be much in excess of the mean free path.

### 3.2 Experimental realization

We used electron ensembles in GaAs/AlGaAs wires (Fig. 3.1) that contain a heterojunction-based two-dimensional electron gas (2DEG) for which the Rashba and linear Dresselhaus SOI are of similar strength [3]. We used time-resolved Kerr readout for directly testing whether quasi-1D confinement in device structures

combined with anisotropy for SOI in  $k$  space can be tuned to give a pronounced suppression for spin dephasing for wires in the  $[110]$  direction. For 2DEG electrons we indeed observe this behavior, which we will further call spin-dephasing anisotropy (SDA). Surprisingly, we also obtained evidence for a new manifestation of SDA: a contribution to our Kerr signals from a deeper bulk layer in our wires also shows SDA. We can explain these observations by considering that an electron ensemble in a bulk layer with weak band bending [Fig. 3.1(c)] is also subject to a Rashba-type SOI and we find agreement with numerical modeling of such a situation.

We fabricated arrays of quasi-1D wires with electron-beam lithography and subsequent wet etching of a GaAs/AlGaAs heterojunction system with a 2DEG at 114 nm depth (etch depth  $\sim 100$  nm). Figure 3.1(b) is a micrograph of an array with wires along  $[110]$  ( $1.2 \mu\text{m}$  wire width and  $1.6 \mu\text{m}$  periodicity). Other

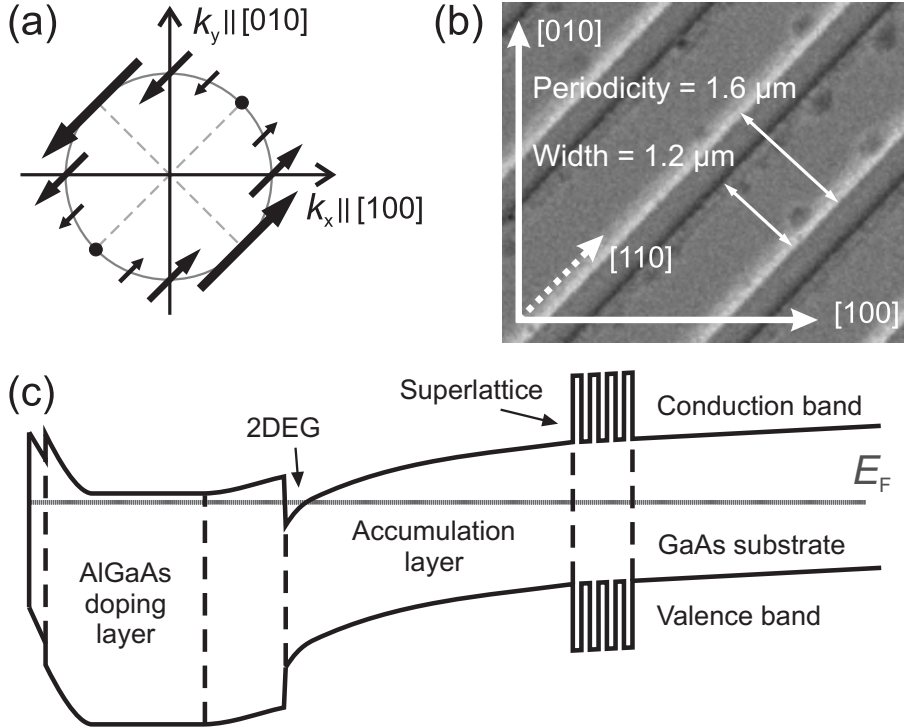


**Figure 3.1:** (a) Dependence of spin-orbit fields on  $k$  vector on the Fermi circle in the  $k_x$ - $k_y$  plane for equal strength of Rashba and linear Dresselhaus effect. (b) Scanning-electron micrograph for a section of a wire array oriented along the  $[110]$  crystal direction. (c) Band diagram of the GaAs/AlGaAs heterostructure (not to scale), with a 2DEG where the conduction band bends below the Fermi energy  $E_F$ .

areas had [100], [010], and [-110] oriented wires, and for reference we had both unpatterned and fully etched areas. Figure 3.1(c) shows a band diagram of the GaAs/AlGaAs heterostructure along growth direction. The layer sequence starts with an intrinsic (001) oriented GaAs substrate, followed by a training layer (superlattice with 10 periods of 5.2 nm GaAs and 10.6 nm AlAs). Then a 933 nm undoped GaAs accumulation layer is followed by a 37 nm undoped  $\text{Al}_{0.32}\text{Ga}_{0.68}\text{As}$  spacer layer. On top of this 72 nm homogeneously Si-doped  $\text{Al}_{0.32}\text{Ga}_{0.68}\text{As}$  is grown. The heterostructure is finished by a 5 nm GaAs cap layer. The 2DEG is at the heterojunction between the AlGaAs spacer layer and the GaAs accumulation layer. Under illuminated conditions at 4.2 K the electron density is  $n_{2D} = 4.7 \times 10^{15} \text{ m}^{-2}$  and the mean free path is  $\sim 30 \mu\text{m}$ .

The spin dynamics was probed with conventional [17] mono-color time-resolved Kerr-rotation measurements in an optical cryostat at 4.2 K with magnetic fields (magnitude  $B$ ) up to 7 T. We used a tunable Ti:sapphire laser with  $\sim 150$  fs pulses at 80 MHz repetition rate. The spectrum of pulses was wider than Fourier-transform limited, with significant amplitudes over a  $\sim 15$  meV window. Samples were excited at normal incidence with a circularly polarized pump pulse (helicity modulated at 50 kHz with a photoelastic modulator for avoiding nuclear polarization). This induces a nonequilibrium electron ensemble in the conduction band with a net spin orientation along the growth direction of the sample. The evolution of the spin ensemble is recorded by measuring the 50 kHz component in Kerr rotation after reflection of a linearly polarized probe pulse with a polarization bridge, as a function of pump-probe delay  $t$ . We used spot diameters of about  $100 \mu\text{m}$  on wire arrays of larger dimensions [18]. All data were taken at pump-photon density  $n_{ex} \approx 3 \times 10^{15} \text{ m}^{-2}$  per pulse. Measurements were performed with the external field in [110] direction, unless stated otherwise.

### 3.3 Signatures of spin dephasing anisotropy for 2DEG and bulk electrons

While a heterojunction system is for our research an interesting material given the strong and tunable band bending in the 2DEG layer, it imposes difficulties for an experiment with optical probing (as compared to double sided quantum wells). The bandgaps for the 2DEG layer, and deeper parts of the accumulation layer and the substrate are nearly identical [Fig. 3.1(c)], so probing must use reflection and one cannot avoid that Kerr signals have contributions from both 2DEG electrons

and bulk electrons in these deeper layers. We recently characterized [19] that it is for our material nevertheless possible to isolate the Kerr signal from 2DEG electrons when pumping at least  $\sim 20$  meV above the bottom of the conduction band for bulk (we used 1.55 eV). In summary, at pump intensities with  $n_{ex} \leq n_{2D}$  the Kerr signal  $\theta_K$  is a superposition of two mono-exponentially decaying cosines,

$$\theta_K = \sum_{i=1,2} A_i \exp\left(-\frac{t}{\tau_i}\right) \cos\left(\frac{|g_i|\mu_B B}{\hbar}t + \phi_i\right) \quad (3.1)$$

with amplitudes  $A_i$ ,  $g$  factors  $|g_i|$ , dephasing times  $\tau_i$ , and  $\phi_i$  are apparent initial phases [20] for spin precession. This also applies to the data that we present here. Figures 3.2(a) and 3.3(a) show Kerr signals from wires, recorded in fields of 0 T to 7 T. In particular at high fields, the envelopes of oscillating Kerr signals show clear nodes and anti-nodes and we checked that all Fourier transforms of data taken at  $B > 3$  T showed two pronounced peaks at  $g$  factors  $|g_1| \approx 0.36$  and  $|g_2| \approx 0.43$ . Further, Eq. 3.1 always yields good fits for these same  $g$ -factors, also when applied to data in the range 0 T to 3 T. In our earlier work we identified the contribution with  $|g_1| \approx 0.36$  as a population in the 2DEG layer, and the contribution with  $|g_2| \approx 0.43$  as a population in a bulk GaAs layer [19]. The slow growth during delays till  $\sim 100$  ps (as compared to mono-exponential decay for a single population) of signals (at 0 T) and signal envelopes also originates from having a superposition of two contributions. It occurs because the amplitudes  $A_i$  always have opposite sign (for  $\phi_i$  around zero) [19].

SDA is apparent in the zero-field Kerr signals in Fig. 3.2(a) from wires oriented along the [110], [-110], [100], and [010] (and for reference from unpatterned area). The decay of signals during delays  $t > 100$  ps clearly depends on the wire orientation. The loss of Kerr signal is fastest for [-110] oriented wires (only slightly slower than for unpatterned area). Kerr signal decay is slowest for [110] oriented wires, and results for wires in [100] and [010] directions are in between these extreme cases and nearly identical. The inset of Fig. 3.2(a) shows that the time scale for slow signal growth for  $t < 100$  ps has a similar dependence on wire orientation, with again the slowest time scale for the [110] direction. For the Kerr signals measured in the range 1 T to 7 T in Fig. 3.3(a), all traces have envelopes with slow growth for  $t < 100$  ps, and decaying envelopes for  $t > 100$  ps as the zero-field signals. At 1 T, the corresponding time scales are again clearly longest for [110] wires and shortest for [-110] wires but the differences degrade for  $B > 1$  T. We only present signals for the extreme cases [-110] and [110], results for [100] and [010] wires show intermediate behavior.

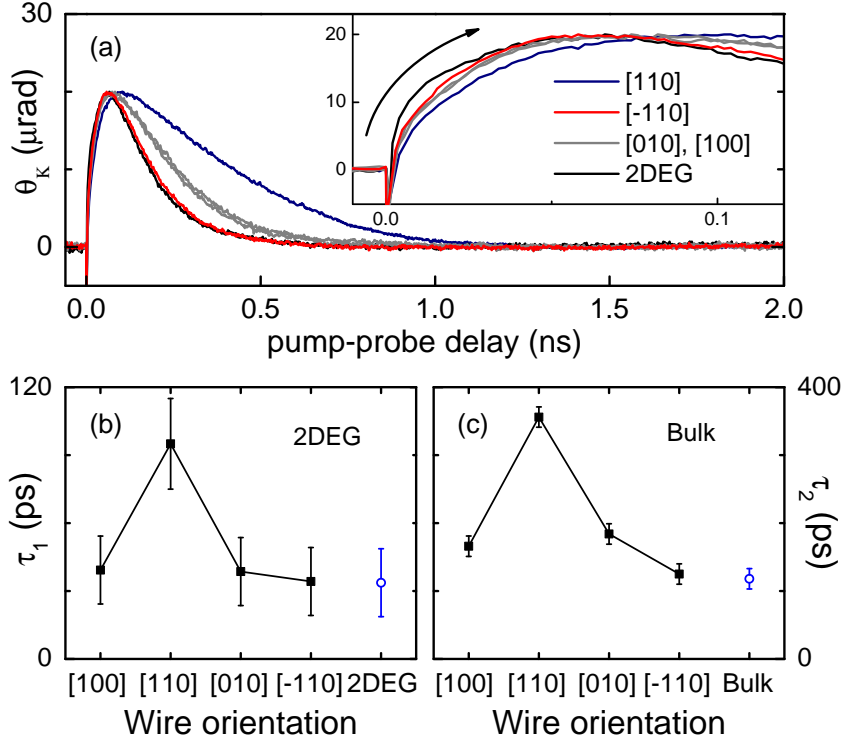


**Figure 3.2:** Spin-dephasing anisotropy at zero external magnetic field. (a) Kerr rotation as a function of pump-probe delay for the unpatterned area and wires in [-110], [110], [100], and [010] directions (order along arrow in traces and legend match). The inset shows the Kerr response at short delays to highlight the slow growth in all traces. [(b) and (c)] Spin-dephasing times for both the 2DEG ( $\tau_1$ ) and bulk ( $\tau_2$ ) spin populations.

Fitting these results with Eq. (3.1) yields traces which very closely match the experimental traces (therefore not shown). Signals from  $B \geq 1$  T give results for  $\tau_i$  for both the 2DEG ( $|g_1| \approx 0.36$ ) and bulk ( $|g_2| \approx 0.43$ ) contributions to the signals [Figs. 3.3(b) and 3.3(c)]. This identifies that the time scale for slow growth ( $t < 100$  ps) is dominated by dephasing of the 2DEG population, while the later decay of signals ( $t > 100$  ps) is dominated by dephasing of a bulk population. The behavior for  $B = 0$  T [Figs. 3.2(b) and 3.2(c)] is interpreted in the same way from extrapolating down the trends in  $\tau_i$  for  $B > 0$  T. This identification of populations based on  $g$  factors is consistent with reported values for dephasing times in high-mobility 2DEGs [ $\sim 50$  ps due to rapid D'yakonov-Perel' (DP) dephasing [3, 21, 22]] and intrinsic GaAs layers [ $\sim 300$  ps [17]].

The results in Figs. 3.2(b) and 3.3(b) give clear evidence for SDA for the 2DEG

population, with qualitative agreement with predicted behavior [15, 23]. These predictions were based on the assumption that Rashba and linear Dresselhaus SOI terms dominate. Expressed as  $k$ -vector-dependent effective fields these are  $\vec{B}_R = C_R(\hat{x}k_y - \hat{y}k_x)$  and  $\vec{B}_{D1} = C_{D1}(-\hat{x}k_x + \hat{y}k_y)$ , respectively, with typical magnitudes of about 2 T for heterojunction 2DEGs [3]. A summary of the numerical approach is given below for the bulk population. The dependence of 2DEG dephasing on wire orientation is here less strong than expected for exact cancellation for  $C_{D1} = C_R$  [15, 4]. Instead, it is consistent with simulations for  $|C_{D1} + C_R|/|C_{D1} - C_R| \approx 3$

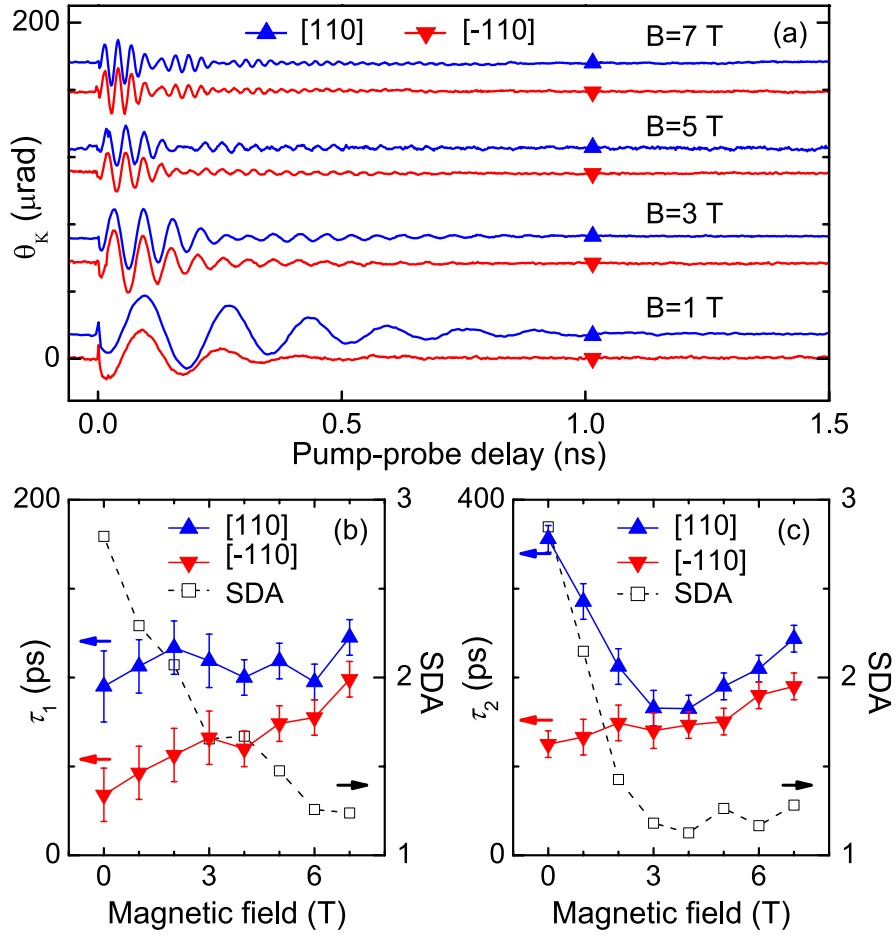


**Figure 3.3:** Evolution of spin-dephasing anisotropy (SDA) in transverse magnetic fields up to  $B = 7$  T. (a) Kerr signals as a function of pump-probe delay from  $[110]$  and  $[-110]$  oriented wires (traces offset for clarity). [(b) and (c)] Corresponding spin dephasing times  $\tau_i$  as a function of  $B$ , for (b) 2DEG and (c) bulk electrons. These plots also present SDA quantified as  $\tau_{i,[110]}/\tau_{i,[-110]}$ .

and  $C_{D1}$  and  $C_R$  as reported values [3]. We cannot make more detailed statements about  $C_{D1}$  and  $C_R$  values since we analyzed that this should account for the influence of the cubic Dresselhaus SOI, momentum relaxation, and electron-hole recombination on the observed Kerr signals. The dependence of SDA on  $B$  is discussed below.

The SDA observed for spins in a bulk layer in Figs. 3.2(c) and 3.3(c) was an unexpected result since SDA was until now only considered for 2D electron systems. Apparently, our samples also contain quasi-1D ensembles with bulk characteristics that have anisotropy for SOI. Such ensembles must indeed be present because band bending is significant up to  $\sim 2 \mu\text{m}$  below the wafer surface. Consequently, the lifting of the conduction band below etched areas also induces confining potentials along the wires at the depth of the superlattice (which also drives a rapid drift of photoelectrons from etched to unetched areas, such that the bulk contribution to signals is mainly from unetched regions). In addition, below the wires (areas not etched) at the depth of the superlattice there is still a weak slope in the conduction band [Fig. 3.1(c)]. A Rashba SOI should be effective here that only depends on the  $x$  and  $y$  component of a  $k$  vector as for the 2DEG case. Here the Rashba parameter  $C_R \propto \langle dV/dz \rangle$  still has a substantial value [24] due to the slope of the conduction band ( $V$  is potential of the bottom of conduction band and  $z$  is growth direction). This results in anisotropic SOI [analogs to Fig. 3.1(a)] when this Rashba term has a similar magnitude as the Dresselhaus SOI for bulk [23].

We therefore conjecture that the observed SDA for a bulk population is due to electrons *around* (*i.e.*, not inside [19]) the superlattice. The Kerr reflection from the superlattice will probe the spin imbalance in its vicinity. Most likely, this population is located in the accumulation layer [Fig. 3.1(c)] since the thickness of this layer is sufficient for absorbing most of the energy from our laser pulses. The separation into two distinct spin populations can then only be explained if we assume the surprisingly low mobility for photo-electrons along the growth direction that was recently reported [25]. We can therefore not fully rule out scenarios where the bulk response is dominated by electrons at the substrate side of the superlattice, given that these low mobility values are not yet fully understood [19].

### 3.4 Summary of numerical simulations

To investigate the above scenario, we use a simple model and Monte Carlo simulations as for 2DEG-based wires [15]. The short summary presented here is based on the work presented in *Chapter 4* and *Chapter 5*. We model a wire of bulk material by assuming a randomly moving electron ensemble with a three-dimensional  $k$  vector distribution that is confined to a rectangular elongated box with short sides of  $1 \mu\text{m}$ . The electrons are scattering on the edge of the box and on impurities (mean-free path from impurities alone set at  $1 \mu\text{m}$ , *i.e.*, a quasibalistic electron ensemble). The (quasi-)Fermi level is derived from the estimated photo-electron density around the superlattice ( $\sim 3 \cdot 10^{21} \text{ m}^{-3}$ ). Spins are precessing around the sum of anisotropic spin-orbit fields and the external field. We assume the electron spins experience only the bulk Dresselhaus SOI Ref.([2]), and the mentioned Rashba SOI. Dephasing is again purely due to the DP mechanism. Such numerics indeed produces dephasing times similar to the observed values. Also, it shows SDA as a function of wire orientation with the slowest dephasing for wires along [110] and with the ratio between  $\tau_2$  for [110] and [-110] wires close to 3 for  $B = 0 \text{ T}$ .

### 3.5 Effect of external magnetic field on spin dephasing anisotropy

As an extra point we discuss the magnetic field dependence of SDA for the 2DEG and bulk populations. For both, the SDA (taken as the ratio between dephasing times for [110] and [-110] wires, see Figs. 3.3(b) and 3.3(c)) is most apparent at zero external field, and degrades with increasing field. Our type of SDA only occurs in quasi-1D systems, *i.e.*, when the width of the wires is less than the spin precession length  $L_{sp}$  [15]. Alternatively, it can degrade when an external field starts to dominate over anisotropic spin-orbit fields [Fig. 3.1(a)]. The degradation of SDA of the bulk population is consistent with both explanations. The external field drives  $L_{sp}$  below  $\sim 1 \mu\text{m}$  for  $B \approx 4 \text{ T}$  (using again the estimated density of photo-electrons around the superlattice) but we also estimate [3] that the external field dominates over spin-orbit fields above  $B \approx 0.3 \text{ T}$ . For the 2DEG a much stronger field is needed for driving  $L_{sp} \lesssim 1 \mu\text{m}$ , but the external field dominates over spin-orbit fields for  $B > 4 \text{ T}$  [3]. We repeated all measurements with the external field in [-110] direction. We observed small shifts ( $\sim 10\%$ ) in the dephasing times, but the  $B$  dependence of SDA was at nearly the same

level. We interpret this as follows. Having only partial cancellation of SOI (not the pure case  $C_{D1} = C_R$ ) gives anisotropy for SOI with fields varying both in magnitude and direction. This still gives SDA, but it can be lifted by adding an external field that is stronger than the spin-orbit fields, and there is then little dependence on the direction of the field. Our Monte-Carlo simulations confirm this behavior, and give SDA values that degrade from  $\sim 3$  at  $B = 0$  T to  $\sim 2$  at 7 T.

### 3.6 Effect of temperature and pump power on spin dephasing anisotropy

The dependence on temperature can provide more insights in the spin dephasing anisotropy, since the spin dephasing time of bulk and 2DEG changes differently with temperature [17].

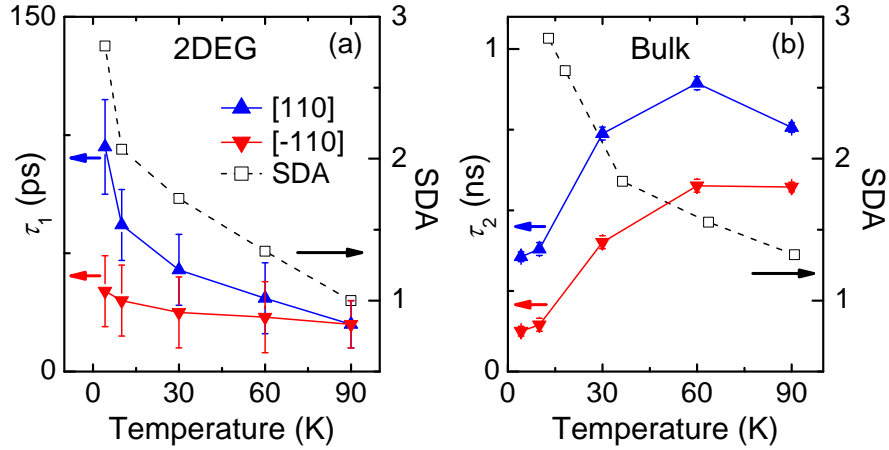


**Figure 3.4:** Effect of temperature on spin-dephasing anisotropy (SDA). [(a) and (b)] The spin dephasing times  $\tau_i$  as a function of  $T$ , for (a) 2DEG and (b) bulk electrons. These plots also present SDA quantified as  $\tau_{i,[110]}/\tau_{i,[-110]}$ .

The measurements were performed at a few different temperatures for the case zero external magnetic field. The spin dephasing anisotropy is decaying with increasing temperature for both: 2DEG and bulk. However, 2DEG and bulk show an opposite trend for the actual values of the spin dephasing times. While the spin dephasing time of 2DEG is rapidly decreasing with temperature, the bulk exhibits the opposite behavior. This can be explained by the effective

change in spin precession length due to temperature dependence of the electron mobility.

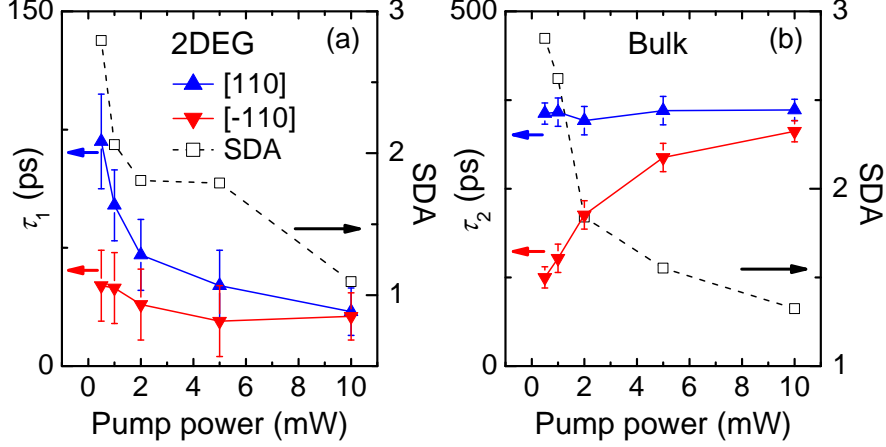


**Figure 3.5:** Effect of excited electron density tuned by means of the pump power. [(a) and (b)] The spin dephasing times  $\tau_i$  as a function of pump power, for (a) 2DEG and (b) bulk electrons. These plots also present SDA quantified as  $\tau_{i,[110]}/\tau_{i,[-110]}$ .

Increasing the number of photo-excited (spin polarized) carriers also strongly affects the spin dephasing anisotropy. For low pump powers (where the number of photo-excited electrons is comparable to the number of electrons already present in the 2DEG) the previous picture of the spin dephasing anisotropy mechanism holds. For higher excitation densities (above roughly 2 mW of pump power) the number of photo excited carriers exceeds the number of native electrons in the system. This generates a strong self-screening effect, which reduces the mobility in a transient manner (due to electron-hole recombination at a timescale of about 300 ps). Having such a process in the sample strongly affects the dynamics of the ensemble of spin, which can no longer be considered as a ballistic electron ensemble in a wire with fixed transport properties over the measurement period. Strong pumping also increases the effective temperature in the system and this contributes to the reduction of the SDA when increasing the pump powers.

As a conclusion, we note that the results of the study of the temperature dependence and the pump-power dependence are consistent with our interpretation of having an SDA effect for both a 2DEG and a bulk population in the system.

## 3.7 Conclusions

In conclusion, our results confirm that confining electron ensembles in quasi-1D wires in [110] direction can yield suppressed spin dephasing. The results agree with predictions based on anisotropy for SOI. Further studies with tuning of SOI by a gate gives access to better cancellation of Rashba and Dresselhaus SOI, and can explore the ultimate limit of suppressing dephasing in wires [4, 15]. Such gate control can also yield spin-transistor functionality [1] by associating *on* and *off* with strong or little dephasing of spin signals. Our results also establish that using SDA for suppressing dephasing is not restricted to quantum-well electron ensembles. It is also applicable to quasi-1D ensembles in bulk-like layers where the conduction band has a slope. Our results thus open the path to investigating the mentioned spin-transistor functionality for bulk semiconductor channels [26].

We thank R. Winkler and A. Rudavskiy for discussions, and the Dutch NWO and NanoNed, and the German programs DFG-SFB 491, DFG-SPP 1285 and BMBF nanoQUIT for financial support.

## References

- [1] D. D. Awschalom and N. Samarth, *Physics* **2**, 50 (2009).
- [2] For a review see R. H. Silsbee, *J. Phys. Condens. Matter* **16**, R179 (2004).
- [3] J. B. Miller, D. M. Zumbuhl, C. M. Marcus, Y. B. Lyanda-Geller, D. Goldhaber-Gordon, K. Campman, and A. C. Gossard, *Phys. Rev. Lett.* **90**, 076807 (2003).
- [4] J. D. Koralek, C. P. Weber, J. Orenstein, B. A. Bernevig, S. C. Zhang, S. Mack, and D. Awschalom, *Nature (London)* **458**, 610 (2009).
- [5] N. S. Averkiev and L. E. Golub, *Phys. Rev. B* **60**, 15582 (1999).
- [6] J. Schliemann, J. C. Egues, and D. Loss, *Phys. Rev. Lett.* **90**, 146801 (2003).
- [7] B. A. Bernevig, J. Orenstein, and S.-C. Zhang, *Phys. Rev. Lett.* **97**, 236601 (2006).
- [8] J. L. Cheng, M. W. Wu, and I. C. da CunhaLima, *Phys. Rev. B* **75**, 205328 (2007).
- [9] M. Duckheim and D. Loss, *Phys. Rev. B* **75**, 201305(R) (2007).

- 
- [10] N. S. Averkiev, L. E. Golub, A. S. Gurevich, V. P. Evtikhiev, V. P. Kochereshko, A. V. Platonov, A. S. Shkolnik, and Y. P. Efimov, *Phys. Rev. B* **74**, 033305 (2006).
- [11] T. Korn, D. Stich, R. Schulz, D. Schuh, W. Wegscheider, and C. Schller, *Physica E* **40**, 1542 (2008).
- [12] A. W. Holleitner, V. Sih, R. C. Myers, A. C. Gossard, and D. D. Awschalom, *Phys. Rev. Lett.* **97**, 036805 (2006).
- [13] Y. Kunihashi, M. Kohda, and J. Nitta, *Phys. Rev. Lett.* **102**, 226601 (2009).
- [14] S. M. Frolov, S. Lscher, W. Yu, Y. Ren, J. A. Folk, and W. Wegscheider, *Nature (Londen)* **458**, 868 (2009).
- [15] J. Liu, T. Last, E. J. Koop, S. Denega, B. J. van Wees, and C. H. van der Wal, *J. Supercond. Novel. Magn.* **23**, 11 (2010).
- [16] Y. Kunihashi, M. Kohda, and J. Nitta, *Physics Procedia* **3**, 1255 (2010).
- [17] J. M. Kikkawa and D. D. Awschalom, *Phys. Rev. Lett.* **80**, 4313 (1998).
- [18] We checked that grating behavior of the arrays did not influence Kerr signals, by rotating the polarization planes of the pump and probe beam around their axes.
- [19] P. J. Rizo, A. Pugzlys, A. Slachter, S. Z. Denega, D. Reuter, A. D. Wieck, P. H. M. van Loosdrecht, and C. H. van der Wal, *New J. Phys.* **12**, 113040 (2010).
- [20] We observe that using phases  $\phi_i$  as free parameters is needed for obtaining good fits. We only use data from delays  $t > 5$  ps, since holes contribute to the Kerr signals up to  $t \approx 5$  ps. For  $t < 5$  ps there is also rapid relaxation of electron kinetic energy, which can contribute to apparent phase offsets for  $t > 5$  ps [19].
- [21] M. J. Snelling, G. P. Flinn, A. S. Plaut, R. T. Harley, A. C. Tropper, R. Eccleston, and C. C. Phillips, *Phys. Rev. B* **44**, 11345 (1991).
- [22] D. Stich, J. Zhou, T. Korn, R. Schulz, D. Schuh, W. Wegscheider, M. W. Wu, and C. Schuller, *Phys. Rev. Lett.* **98**, 176401 (2007).
- [23] We analyzed that SOI due to possible presence of wire-induced strain cannot explain the observed SDA.
- [24] As compared to the 2DEG case, where the slope in  $V$  for the GaAs layer is compensated by the steep increase in  $V$  at the heterojunction, since 2DEG states penetrate the AlGaAs layer (Fig. 3.1(c)).

- [25] G. Salis and S. F. Alvarado, Phys. Rev. Lett. **96**, 177401 (2006).
- [26] S. P. Dash, S. Sharma, R. S. Patel, M. P. de Jong, and R. Jansen, Nature **462**, 491 (2009).

## Chapter 4

# Spin-dephasing anisotropy for 2D electrons in a diffusive quasi-1D GaAs wire

### Abstract

We present a numerical study of dephasing of electron spin ensembles in a diffusive quasi-one-dimensional GaAs wire due to the D'yakonov-Perel' spin-dephasing mechanism. For widths of the wire below the spin precession length and for equal strength of Rashba and linear Dresselhaus spin-orbit fields a strong suppression of spin-dephasing is found. This suppression of spin-dephasing shows a strong dependence on the wire orientation with respect to the crystal lattice. The relevance for realistic cases is evaluated by studying how this effect degrades for deviating strength of Rashba and linear Dresselhaus fields, and with the inclusion of the cubic Dresselhaus term.

---

This chapter is based on Ref. 5 on p. 103.

## 4.1 Introduction

The ability to maximize the spin-dephasing time  $T_2^*$  of an electron spin ensemble is one of the key issues for developing semiconductor-based spintronic devices [1, 2]. However, in all III-V semiconductor materials spin ensembles rapidly dephase due to the D'yakonov-Perel' (DP) spin-dephasing mechanism [3, 4]. For the case of electron ensembles in a heterojunction two-dimensional electron gas (2DEG), two distinct contributions to DP spin-dephasing have to be considered: the inversion asymmetry of the confining potential (structural inversion asymmetry) and the bulk inversion asymmetry of the crystal lattice. The former results in an effective Rashba field and the latter in an effective Dresselhaus field, which includes linear and cubic contributions [3, 5, 6, 4]:

$$\vec{B}_R = C_R (\hat{x}k_y - \hat{y}k_x), \quad (4.1)$$

$$\vec{B}_{D1} = C_{D1}(-\hat{x}k_x + \hat{y}k_y), \quad (4.2)$$

$$\vec{B}_{D3} = C_{D3}(\hat{x}k_xk_y^2 - \hat{y}k_x^2k_y), \quad (4.3)$$

where  $\hat{x}$ ,  $\hat{y}$  are the unit vectors along the [100] and [010] crystal directions,  $k_x$ ,  $k_y$  are the components of the in-plane wave vector, and  $C_{R,D1,D3}$  are the spin-orbit coupling parameters. The total effective spin-orbit field  $\vec{B}_{eff}$  is the vector sum of all three contributions. For 2D and quasi-1D electron systems, the direction and magnitude of these effective spin-orbit fields can be illustrated as arrows on the Fermi circle. Figure 4.1 presents this for selected points in the 2D momentum space, for the Rashba (a) and linear Dresselhaus (b) field alone, and their sum (c) for the case of equal strength of Rashba and linear Dresselhaus field. In contrast to the individual cases (Fig. 4.1 (a), (b)), the magnitude of the vector sum shows a strong anisotropy in momentum space (Fig. 4.1 (c)). This already suggests that spin dephasing in very narrow wires in which electron motion is restricted to the [110] direction can be strongly reduced as compared free 2DEG or such wires oriented along other crystal directions. However, it is harder to analyze whether such a dephasing anisotropy also occurs for wider quasi-1D wires, where the motion in the 2DEG plane is still completely random and diffusive, but where the width of the wire is less than length scales as the spin precession length or the mean free path. For the latter case the transport regime could be named quasi-ballistic, but we consider the case of a large ensemble where transport along the wire is still diffusive, and where the width of the wire in the 2DEG plane is much wider than the regime of quantum confinement. Initial studies of such spin-dephasing anisotropy include a recent experiment [7] on wires, and the-

oretical work on drifting ensembles in free 2DEG [8]. However, until now most emphasis was on work related to the spin field-effect transistor [9], using InAs-based systems or highly asymmetrical heterojunctions, where structural inversion asymmetry dominates the spin-orbit interaction [10, 11, 12, 13, 14].

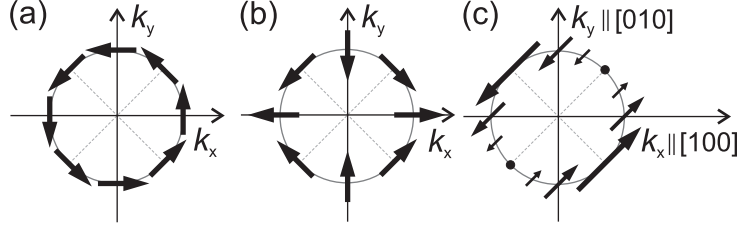


**Figure 4.1:** A schematic representation of the direction and magnitude of the effective magnetic field for selected points in a two-dimensional  $k$ -space, sketched for (a) the Rashba field, (b) the linear Dresselhaus field and for (c) the symmetric case of the sum of equal Rashba and linear Dresselhaus field. Both the magnitude and direction are depicted as arrows on the Fermi circle with radius  $k_F$  in the  $(k_x, k_y)$ -plane.

We report here how the D'yakonov-Perel' spin dephasing mechanism can be strongly suppressed in diffusive quasi-1D electron systems based on GaAs heterojunction material, for which Rashba and linear Dresselhaus spin-orbit contributions can be indeed of comparable magnitude [4, 7]. The dephasing is studied for spin ensembles initially aligned perpendicular to the plane of the wire ([001] direction). This situation reflects the method of preparing and interrogating a spin population via optical pump-probe techniques [2]. Our numerical calculation is first performed for conditions with equal Rashba and linear Dresselhaus contributions and the cubic Dresselhaus term set to zero. For widths of the diffusive quasi-1D wires smaller than the spin precession length the DP spin-dephasing mechanism can be strongly suppressed and the spin-dephasing time  $T_2^*$  is considerably enhanced if the wire is aligned along the direction of zero effective spin-orbit field. Moreover, we want to point out that the value of our numerical tool lies in the opportunity to study such phenomena also for more realistic conditions. Thus, we can study how breaking the equality of the Rashba and linear Dresselhaus spin-orbit fields, or adding the cubic Dresselhaus term leads to a degradation of the spin-dephasing anisotropy.

## 4.2 Method

We apply a Monte Carlo method [15] to study the temporal evolution of the normalized spin orientation (average spin expectation value) in an elongated quasi-1D wire. Our numerical tool is based on a semiclassical approach. We use a classical description for the electron motion, and a quantum mechanical description of the dynamics of the electron spin. The wire is treated as a rectangular box of aspects 1  $\mu\text{m}$  and 200  $\mu\text{m}$ . The electron density and mobility are set to  $4 \cdot 10^{15} \text{ m}^{-2}$  and  $100 \text{ m}^2/\text{Vs}$ , which are typical values for a GaAs/AlGaAs heterojunction material. All electrons are assumed to have the same Fermi velocity  $v_F$  of  $2.7 \cdot 10^5 \text{ m/s}$ . This is a valid approximation for  $k_B T, \Delta E_{Z,SO} \ll E_F$  (with respect to the bottom of the conduction band), where  $\Delta E_{Z,SO}$  is the Zeeman splitting due to the spin-orbit fields alone. Electron-electron interaction and inelastic scattering mechanisms are neglected.

The electron is regarded as a point particle which moves on a classical trajectory between scatter events on impurities (randomly determined at a rate to obtain an average scatter time of 38 ps) yielding diffusive behavior in the ensemble (electron mean free path  $L_p = v_F \tau_p = 10 \mu\text{m}$ ), and specular scattering on the edges of the wire. For each electron moving on such a ballistic trajectory we calculate the spin evolution in the effective spin-orbit fields quantum mechanically, and we then take the ensemble average on a set of electrons with random initial position and momentum direction.

Within a straight ballistic segment of an electron trajectory the spin rotates around  $\vec{B}_{eff}$  over a precession angle given by

$$\phi_{prec} = \frac{g\mu_B |\vec{B}_{eff}|}{\hbar} t, \quad (4.4)$$

where  $\hbar$  is the reduced Planck's constant and  $t$  the time of traveling through the segment. The spin rotation operator  $\hat{U}$  for rotation over the precession angle  $\phi_{prec}$  about the direction  $\vec{u}$  (unit vector) of the effective magnetic field  $\vec{B}_{eff}$  is obtained by (see e.g. [16])

$$\hat{U} = \exp\left(-i \frac{\phi_{prec}}{2} \vec{\sigma} \vec{u}\right) = \begin{pmatrix} \cos \frac{\phi_{prec}}{2} - i u_z \sin \frac{\phi_{prec}}{2} & -(i u_x + u_y) \sin \frac{\phi_{prec}}{2} \\ -(i u_x - u_y) \sin \frac{\phi_{prec}}{2} & \cos \frac{\phi_{prec}}{2} + i u_z \sin \frac{\phi_{prec}}{2} \end{pmatrix} \quad (4.5)$$

where  $\vec{\sigma}$  represents the vector of Pauli spin matrices (x, y, z components of the spin).  $\hat{U}$  acting on a spin state  $|\Psi_{initial}\rangle$  at the beginning of a ballistic trajectory yields the spin state  $|\Psi_{final}\rangle = \hat{U} |\Psi_{initial}\rangle$  at the end of the trajectory. Thus, we can follow the spin state of each electron (labeled  $i$ ), and we use this to define a

semiclassical spin vector to present its orientation,  $\vec{S}_i = (\langle S_x \rangle_i, \langle S_y \rangle_i, \langle S_z \rangle_i)$  from its spin expectation values in  $x, y, z$  directions.

For an electron experiencing multiple scattering events, the orientation of the effective magnetic field is changed at each scatter event. For each trajectory a rotation is applied. Once a scattering event takes place, the wave vector state is updated,  $\vec{B}_{eff}$  is recalculated based on the new wave vector, resulting in a new rotation operator, and the evolution of the spin state will carry on. For spin ensembles, the randomization will bring a reduction of the normalized spin orientation (average spin expectation value)  $\langle S_r \rangle = \left| (\sum_{i=1}^N \vec{S}_i) / N \right|$  for the ensemble.  $\langle S_r \rangle$  is obtained by averaging over an ensemble of  $N = 1000$  spins, independent of their positions within the system, and calculated as a function of time. We choose to study the spin coherence in the ensemble here as  $\langle S_r \rangle$ . The advantage is that  $\langle S_r \rangle$  gives the magnitude of the residual spin orientation in the direction that is maximum (automatically evaluating the envelope in case the ensemble average shows precession). However, in the present study without externally applied fields, there was no development of average spin orientation in the  $x$  and  $y$  directions, and the decay of  $\langle S_r \rangle$  always equaled the decay of ensemble average  $\langle S_z \rangle = (\sum_{i=1}^N \langle S_z \rangle_i) / N$ . The spin-dephasing time  $T_2^*$  of the ensemble is defined as the decay time over which  $\langle S_r \rangle$  reduces to  $1/e$  of its initial value. Note, however, that decay traces of  $\langle S_r \rangle$  were not always mono exponential in our simulations.

### 4.3 Results and discussion

The temporal evolution of the normalized spin orientation  $\langle S_r \rangle$  is studied for out-plane initial spin states oriented along the [001] direction. The effective spin-orbit field resulting from equal magnitudes of the Rashba and linear Dresselhaus fields is always parallel to the [110] axis ( $C_R = C_{D1} = -1.57 \cdot 10^{-8}$  Tm, [4]). These values of the spin-orbit parameters give rise to an average spin precession length of about  $3 \mu\text{m}$ . The width of our wire of  $1 \mu\text{m}$  is chosen to be smaller than this length scale.

The inset of Fig. 4.2 shows the temporal evolution for five different orientations of the quasi-1D wire with respect to the [100] direction. A distinct anisotropy of the spin dephasing times is observed. The peak value of  $T_2^*$  is reached when the wire is oriented exactly along the [110] direction. It is found to be in excess of  $10^4$  ps. This agrees with the result  $T_2^* = \infty$ , which can be derived analytically for this ideal case [17]. Yet, a deviation of only  $5^\circ$  in the wire orientation with respect to the [110] direction leads to a reduction of  $T_2^*$  of more than an order

of magnitude towards a value of about 200 ps. For angles close to  $[110] \pm 15^\circ$  the spin-dephasing time drops already to 43 ps and it reaches a minimum of 9 ps for wires oriented along the  $[\bar{1}10]$  and  $[1\bar{1}0]$  direction. A detailed summary of these findings is presented in Fig. 4.2 where the extracted spin-dephasing times are plotted as a function of the wire orientation. This plot reveals the strong anisotropy of  $T_2^*$  with respect to the crystal axes.

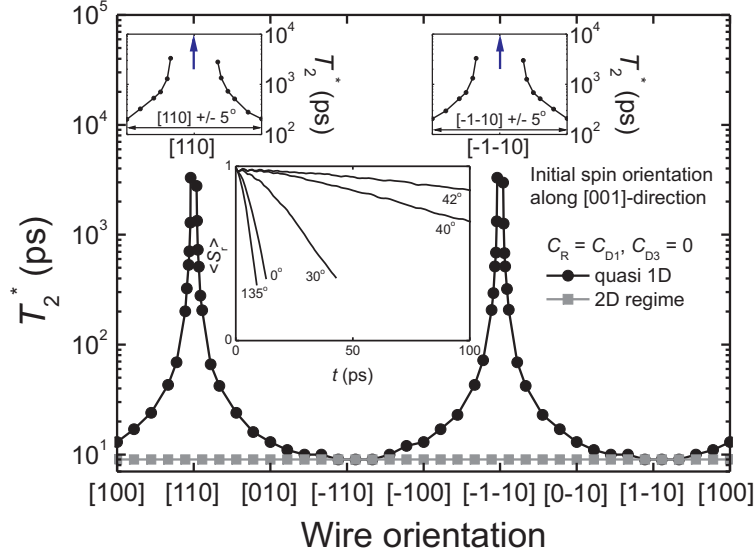


**Figure 4.2:** The spin-dephasing time  $T_2^*$  of a spin ensemble is plotted as a function of the wire orientation with respect to the  $[100]$  lattice direction. The ensemble is initially oriented along the  $[001]$  direction.  $T_2^*$  is strongly enhanced for a quasi-1D wire oriented in the  $[110]$  direction (black) as compared to an ensemble in a 2D system (gray). The arrows (in the top insets, horizontal axes span  $\pm 5^\circ$ ) for data at  $45^\circ$  and  $225^\circ$  indicate that here  $T_2^*$  is larger than could be calculated ( $C_R = C_{D1} = -1.57 \cdot 10^{-8}$  Tm,  $C_{D3} = 0$ ). Inset: Ensemble spin expectation value  $\langle S_r \rangle$  as a function of time for different wire orientations.

The anisotropy of  $T_2^*$  is directly connected to the motion of single electrons within the ensemble. Specular edge scattering implies that electrons with a solely transverse momentum component to the wire orientation (traveling less than the spin precession length between scatter events) almost do not contribute to the spin-dephasing because of motional narrowing. Only electrons with a strong momentum component longitudinal to the wire orientation are contributing to the dephasing of the spin ensemble. This results in the strong enhancement of  $T_2^*$  for wires in the  $[110]$  direction.

Spin-dephasing times for non-confined spin ensembles (wire width taken much wider than the mean free path and spin precession length) are also calculated (gray, Fig. 4.2). In contrast to the quasi-1D wire case, no spin-dephasing anisotropy is found. We investigated the crossover from 2D to quasi 1D behavior for a wide range of values for the spin precession length and mean free path (with respect to the wire width), and found that the spin precession length is the crucial length scale which is governing this crossover.

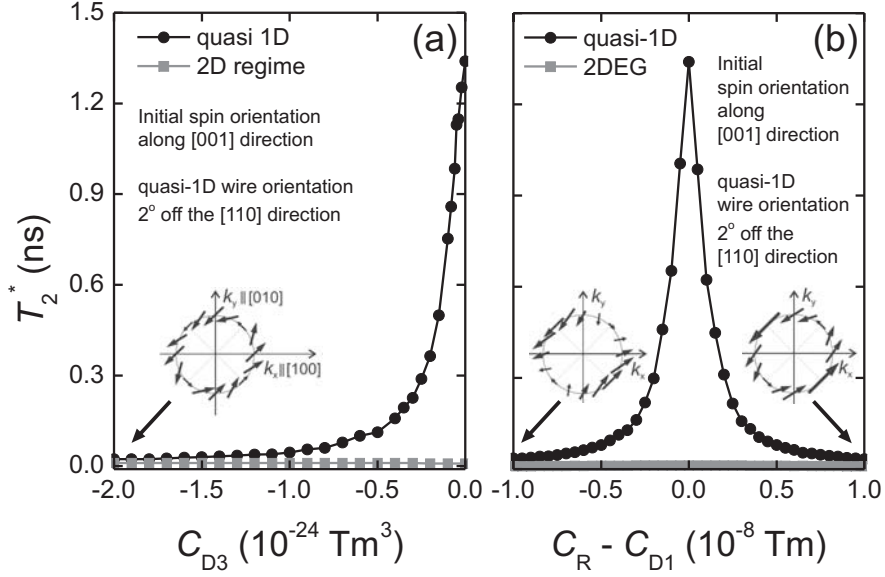


**Figure 4.3:** Data shows how the  $T_2^*$  enhancement of Fig. 4.2 reduces when the cubic Dresselhaus term is added and when the symmetry between  $C_R$  and  $C_{D1}$  is lifted. The initial spin state is chosen to be along [001] direction and the quasi-1D wire is set at  $43^\circ$  with respect to the [100] direction. The case of  $43^\circ$  wire orientation (rather than  $45^\circ$ ) avoids the need to deal in calculations with extremely long  $T_2^*$  for the symmetric case of  $C_R = C_{D1}$  and  $C_{D3} \approx 0$ , while still clearly showing the 1D  $T_2^*$  enhancement. (a) The effect of the cubic Dresselhaus term on  $T_2^*$  is plotted for the 2D case (gray) and for the quasi-1D case (black) ( $C_R = C_{D1} = -1.57 \cdot 10^{-8} \text{ Tm}$ ). (b)  $T_2^*$  is plotted here against the difference  $C_R - C_{D1}$ , at the fixed value of  $C_{D1} = -1.57 \cdot 10^{-8} \text{ Tm}$  for the 2D case (gray) and for the quasi-1D case (black) ( $C_{D3} = 0$ ).

Next, we discuss whether this distinct spin-dephasing anisotropy in quasi-1D wires (with a strong enhancement of  $T_2^*$  for wires in the [110] direction as a fingerprint) can be maintained under more realistic circumstances. First we study the influence of adding the cubic Dresselhaus term on the enhancement of  $T_2^*$ . Secondly, the influence of deviating strength of Rashba and linear Dresselhaus

fields will be discussed. To avoid the difficulty that  $T_2^*$  cannot be calculated for  $45^\circ$  with respect to the [100] direction within reasonable calculation time, we take  $43^\circ$  as a test case, as this already shows a very strong  $T_2^*$  enhancement, while  $T_2^*$  is limited to nanoseconds. Hence, the calculated spin-dephasing times in the following part can be seen as lower bounds.  $T_2^*$  for the exact [110] direction is expected to be distinctively higher.

The effect of the additional cubic Dresselhaus term on the spin dephasing time in the quasi-1D wire is presented in Fig. 4.3 (a). Again, the 2D case is plotted as a reference (gray). Without the cubic Dresselhaus term the calculation results in a  $T_2^*$  of 1.3 ns. However, the spin-dephasing time is decreasing rapidly with increasing Dresselhaus parameter. For  $C_{D3} = -7 \cdot 10^{-25} \text{ Tm}^3$ ,  $T_2^*$  is already reduced to 78 ps. To estimate whether the spin-dephasing anisotropy is still present in a more realistic situation, experimentally deduced parameters are applied for comparison with our calculations. In [4] a value of  $C_{D3} = -1.18 \cdot 10^{-24} \text{ Tm}^3$  is evaluated which results in a  $T_2^*$  of only 40 ps. A value which is less than an order of magnitude higher than the value calculated for the 2D case. This points to the conclusion that the cubic Dresselhaus term nearly annihilates the spin-dephasing anisotropy. However,  $C_{D3}$  depends strongly on the electron density of the system. For samples with lower densities  $C_{D3}$  is orders of magnitude smaller [4, 18, 19]. Considering those values, it turns out, that there is a much weaker decay of the peak value of the spin-dephasing time, even when the cubic Dresselhaus term is included.

Finally,  $T_2^*$  is investigated for deviating Rashba and linear Dresselhaus contributions. This dependence is summarized in Fig. 4.3 (b) where  $T_2^*$  is plotted as a function of the difference in strength of the Rashba and linear Dresselhaus parameter,  $(C_R - C_{D1})$ , in the interval  $\pm 1 \cdot 10^{-8} \text{ Tm}$  for  $C_{D1}$  fixed at  $-1.57 \cdot 10^{-8} \text{ Tm}$ . At  $C_R - C_{D1} = 0$  this results in the previously calculated  $T_2^*$  of around 1.3 ns. With either increasing  $|C_R|$  or increasing  $|C_{D1}|$ ,  $T_2^*$  is decaying equally fast.  $C_R$  and  $C_{D1}$  taken from [4] result in a difference  $C_R - C_{D1}$  of  $0.4 \cdot 10^{-8} \text{ Tm}$ . For this value our calculated  $T_2^*$  is already considerably reduced to about 110 ps. However, this spin dephasing time is still an order of magnitude higher than the one resulting from the 2D case and in addition,  $C_R$  can be tuned with a gate or heterostructure design to equalize it to the linear Dresselhaus field. Therefore, in summary, it can be stated that the spin-dephasing anisotropy which is very distinct for  $C_R$  and  $C_{D1}$  exactly equal can still prevail under less ideal conditions.

## 4.4 Conclusions

A useful numerical tool is developed for studying spin-dephasing in device structures due to the D'yakonov-Perel' spin-dephasing mechanism. The Rashba, linear and cubic Dresselhaus contributions can be taken into account. With this tool it was demonstrated that quasi-1D wires (narrower than the spin precession length, but with diffusive 2D motion for the electron ensemble) can show very clear signatures of spin-dephasing anisotropy, with a strong suppression of spin dephasing for wires in the [110] crystal direction.

We acknowledge financial support from the Dutch Foundation for Fundamental Research on Matter (FOM), the Netherlands Organization for Scientific Research (NWO) and one of us (T. Last) acknowledges financial support by the Dutch Nanotechnology Program NanoNed.

## References

- [1] For a review: D. D. Awschalom, D. Loss, and N. Samarth (Eds), *Semiconductor Spintronics and Quantum Computation*, Springer, Berlin 2002.
- [2] J. M. Kikkawa and D. D. Awschalom, *Phys. Rev. Lett.* **80**, 4313 (1998).
- [3] M. I. D'yakonov and V. Yu. Kachorovskii', *Fiz. Tekh. Poluprovodn.* (S.-Peterburg) **20**, 178 (1986); [*Sov. Phys. Semicond.* **20**, 110 1986].
- [4] J. B. Miller, D. M. Zumbühl, C. M. Marcus, Y. B. Lyanda-Geller, D. Goldhaber-Gordon, K. Campman and A. C. Gossard, *Phys. Rev. Lett.* **90**, 076801 (2003).
- [5] Y. A. Bychkov and E. I. Rashba, *Pis'ma Zh. Eksp. Teor. Fiz* **39**, 66 (1984); [*JETP Lett.* **39**, 78 (1984)].
- [6] G. Lommer, F. Malcher and U. Rössler, *Phys. Rev. B* **32**, 6965 (1985).
- [7] S. M. Frolov, A. Venkatesan, W. Yu, S. Lüscher, W. Wegscheider, and J. A. Folk, *Phys. Rev. Lett.* **102**, 116802 (2009).
- [8] M. Duckheim, and D. Loss, *Phys. Rev. B* **75**, 201305(R) (2007).
- [9] S. Datta and B. Das, *Appl. Phys. Lett.* **56**, 665 (1990).
- [10] A. A. Kiselev and K. W. Kim, *Phys. Rev. B* **61**, 13115 (2000).
- [11] T. P. Pareek and P. Bruno, *Phys. Rev. B* **65**, 241305(R) (2002).
- [12] F. Mireles and G. Kirczenow, *Phys. Rev. B* **64**, 024426 (2001).

- [13] S. Pramanik, S. Bandyopadhyay, and M. Cahay, Phys. Rev. B **68**, 075313 (2003).
- [14] A. W. Holleitner, V. Sih, R. C. Myers and D. D. Awschalom Phys. Rev. Lett, **97**, 036805 (2006).
- [15] E. J. Koop, B. J. van Wees, and C. H. van der Wal, arXiv:0804.2968.
- [16] C. Cohen-Tannoudji, B. Diu, F. Laloë, *Quantum Mechanics*, vol. 1, p. 691, John Wiley & Sons (1977).
- [17] J. A. Folk, private communication; J. Liu *et al.*, in preparation.
- [18] B. Jusserand, D. Richards, G. Allan and B. Etienne, Phys. Rev. B **51**, 4707 (1995).
- [19] D. Richards, B. Jusserand, H. Peric, and B. Etienne, Phys. Rev. B **47**, 16028 (1993).

## Chapter 5

# Spin-dephasing anisotropy for electrons in a quasi-1D GaAs wire without quantum confinement

### Abstract

We present a numerical study of the electron-spin dephasing time  $T_2^*$  in quasi-ballistic wires of bulk GaAs material. The study assumes that dephasing occurs due to spin-orbit fields from a bulk Dresselhaus term and a Rashba term in wires with specular momentum scattering on the walls. With a similar magnitude for the Dresselhaus and Rashba effect our results show the longest  $T_2^*$  values for wires in [110] direction. This is consistent with the dependence of  $T_2^*$  on the crystal orientation of wires that was observed in recent experiments. However, a comparison with results for random momentum scattering on the wire edges reveals that the mechanism behind the spin dephasing anisotropy differs from the analogous effect in wires with two-dimensional electron systems. We also studied the magnetic field dependence of this phenomenon with simulations that account for the field-induced cyclotron motion of electrons.

---

This chapter is based on Ref. 1 on p. 103.

## 5.1 Introduction

The spin dephasing of mobile electron ensembles in III-V semiconductors such as GaAs occurs predominantly due to spin precession in spin-orbit fields. These spin-orbit fields are highly anisotropic in momentum space, such that random electron motion within an ensemble results in random precession [1, 2]. For two-dimensional (2D) electron ensembles in quantum wells the spin-orbit effect can be dominated by two terms (see Ref [2] for details): the linear Dresselhaus term (due to a lack of inversion symmetry in the crystal structure) and the Rashba term (due to the inversion symmetry breaking that is associated with the quantum well structure). Such systems can be engineered to give zero spin-orbit fields for electrons with  $k$ -vectors along the [110] direction [3]. This has been central in many theoretical proposals [4, 2, 5, 6, 7, 8] aimed at suppressing spin dephasing. Such a suppression has been observed with quasi-1D wire systems based on 2D GaAs materials [3, 9, 10], where the spin dephasing time showed a dependence on the crystal orientation in the wires.

One of these experiments also showed the unexpected result that the spin dephasing time  $T_2^*$  for electrons in wires based on bulk GaAs also has a dependence on the crystal orientation in the wires [10]. Also here, the longest  $T_2^*$  values were observed for wires along the [110] direction. Initial numerical studies of this effect that were reported in the original publication on the experiment indicated that the spin dephasing anisotropy (SDA) in these wires also relies on a cancellation between spin-orbit terms. In this case, these are the cubic Dresselhaus [11] term and the Rashba term [12]. While the Rashba term is mostly described in the context of 2D electron systems, for micron-thick bulk layers it can also play a role. In the reported experiment there was an unidirectional electric field present in a micron-thick bulk layer near the wafer surface due to band-bending.

We report here further numerical studies on this effect for bulk electrons in quasi-ballistic GaAs wires. In particular, we report a more detailed study of the magnetic field dependence of these effects by including the effect of the external magnetic field on the electron trajectories. While this can be neglected for 2D electron systems with in-plane field, for bulk systems the cyclotron-motion effects are very significant. In addition, we compared in our studies the case of specular and random momentum scattering on the walls of the wires. This revealed that the mechanism behind the spin dephasing anisotropy in wires with specular scattering differs from the analogous effect in wires with 2D electron systems. Instead of a confinement-induced motional-narrowing effect, spin dephasing anisotropy

now results from the interplay between repetitive electron trajectories in the wire and the anisotropy in the spin orbit fields. This points to a mechanism that has similarities with the phenomenon of ballistic spin resonance that can occur in wires based on 2D electron systems [13].

## 5.2 Spin-orbit coupling

For convenience we describe the spin-orbit (SO) coupling as a  $k$ -vector dependent effective magnetic field which acts on the spin of an electron. For III-V semiconductors with zinc-blende crystal structure the SO coupling was derived by G. Dresselhaus [11] and can be expressed in the following form [12]:

$$\vec{B}_D^{bulk} = (2\gamma/g\mu_B) [\hat{x}k_x(k_y^2 - k_z^2) + \hat{y}k_y(k_z^2 - k_x^2) + \hat{z}k_z(k_x^2 - k_y^2)], \quad (5.1)$$

where  $\mu_B$  is the Bohr magneton,  $g$  is the  $g$  factor for an electron in the conduction band and  $\gamma$  is the strength of the SO interaction. The link to the crystallographic axes is represented by the unit vectors  $\hat{x}$ ,  $\hat{y}$  and  $\hat{z}$  which are in the directions [100], [010] and [001], respectively.

For the two-dimensional case with quantum confinement along the  $z$  direction in a quantum well of width  $a$ ,  $\langle k_z \rangle = 0$ . However, the electrons are then in a state with a very significant value for  $\langle k_z^2 \rangle \approx (\pi/a)^2$ . The Dresselhaus SO field can then be expressed in the form of two terms with a different power dependence on  $k$ . It yields the linear Dresselhaus term, which dominates in the limit of  $(\pi/a)^2 \gg k_x^2 + k_y^2$ ,

$$\vec{B}_{D1} = (2\gamma/g\mu_B) \left(\frac{\pi}{a}\right)^2 [-\hat{x}k_x + \hat{y}k_y]. \quad (5.2)$$

The cubic Dresselhaus term for the case of such a quantum well system is

$$\vec{B}_{D3} = (2\gamma/g\mu_B) [\hat{x}k_xk_y^2 - \hat{y}k_yk_x^2]. \quad (5.3)$$

The value for the coupling parameter is taken from Ref. [14],  $2\gamma/g\mu_B = -1.18 \cdot 10^{-24} \text{ Tm}^3$ . In the presence of structural asymmetry (such as asymmetry in the confinement potential of a quantum well) the electrons will also experience the Rashba SO field, given by [12]

$$\vec{B}_R = C_R [\hat{x}k_y - \hat{y}k_x]. \quad (5.4)$$

The value of the  $C_R$  is different for different structures, since it is a geometry dependent parameter. Notably, for quantum wells in GaAs it can produce a

contribution to the total effective SO field that has the same order of magnitude as the linear Dresselhaus term [14].

An electron in such material experiences the vector sum of all these contributions to the SO field, and its spin is precessing accordingly. In the case with also an externally applied magnetic field present, the spin precesses in the vector sum of the total SO field and the external field. The principal difference between the effective magnetic field from SO interaction and the externally applied magnetic field is that the SO field does not affect the motion of the electron and only interacts with the spin (when neglecting higher order relativistic corrections). An externally applied magnetic field, however, also couples to the electron orbit and induces cyclotron motion for the mobile electrons in the material. This effect of the external  $B$ -field on the electron motion can be nearly absent for electron states with strong quantum confinement. The confinement energy can then forbid the orbits to form, as for example in the case of a magnetic field in the plane of a narrow quantum well). The formation of cyclotron orbits is further discussed in the Methods section.

### 5.3 Method

Our numerical approach is based on a semi-classical picture for the electron motion in the material. Electrons are assumed to move with Fermi velocity (independent of the momentum direction). They never escape the region of the interest as they scatter on the walls elastically. For smooth wall this will be specular scattering, while elastic scattering on a wall with surface roughness is modeled as elastic scattering in a random direction. Electrons also have a probability to scatter inside the volume of interest, which is defined by the mobility. This approximation for electron motion is valid for motion in directions without quantum confinement, and for the case of  $E_F \gg kT, \Delta E_{Zeeman}, E_{SO}$ . For a more detailed explanation of approach, the basic model and assumptions were refer to *Chapter 4* and our previous work [15, 16]. This work and related results from the Folk group [17, 18] on modeling the spin dynamics in confined structures of material with a two-dimensional electron system showed that this approach is reliable and efficient.

Here we focus on the modeling of the temporal evolution of spin polarization in a three-dimensional electron ensemble that is ballistically confined in a wire (typical dimension is  $1 \mu\text{m}$  by  $1 \mu\text{m}$  by  $200 \mu\text{m}$ ). The total SO field that electrons experience consists of the bulk Dresselhaus term (Eq. 5.1) and the Rashba term

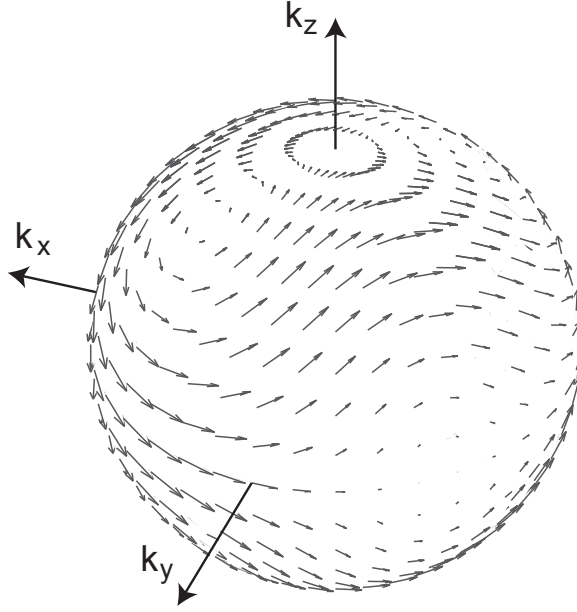


**Figure 5.1:** The total spin-orbit field experienced by electrons with the Fermi velocity, for the case where the contributions  $|\vec{B}_R| = |\vec{B}_D^{bulk}|$  for electrons that move in the  $xy$ -plane. This leads to  $B_{SO}^{total} = 0$  for electrons that move in  $[-110]$  and  $[1-10]$  direction, and for some directions with non-zero  $k_z$ .

(Eq. 5.4). Inclusion of the bulk Dresselhaus term is natural, while the Rashba term for three-dimensional structures is rarely considered. Nevertheless a Rashba-like SO field also appear for structures without a pure two-dimensional nature, since the necessary requirement for having such SO present is hidden in the asymmetry of the potential. A Rashba term should be effective in all cases with a unidirectional electric field in the volume of interest.

In this case, exact cancelation of SO terms is also still possible for specific directions of electron motion. The potential advantage of using three-dimensional structures lies in the possibility of strongly tuning the cancelation of Rashba and Dresselhaus terms by tuning the electron density (which is easy to achieve for the optical experiments in which spin dephasing anisotropy (SDA) was observed [10]). It comes from the fact that  $B_D$  is proportional to  $k^3$ , while the  $B_R$  is linear in  $k$ , and the value of  $k_F$  in the system is defined by the total electron density. An example of the engineered cancelation of SO field is presented in Fig. 5.1.

For the case with no external magnetic field the modeling of such a three-dimensional wire is not very much different from the two-dimensional case (*Chap-*

ter 4). However, the presence of such field with a magnitude that that is of interest in the experiments requires to include the cyclotron motion of an electron. At the same time, the calculation should keep track of the spin precession in the total field (external and SO fields), and check for momentum scattering on the walls of the wire. This extension thus makes the calculations for the 3D case computationally much more demanding than the 2D case. However, the simplicity of this numerical approach on a complex physical situation still has counts as an advantage in comparison with efforts that aim at analytically solving this model.

A necessary requirement for observing SDA in three-dimensional wire is (as for the 2D case) that the spin precession length is smaller than the transverse wire dimension. For our simulations we kept the material parameters at values that yield a spin precession length of about  $\sim 10\mu\text{m}$  in zero external field. In the numerical experiments we vary the wire orientation in the  $xy$ -plane. This is the primary parameter in the search for SDA, that should appear as  $T_2^*$  values that depend on wire orientation. We also vary the electron density, strength of the coupling parameter for the Rashba SO, and the value of the external magnetic field.

## 5.4 Results

We expected non-zero SDA results for 3D wires (based on extrapolating our findings for the 2D case) that would show a maximum  $T_2^*$  for a wire orientation along the direction with the smallest SO fields (all in  $xy$  plane, see for example Fig. 5.1) A wire orientation perpendicular to this direction should then give a minimum  $T_2^*$ . For cancelation of  $B_D$  by a  $B_R$  term as in Fig. 5.1 this would lead to a maximum  $T_2^*$  for wires along the  $[-110]$  direction, and minimum  $T_2^*$  for the  $[110]$  orientation. However, while Fig. 5.1 represents the magnitude and sign for  $B_D$  and  $B_R$  that we estimate for the experimental situation, the expected SDA is then in fact opposite to what was observed in the experiments [10] (both 2D and 3D wires had a peak in  $T_2^*$  for wires in the  $[110]$  direction). This discrepancy is further explored in the Section.

Note that in the three-dimensional case the direction of the SO field cancelation is opposite to that of the two-dimensional case (Fig. 5.2) if we focus only on motion in  $xy$  plane. This comparison is for identical signs for the underlying Dresselhaus and Rashba terms, but the symmetry changes because the effective sign for the Dresselhaus contribution gets reversed (see Eq. (5.1), for the 2D case

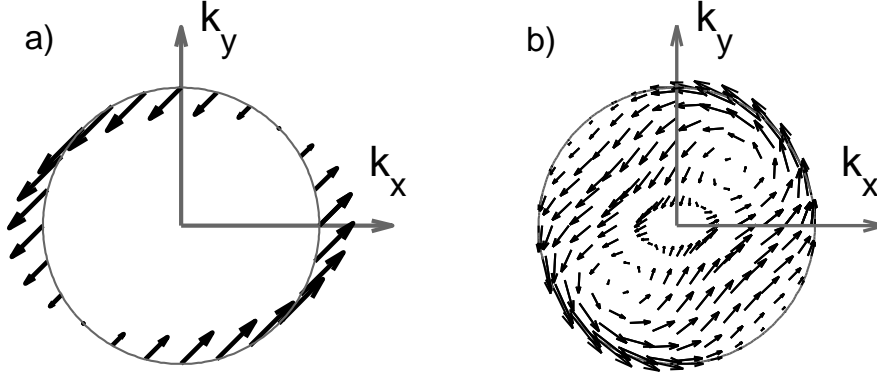


**Figure 5.2:** (a) A schematic representation of the spin-orbit (SO) fields as an effective magnetic field for selected points (Fermi circle with radius  $k_F$  in the  $k_x k_y$ -plane) in a two-dimensional  $k$ -space. The SO field is the sum of the Rashba field and linear Dresselhaus field for the two-dimensional case with exact cancellation for  $k$ -vectors in  $[110]$  direction. (b) A similar representation for selected points in a three-dimensional  $k$ -space (top view onto a Fermi sphere with radius  $k_F$ ), with the total field as the sum of the Rashba field and the bulk (cubic) Dresselhaus field for the three-dimensional case. Both the magnitude and direction of the total SO field are depicted as arrows. For the 2D and 3D case the Rashba term has the same sign, while the Dresselhaus SO field is reversing its sign (in the  $xy$ -plane). This sign flip is due to the fact that for the 2D case  $\langle k_z^2 \rangle \gg k_x^2 + k_y^2$ , while the dominant motion in the  $xy$  plane for the 3D case is carried by electrons with  $k_z \approx 0$  and  $k_z^2 \approx 0$ .

$\langle k_z \rangle = 0$  and  $\langle k_z^2 \rangle \gg k_x^2 + k_y^2$ , while the dominant motion in the  $xy$  plane for the 3D case is carried by electrons with  $k_z \approx 0$  and  $k_z^2 \approx 0$ ). Also the  $SU(2)$  symmetry [5] for the three-dimensional bulk case is not applicable.

### Results for zero external magnetic field

We start the discussion of results with the simulations for zero external magnetic field. Here the electrons move randomly in the wire and experience specular scattering on the edges and random scattering inside the wire. The spin ensemble is prepared in a state that points in the the  $[001]$  direction.

Calculated time traces with the expectation value for spin polarization in the ensemble are presented in the Fig. 5.3. As in *Chapter 4* we plot  $\langle S_r \rangle$  (spin expectation value in the direction that it is maximum) to account for collective spin precession, but for this plot it overlaps with results for  $\langle S_z \rangle$ . The spin expectation

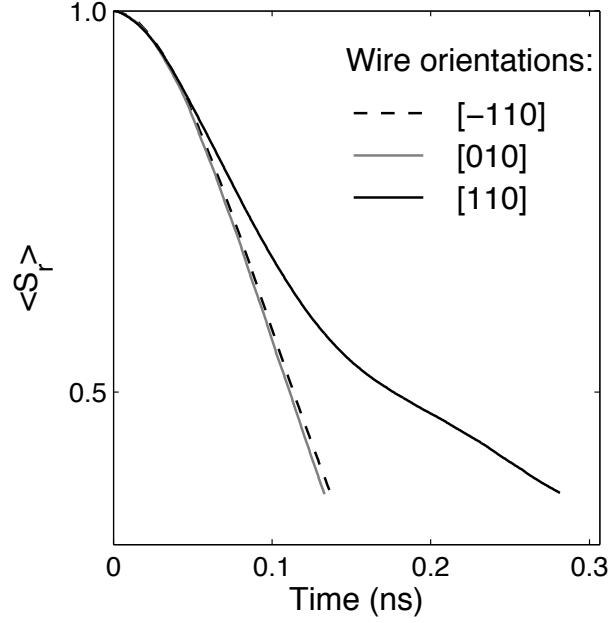


**Figure 5.3:** Ensemble spin expectation value  $\langle S_r \rangle$  as a function of time for different wire orientations.

value for an ensemble is decaying in time due to precessional dephasing in the SO fields. For wires along the [110] direction the spin dephasing is clearly suppressed in comparison with wire in the other directions.

We investigated the  $T_2^*$  values for a range of wire orientations (Fig. 5.4(a)). The wire direction [110] yields the slowest spin dephasing for an electron spin ensemble. Notably, this is consistent with the experimental observations [10], but opposite to our qualitative expectation that the directions on the Fermi sphere with near-zero SO fields determine the direction in which wires give the longest  $T_2^*$  values (as for a 2D case). Thus, this qualitative argument can not explain the results for the 3D case (see Fig. 5.2).

To make a connection to the standard motional narrowing picture [19] we change the scattering on the edges of the wire to non-specular (scattering in a random direction). Results for this case are presented in Fig. 5.4(b). Now the simulations do give the longest  $T_2^*$  values for wires in the [-110] direction, and minimal values for [110] oriented wires. These results are indeed consistent with the motional narrowing mechanism, and simply show the longest  $T_2^*$  for the wire direction where the spin-orbit field is the smallest for electron motion along the wire (and vice versa). Dephasing by the highest SO field values during motion

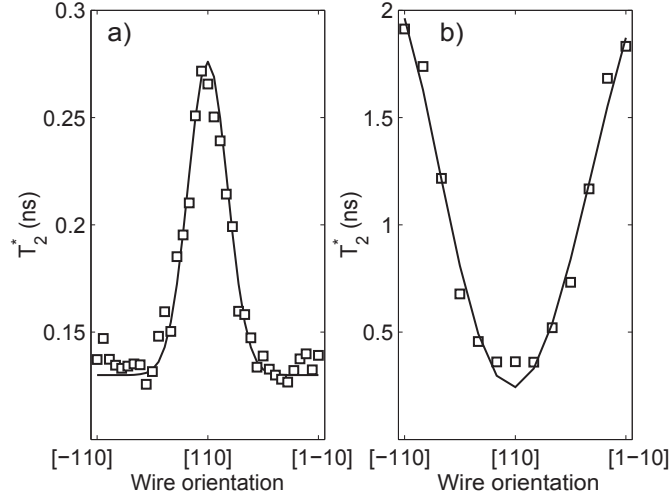


**Figure 5.4:** The spin-dephasing time  $T_2^*$  of a spin ensemble plotted as a function of the wire orientation. (a) For electrons with specular momentum scattering on the edges of the wire. (b) For electrons with non-specular momentum scattering on the edges of the wire.

transverse to the wire direction is suppressed by frequent momentum scattering on the walls.

Additional checks that we performed include specular scattering for a wire with transverse dimensions of  $0.7 \mu\text{m}$  by  $1.4 \mu\text{m}$ . This gave results very close to the SDA as for specular scattering in the wire with  $1 \mu\text{m}$  by  $1 \mu\text{m}$  transverse dimensions. Further, we checked that setting the Rashba term to zero for the case of specular scattering gave  $T_2^* \approx 0.33 \text{ ns}$ , with almost no dependence on wire orientation.

From comparing these cases we conclude that for the case of specular scattering the spin dephasing anisotropy is not due to the confinement enhanced motional-narrowing effect. Instead, it must be due to an interplay between repetitive ballistic electron trajectories (from frequent wall collisions) in the wire and the anisotropy in the spin orbit fields. The mechanism then has similarities with the phenomenon of ballistic spin resonance that can occur in wires based on 2D electron systems [13]. However, here it can already occur when the width of the wire is well below the spin precession length. Studies that can confirm this picture are in progress.

Since the scattering mechanism for wire edges in the real devices is more likely to be specular (due to screening the potential of the edges is smoothed) we further

focus only on this type of the scattering.

It is useful to attribute a numerical value to the SDA. For our further studies we define it as the ratio between the spin dephasing time in a wire along the [110] direction and a wire along the [-110] direction.

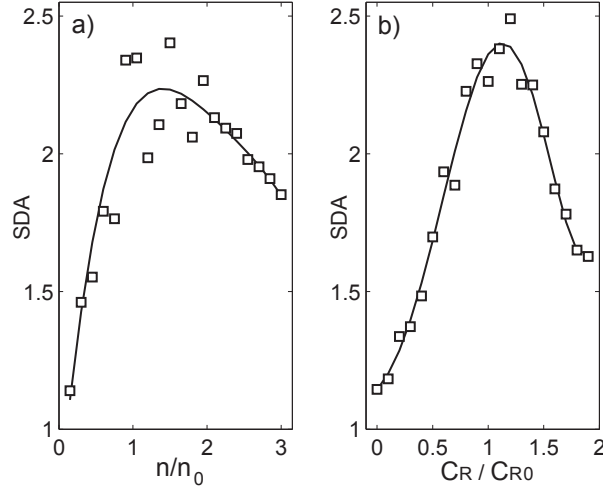


**Figure 5.5:** Spin dephasing anisotropy SDA as a function of simulation parameters. Data points from the numerical experiments are supported by a guide to the eye (solid line). (a) Electron density dependence of the SDA. (b) Dependence of SDA on the relative strength of the Rasha SO field (normalized to the value which yields  $|B_R| = |B_D^{bulk}|$  in the  $xy$ -plane).

To investigate the link between the SDA and exact cancellation of the SO field along the direction perpendicular to the wire we vary two simulation parameters. Results from varying the density of electrons (and thereby  $k_F$ ) in the wire are presented in Fig. 5.5(a). We observe a maximum SDA for the value of the electron density which leads to exactly zero SO field in the direction [-110]. This provides further evidence that the symmetry of the SO fields indeed underlie the SDA. This is further confirmed by results for the SDA as a function of the strength of the Rasha spin-orbit coupling [Fig. 5.5(b)]. We see here similar behavior as in Fig. 5.5(a). The SDA weakens when deviating from values which give exact cancellation of the two SO fields for electrons with  $k$ -vectors in the [-110] direction.

### Magnetic field dependence

We now turn to discussing the results of calculations where the effects of an external magnetic field are included in the model. A first remark is that we

observed that the SDA as in Fig. 5.4 collapses in fields of about 1 Tesla, for any direction of the field. At the same time, we observe that analysis of this collapse is complicated because a richer structure in the dependence of  $T_2^*$  on wire orientation appears.

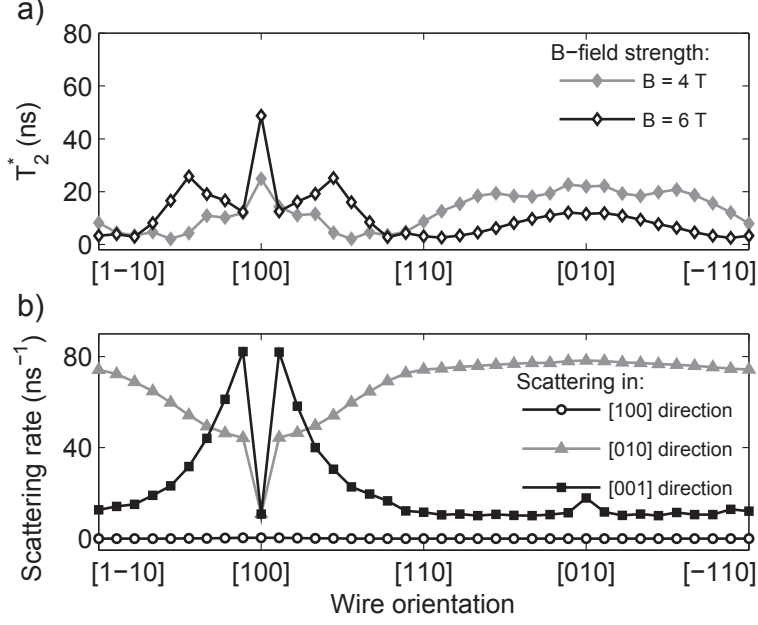


**Figure 5.6:** Spin dephasing time and momentum scattering in wires in an external magnetic field. (a) The spin dephasing time  $T_2^*$  for different wire orientations at 4 Tesla and 6 Tesla. (b) The momentum scattering rate for motion in specific directions at  $B=4$  Tesla. The scattering rate represents the amount of scattering for motion in both (positive and negative) directions in the specified direction.)

This is illustrated in Fig. 5.6, with results for a  $B$ -field along the [100] direction. Upon increasing the external field to a few Tesla, the typical dephasing times increase since the relative strength of the SO fields is getting smaller. For ideal alignment of the field with a wire (*i.e.* a wire in the [100] direction) there is a sharp peak in the  $T_2^*$  which we attribute to the formation of stable cyclotron orbits that are not disturbed by wall collisions. The electrons can then move freely along the wire with very small probability to scatter on the edge, and such trajectories preserve the averaged spin orientation. This interpretation is supported by the study of scattering rates that is presented in Fig. 5.6(b).

As soon as the wire orientation deviates a small amount from this ideal alignment, the cyclotron orbits are no longer closed, but turn into skipping orbits on the walls. This comes along with frequent random scattering and differences in

the precession dynamics within the electrons ensemble (observed as much lower  $T_2^*$  values). In this regime the external magnetic field is dominating the motion of electron trajectories, and this in turn governs the spin dephasing.

## 5.5 Conclusions

We presented a numerical tool for studying the temporal evolution of spin ensembles in micronscale structures of bulk GaAs material. Our modeling tool is based on a semiclassical picture for the electron spin in the material. Simulations with this tool show spin dephasing anisotropy (SDA) for electron ensembles in quasi-ballistic wires. These calculations serve as a theoretical background for effects which have been observed experimentally. We quantify the spin dephasing times and SDA for material parameters as in the experiment, and find reasonable agreement.

By comparing results for specular and non-specular momentum scattering on the edges of the wires we find that the spin dephasing anisotropy in 3D wires with specular scattering arises due to a different mechanism than confinement-enhanced motional narrowing. We attribute the observed SDA to a new mechanism that can be pictured as ballistic spin resonances that occur due to the interplay between repetitive scattering trajectories and the symmetries in the spin-orbit fields. Notably, this already occurs when the spin precession length is smaller than the transverse wire dimensions. Our SDA findings agree with the experimental results (for which can indeed expect specular scattering), while the motional narrowing picture does not.

We also studied the effect of an external magnetic field on a spin polarized electron ensembles in a wire. For values of the magnetic field where the cyclotron radius is smaller than the wire width the field dominates that character of the electron trajectories and the amount of wall scattering. In turn, this is decisive for the spin dephasing time. These results are very sensitive to the alignment of the wire with respect to the magnetic field and the crystallographic axis.

We thank S. Artyukhin and A. Rudavskyi for help and valuable discussions and acknowledge the support of the High Performance Computing Center at the University of Groningen.

## References

- [1] M. I. D'yakonov and V. I. Perel', *Sov. Phys. Solid State* **13**, 3023 (1972).

- 
- [2] R. Winkler, *Spin-Orbit Coupling Effects in Two-Dimensional Electron and Hole Systems*, Springer Tracts in Modern Physics Vol. 191 (Springer, Berlin, 2003).
  - [3] J. D. Koralek, C. P. Weber, J. Orenstein, B. A. Bernevig, Shou-Cheng Zhang, S. Mack, and D. D. Awschalom, *Nature (London)* **458**, 610 (2009).
  - [4] N. S. Averkiev, L. E. Golub, and M. Willander, *J. Phys.: Condens. Matter* **14** R271 (2002).
  - [5] B. Andrei Bernevig, J. Orenstein, and Shou-Cheng Zhang, *Phys. Rev. Lett.* **97**, 236601 (2006).
  - [6] M. Duckheim and D. Loss, *Phys. Rev. B* **75**, 201305(R) (2007).
  - [7] M. Duckheim, D. L. Maslov, and D. Loss, *Phys. Rev. B* **80**, 235327 (2009).
  - [8] M. Duckheim, D. Loss, I. Adagideli, and P. Jacquod, *Phys. Rev. B* **81**, 085303 (2010).
  - [9] A. W. Holleitner, V. Sih, R. C. Myers, A. C. Gossard, and D. D. Awschalom, *Phys. Rev. Lett.* **97**, 036805 (2006); A. W. Holleitner, V. Sih, R. C. Myers, A. C. Gossard, and D. D. Awschalom, *New J. Phys.* **9**, 342 (2006).
  - [10] S. Z. Denega, T. Last, J. Liu, A. Slachter, P. J. Rizo, P. H. M. van Loosdrecht, B. J. van Wees, D. Reuter, A. D. Wieck, C. H. van der Wal, *Phys. Rev. B* **81**, 153302 (2010).
  - [11] G. Dresselhaus, *Phys. Rev.* **100**, 580586 (1955).
  - [12] R. H. Silsbee, *J. Phys. Condens. Matter* **16**, R179 (2004).
  - [13] S. M. Frolov, S. Lüscher, W. Yu, Y. Ren, J. A. Folk, and W. Wegscheider, *Nature (London)* **458**, 868 (2009).
  - [14] J. B. Miller, D. M. Zumbuhl, C. M. Marcus, Y. B. Lyanda-Geller, D. Goldhaber-Gordon, K. Campman, and A. C. Gossard, *Phys. Rev. Lett.* **90**, 076807 (2003).
  - [15] E. J. Koop, B. J. van Wees, C. H. van der Wal, arXiv:0804.2968 (2008).
  - [16] J. Liu, T. Last, E. J. Koop, S. Denega, B. J. van Wees, C. H. van der Wal, *J. Supercond. Nov. Magn.* **23**, 11 (2010).
  - [17] S. Lüscher, S. M. Frolov, J. A. Folk, *Phys. Rev. B* **82**, 115304 (2010).
  - [18] W. W. Yu, S. M. Frolov, S. Lüscher, J. A. Folk and W. Wegscheider, arXiv:1009.5702 (2010).

- [19] J. Fabian, A. Matos-Abiague, C. Ertler, P. Stano, and I. Zutic, *Semiconductor Spintronics*, Acta Phys. Slov. **57**, 565 (2007).

## Chapter 6

# Ultrafast mapping of optical polarization states onto spin coherence of localized electrons in a semiconductor

### Abstract

We experimentally demonstrate an ultrafast method for preparing spin states of donor-bound electrons in GaAs with single laser pulses. Each polarization state of a preparation pulse has a direct mapping onto a spin state, with bijective correspondence between the Poincaré-sphere (for photon polarization) and Bloch-sphere (for spin) state representations. The preparation is governed by a stimulated Raman process and occurs orders of magnitude faster than the spontaneous emission and spin dephasing. Similar dynamics governs our ultrafast optical Kerr detection of the spin coherence, thus getting access to spin state tomography. Experiments with double preparation pulses show an additive character for the preparation method. Utilization of these phenomena is of value for quantum information schemes.

---

This chapter is based on Ref. 3 on p. 103.

## 6.1 Introduction

The ability to rapidly prepare and detect arbitrary spin states is of key interest in the fields of quantum information [1] and spintronics [2]. This is currently explored with the electron spin in many different material systems such as atomic gases [3, 4, 5, 6], quantum dots [7, 8, 9, 10, 11, 12] and defect centers in diamond [13, 15, 14]. Donor-bound electrons in semiconductors ( $D^0$  systems) are another interesting system [16, 17, 18, 19, 20, 21], as they provide optically active centers with atom-like properties in solid state:  $D^0$  systems combine a high level of homogeneity for ensembles (as for atomic vapors) with strong optical transitions and the ability to nano-fabricate and integrate very compact optoelectronic devices with semiconductor processing tools.

We report here a method for preparation and detection of arbitrary  $D^0$  spin states with picosecond laser pulses, using GaAs with Si donors at very low concentration. The polarization state of the pump pulse fully determines which spin state is prepared. Such preparation [22] and tomographic detection [23] was recently also reported for a GaAs quantum well system. However, there spin coherence was prepared for photo-electrons from single-photon transitions, such that the coherence was limited by electron-hole recombination ( $\sim 300$  ps). We developed an analogous method, but with two-photon Raman transitions between the two  $D^0$  spin states, such that spin coherence is prepared for donor-bound electrons and thus not limited by electron-hole recombination.

Preparing pure spin-up and -down states by optical pumping was already demonstrated with the GaAs  $D^0$  system [17, 19]. Preparation of arbitrary spin states was demonstrated using Coherent Population Trapping (CPT) [16, 21], but the spectroscopic character of this method makes it difficult to control the phase of the quantum state. Moreover, in both cases the preparation takes a few cycles of the spontaneous emission time ( $\sim 1$  ns). Work with detuned picosecond laser pulses demonstrated all-optical spin manipulation [19] and spin echo [20] with a spin coherence time  $T_2$  in excess of  $20 \mu\text{s}$ . Our work here adds picosecond preparation and detection to the available operations for  $D^0$  spins, thus expanding a set with a ratio between coherence time and operation time in excess of  $10^7$ . Completing such a set of tools is essential for investigating quantum error correction schemes [24].

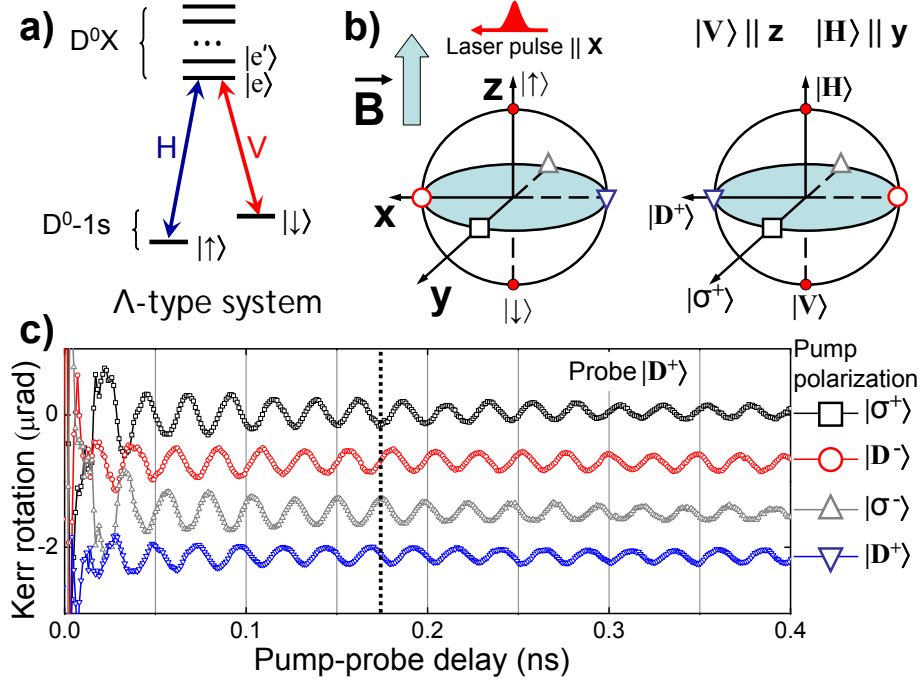


**Figure 6.1:** (a) Energy levels and optical transitions of the  $D^0$ - $D^0X$  system. (b) Bloch sphere representation of electron spin states (left) and Poincaré-sphere representation of the photon polarization states (right). The field  $\vec{B}$  causes spin precession about the  $z$ -axis. Laser pulses propagate along the  $x$ -axis and drive spin state preparation, and subsequent detection with a delayed pulse. (c) Time-resolved Kerr rotation signals displaying the time evolution of four different initial states in the Bloch-sphere equatorial plane (offset for clarity). The phase of the oscillations in each trace corresponds to the precession phase of the spin state. The initial spin state is determined by the polarization of the preparation pulse, as labeled with matching symbols in (b) and (c). Comparing the oscillations at –for example– the dashed line (at 175 ps delay) shows four different phase values.

## 6.2 Experimental realization of bijective mapping

We explored the preparation of spin states with laser pulses that are resonant with transitions of the  $D^0$  system to states with an additional electron-hole pair (donor-bound trion system  $D^0X$ ). However, with fast pulses it is impossible to address transitions to the lowest  $D^0X$  level  $|e\rangle$  only, since within the spectral width of a short laser pulse it has many energy levels [Fig. 6.1(a)]. The selection rules for these transitions are –despite extensive studies [25, 16, 21]– not yet fully

understood. The coupling to these higher levels can play a role, as well as weak coupling to other solid-state excitations [19]. This situation is therefore difficult to assess theoretically. Experimentally, we find nevertheless remarkably simple and robust behavior for the preparation and detection. The results systematically show the behavior of an effective three-level system, and the associated quantum optical effect of CPT that was observed in  $D^0$  studies with continuous wave (CW) lasers [16, 21]. While the higher  $D^0X$  levels can be modeled with one effective  $|e'\rangle$  level [18], we have at this stage no complete understanding of the fact that these levels have such little influence on the spin preparation and detection step.

We therefore describe the  $D^0$  system as a typical three-level  $\Lambda$ -scheme [19] for which a spin-up and -down state ( $|\uparrow\rangle$  and  $|\downarrow\rangle$ ) both have an optical transition to the same excited state  $|e\rangle$  [Fig. 6.1(a)]. The degeneracy of  $|\uparrow\rangle$  and  $|\downarrow\rangle$  is lifted by an applied magnetic field  $|\vec{B}| = 7$  T along the  $z$ -axis. The state  $|e\rangle$  is then the lowest energy level of the  $D^0X$  complex, with two electrons in a singlet state and a hole with  $m_h = -\frac{1}{2}$  [20]. We use optical propagation orthogonal to  $\vec{B}$  (Voigt geometry). High-resolution spectroscopy for this case [21] showed selection rules where the  $|\uparrow\rangle$ - $|e\rangle$  transition only couples to H-polarized light (linear polarization orthogonal to  $\vec{B}$ ), and the  $|\downarrow\rangle$ - $|e\rangle$  only to V-polarized light (parallel with  $\vec{B}$ ). The polarization of light will further be denoted as quantum states  $|H\rangle$ ,  $|V\rangle$ , and we also use the notation  $|D^\pm\rangle = \frac{1}{\sqrt{2}}(|H\rangle \pm |V\rangle)$  and  $|\sigma^\pm\rangle = \frac{1}{\sqrt{2}}(|H\rangle \pm i|V\rangle)$ .

The mentioned CPT physics results from destructive quantum interference in the system's dynamics when driving the H- and V-transition at the same time. The system then gets trapped in a coherent superposition of the  $|\uparrow\rangle$  and  $|\downarrow\rangle$  states only [26, 16, 21]. This state is proportional to  $\Omega_V |\uparrow\rangle - \Omega_H |\downarrow\rangle$ , where the complex optical Rabi frequencies  $\Omega_H$  and  $\Omega_V$  account for both the amplitude and the phase of two selectively applied driving fields. In the conventional CPT case (driving with a pair of weak CW lasers), the transition from an incoherent initial state into the CPT state takes a few times the spontaneous emission time [26]. For our present work, however, we consider the case where we drive both transitions with a single picosecond laser pulse which has an H- and V-component, and with a spectral width ( $\Delta E = 1.8$  meV) that is larger than the  $D^0$  Zeeman splitting ( $E_Z = 0.16$  meV). The polarization state of the pulse  $\alpha|H\rangle + e^{i\varphi}\beta|V\rangle$  thus determines how it interacts with the three-level system, and we find behavior that is consistent with the mapping

$$\alpha|H\rangle + e^{i\varphi}\beta|V\rangle \quad \rightarrow \quad \beta |\uparrow\rangle - e^{-i\varphi}\alpha |\downarrow\rangle, \quad (6.1)$$

where  $\alpha$  and  $\beta$  are positive real-valued probability amplitudes, and  $\varphi$  is a phase

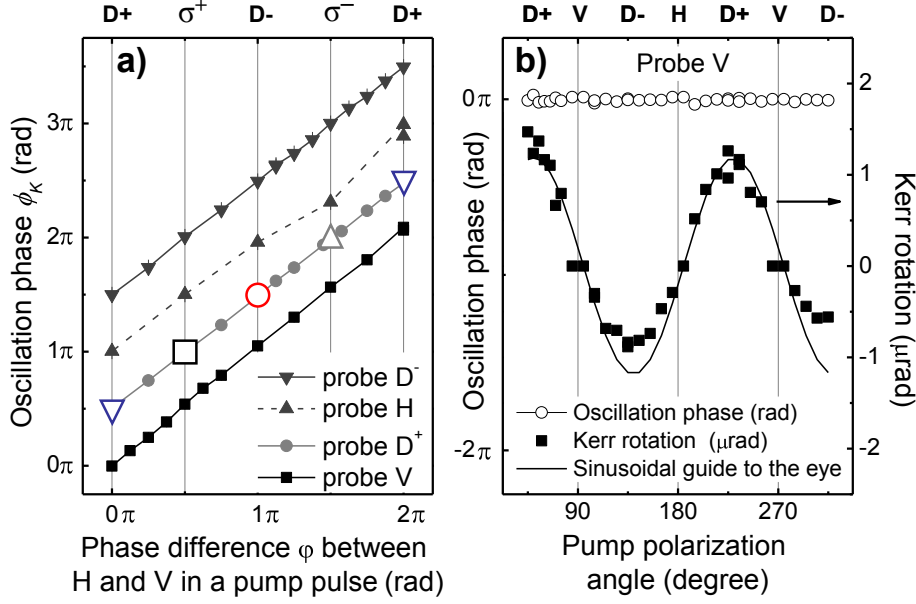


**Figure 6.2:** (a) The phase  $\phi_K$  of oscillations in Kerr signals for different probe polarizations, as a function of the phase difference  $\varphi$  between the  $H$ - and  $V$ -component in the preparation pulse (see also the polarization labels on the top axis). Empty symbols correspond to the data extracted from Fig. 6.1(c). (b) Amplitude (right axis) and phase (left axis) for the oscillating Kerr signal as a function of polarization angle (see again the top axis for polarization labels) for a linearly polarized preparation pulse (with –unlike (a)– using in the fits a negative amplitude rather than a phase change of  $\pi$ ).

for the quantum superpositions. The swap of  $\alpha$  and  $\beta$  and sign change for the phase directly reflect the underlying CPT physics. We thus operate a unique mapping from polarization state onto spin state with direct correspondence between the Poincaré-sphere (for polarization) and Bloch-sphere (for spin) state representations [Fig. 6.1(b)].

Typical results are presented in Fig. 6.1(c). We used a stroboscopic pump-probe method with Kerr detection (further discussed below) for time-resolved preparation and detection of  $D^0$  spin coherence. Figure 6.1(c) shows oscillating Kerr signals that directly reflect the precession of prepared spin states about the field  $\vec{B}$ . Notably, the phase of the precession is determined by the polarization of the pump pulse, and can be traced back to an initial state that shows a unique mapping between polarization and spin states.

We used an epitaxial GaAs film grown along [001] of  $10 \mu\text{m}$  thickness with Si doping at  $n_{\text{Si}} \approx 3 \times 10^{13} \text{ cm}^{-3}$  (same material as our CPT results [21] but

with the epitaxial lift-off process omitted). Measurements were performed at 4.2 K in an optical cryostat with superconducting magnet, and with pump and probe laser beams at normal incidence to the sample plane. The pump and probe beams were focused into a spot of 120  $\mu\text{m}$  diameter. The laser photon energy was  $E = 1.5167$  eV (unless stated otherwise) and tuned to resonance with transitions from  $|\uparrow\rangle$  and  $|\downarrow\rangle$  to  $|e\rangle$ . This photon energy is sufficiently low for avoiding the generation of a significant amount of free excitons. The spectral width of the laser pulses was reduced to 1.8 meV by filtering with a tunable liquid-crystal Fabry Perot (LCFP). All measurements were performed in the regime  $T_2^* < T_{rep} < T_1$ , where  $T_2^* \approx 2$  ns is the ensemble transverse spin dephasing time,  $T_{rep} \approx 12$  ns is the laser repetition time, and  $T_1 \approx 1$  ms is the  $D^0$  longitudinal spin relaxation time (value taken from Ref. [17]).

For determining the  $D^0$  spin state we measure the Kerr rotation of a reflected probe pulse, while scanning a controllable delay  $t$  between preparation and probe pulses. The polarization rotation is measured with a polarization bridge. Widespread application of this technique showed that it measures spin orientation along the probe beam when applied to a continuum of transitions in a semiconductor [27]. However, we apply it to the discrete set of transitions of the  $D^0$ - $D^0X$  system, and find that we can measure the  $D^0$  spin state along any desired basis by choosing the probe polarization. This gives access to spin state tomography, analogous to the method that was developed for GaAs quantum wells [23].

Figure 6.2(a) presents results from a systematic study of phase values  $\phi_K$  that appear in the oscillations of the measured Kerr signals, obtained with four different linear polarizations of the probe. The phase values  $\phi_K$  were obtained by fitting the signals to a function with factor  $\cos(\omega_L t + \phi_K)$  to represent the oscillations at the Larmor frequency  $\omega_L$ , and with a mono-exponentially decaying envelope. The  $\phi_K$  values are studied as a function of a continuous range of phase values  $\varphi$  applied in preparation pulses with polarization states in the form  $\frac{1}{\sqrt{2}}(|H\rangle + e^{i\varphi}|V\rangle)$  (these are all states on the Poincaré-sphere equator, and the plot includes the results of Fig. 6.1(b,c) with matching symbols, for states that were prepared with phase values  $\varphi = 0, \pi/2, \pi$  and  $3\pi/2$ ). The four straight lines evidence that our method can prepare any state on the equator in a manner that is consistent with the mapping as in Eq. 6.1. In addition, the phase offset between the four straight lines confirms that the probe polarizations  $|V\rangle, |D^+\rangle, |H\rangle, |D^-\rangle$  measure spin orientation along the  $-x, -y, +x, +y$  direction, respectively. We focussed on measuring the equator states, as these carry a clear signature of

spin precession for which we can analyze the phase after careful calibration of the point of zero pump-probe delay. Our results indicate that spin orientation along the  $z$ -axis can be measured with  $|\sigma^\pm\rangle$  probe polarization, but this was more difficult to measure given the long  $T_1$  time for our system.

For the preparation, we could confirm the mapping of Eq. 6.1 with states below or above the equator, with a continuous range of polarization states  $\alpha|H\rangle + \beta|V\rangle$ , with varying real  $\alpha$  and  $\beta$  and fixed  $\varphi = 0$ . This shows, for example, a sinusoidal modulation of the amplitude of Kerr oscillations at a fixed phase for the signal of spin-orientation along the  $-x$ -axis [Fig. 6.2(b)]. This study thus confirms that our method shows bijective mapping between polarization states and spin states, both for preparation and detection.

Since the excitation occurs at energies which are below the GaAs band gap (and resonant with  $D^0$  transitions), the presented Kerr signals are purely due to  $D^0$  spin coherence (in the part of the signal beyond a delay of  $\sim 25$  ps). This is confirmed by the fact that the signals live longer than the various electron-hole recombination processes that can occur in this system. In addition, we find in all traces a  $g$ -factor of  $|g|=0.423\pm 0.002$ , which is consistent with the  $D^0$  case at 7 T. This provides evidence that both the preparation and detection must be due to a stimulated Raman process that occurs during the pulses.

### 6.3 Robustness of spin preparation

We studied the robust character of our method by varying the intensities and detuning of the laser pulses. The amplitude of Kerr signals (directly representing spin coherence) in Fig. 6.3(a) appears to be proportional to the optical Rabi frequency of the excitation (note that the scale represents actual measured Kerr rotation angle). It remains almost linear until  $10\cdot P_0$  (high- $P$  data not shown). This behavior is consistent with the presence of chirped modulation in the laser pulses [11, 12] (which appears in our setup after spectral filtering of the laser with the LCFP). At the lowest measured pump power the extracted  $T_2^*$  is close to the nuclear field limited value [16, 21]. Upon increasing the excitation power the spin dephasing time shortens. This is probably due to the generation of free excitons [28] (for which the red-detuned wing of the absorption line weakly overlaps with the spectrum of our pump pulse). Subsequently, the presence of free excitons leads to a capture-release and dynamics [29] on  $D^0$  sites and this disturbs the  $D^0$  spin coherence. Otherwise, our preparation and detection scheme are robust against a significant change in laser power (in particular, the phase of

the observed spin precession is not strongly affected). Increasing the pump laser power reduces the ratio between the  $T_2^*$  coherence time and the operation time, but it does not affect the phase information of the spin state.

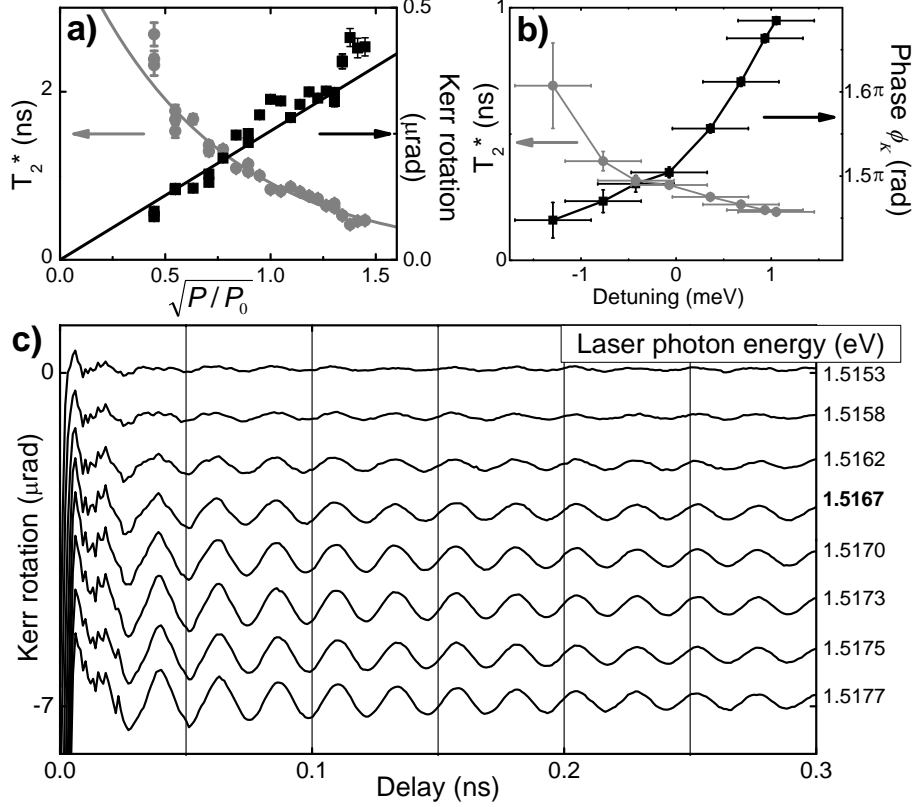


**Figure 6.3:** (a) Dependence of the spin dephasing time  $T_2^*$  (left axis, solid line is guide to the eye) and Kerr oscillation amplitude (right axis, solid line is linear fit) on preparation power  $P$ , where  $P_0=1$  mW. (b) Spin dephasing time  $T_2^*$  and the Kerr oscillation phase  $\phi_K$  as a function of laser detuning. (c) Kerr signals for different excitation photon energies (tuned simultaneously for preparation and probe pulses). Data is offset for clarity. Polarizations of pump and probe beams are  $|D^-\rangle$  and  $|D^+\rangle$  respectively.

By increasing the photon energy for the laser pulses from exact resonance we test how robust our spin preparation and detection method is with respect to an increased role for the higher levels  $|e'\rangle$  of the  $D^0X$  complex [Fig. 6.1(a)]. Increasing the photon energy results in stronger interaction with these levels, and Fig. 6.3(b) shows that a 1 meV blue detuning gives a  $0.18\pi$  phase shift to the observed spin precession. At the same time, the efficiency of state preparation goes up (higher signal amplitude) while the spin dephasing time goes down

[Fig. 6.3(b,c)]. This can be explained as follows: More levels involved in the Raman process gives a higher efficiency for the preparation process, but different polarization selection rules for the higher levels  $|e'\rangle$  [21] also cause a phase shift for the state that is prepared. At the same time, the number of free excitons that are created by the pump pulse also increases, and this probably is the main cause for the reduction of the spin dephasing time. The method therefore functions best and is most robust for pulses that are resonant or slightly red detuned from exact resonance with transitions to the lowest  $D^0X$  level  $|e\rangle$ .

## 6.4 Repeated preparation of a spin state

Further insight into the robust character of our preparation method can be obtained from applying a preparation pulse to an ensemble which already contains spin coherence [10]. To this end, we performed experiments with two identical preparation pulses in sequence, where the repeated pulse (RP) is reaching the system after a controllable delay with respect to the initial pulse. Figure 6.4 shows the evolution of the spin state with and without applying the RP, and for two RP delay values that differ by  $\Delta t$ . The RP can either enhance [Fig. 6.4 middle trace] or suppress [bottom trace] the original spin signal [top trace], and this depends on the delay between the initial pulse and RP. In particular, the enhancement (suppression) occurs when the RP prepares a state that is in phase (in counter phase) with the ensemble's ongoing free precession, as labeled by  $\Delta\varphi = 0$  ( $\Delta\varphi = \pi$ ).

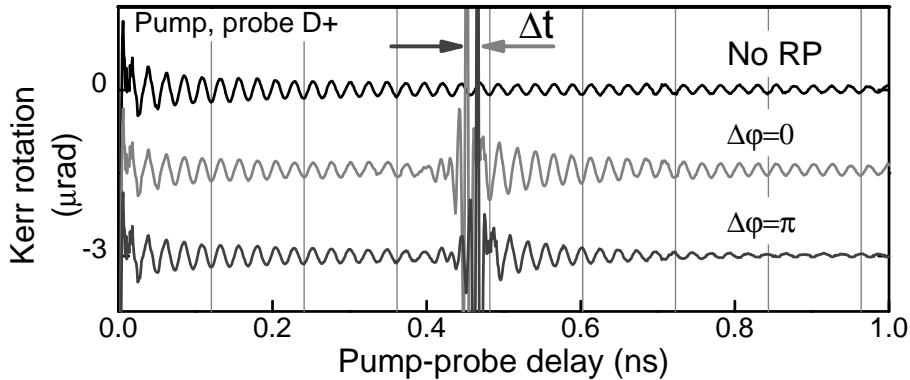


**Figure 6.4:** Kerr oscillation traces for various delays between initial and repeated preparation (RP) pulses (data offset for clarity).

Notably, the experimental data shows that the RP at our power levels does

neither result in pure spin manipulation [19, 10], nor in pure preparation without memory effects. Instead, the RP results in a state that is the vector sum of the Bloch-sphere state vectors for the freely precessing state and the RP-induced state. Since the RP comes when the original state is already partially dephased, the resulting state does not show full cancelation in the case of an RP that adds a state in counter phase. The additive character of precessing and RP-pulse induced states points to the option to use  $D^0$  ensembles for storing the algebraic sum of two or more quantum states.

## 6.5 Conclusions

In conclusion, we presented a picosecond spin preparation and detection method for  $D^0$  electron spins, which gives a ratio of  $10^7$  between the  $T_2$  coherence time and operation time. Our preparation and detection method show a simple and robust bijective mapping between photon polarization states and  $D^0$  spin states. While we have a strong indication that the mentioned CPT physics plays a role for the preparation step, we have at this stage less insight in the mechanism that underlies the detection step and can not provide a theoretical framework. It is also not yet clear to what degree our preparation method induces an incoherent population into the level  $|e\rangle$  and higher levels. This would mean that we prepare –with respect to the full three-level system– a partially coherent state in the donor-bound electron systems. However, such states can still serve as a basis for quantum information operations [30]. An exchange of quantum optical signals between spin ensembles in different micronscale volumes could provide a path to creating entanglement between the state of different spin ensembles, but it remains to be explored how this can be worked out for ensembles that are partially incoherent. We also obtained indications that very strong near-resonance optical driving with fast pulses shortens the spin dephasing time, probably due to the off-resonant generation of free excitons. This is difficult to circumvent and will remain a concern for applications that aim to use higher optical power levels.

We thank the Dutch NWO and NanoNed, and the German programs DFG-SFB 491, DFG-SPP 1285 and BMBF nanoQUIT for financial support.

## References

- [1] T. D. Ladd, F. Jelezko, R. Laflamme, Y. Nakamura, C. Monroe, and J. L. O’Brien, *Nature (London)* **464**, 45 (2010).

- 
- [2] D. Awschalom and N. Samarth, *Physics* **2**, 50 (2009).
  - [3] L. M. Duan, M. D. Lukin, J. I. Cirac, and P. Zoller, *Nature* **414**, 413 (2001).
  - [4] C. W. Chou, H. de Riedmatten, D. Felinto, S. V. Polyakov, S. J. van Enk, and H. J. Kimble, *Nature* **438**, 828 (2005).
  - [5] T. Chanelière, D. N. Matsukevich, S. D. Jenkins, S.-Y. Lan, T. A. B. Kennedy, and A. Kuzmich, *Nature* **438**, 833 (2005).
  - [6] M. Müller, I. Lesanovsky, H. Weimer, H. P. Büchler, and P. Zoller, *Phys. Rev. Lett.* **102**, 170502 (2009).
  - [7] F. H. L. Koppens, C. Buizert, K. J. Tielrooij, I. T. Vink, K. C. Nowack, T. Meunier, L. P. Kouwenhoven, and L. M. K. Vandersypen, *Nature* **442**, 766 (2006).
  - [8] D. Press, T. D. Ladd, B. Zhang, and Y. Yamamoto, *Nature (London)* **456**, 218 (2008).
  - [9] J. Berezovsky, M. Mikkelsen, N. Stoltz, L. Coldren, and D. Awschalom, *Science* **320**, 349 (2008).
  - [10] A. Greilich, S. Economou, S. Spatzek, D. Yakovlev, D. Reuter, A. Wieck, T. Reinecke, and M. Bayer, *Nature Phys.* **5**, 262 (2009).
  - [11] E. R. Schmidgall, P. R. Eastham, and R. T. Phillips, *Phys. Rev. B* **81**, 195306 (2010).
  - [12] Y. Wu, I. M. Piper, M. Ediger, P. Brereton, E. R. Schmidgall, P. R. Eastham, M. Hugues, M. Hopkinson, and R. T. Phillips, *Phys. Rev. Lett.* **106**, 067401 (2011).
  - [13] G. D. Fuchs, V. V. Dobrovitski, D. M. Toyli, F. J. Heremans, C. D. Weis, T. Schenkel, and D. D. Awschalom, *Nature Phys.* **6**, 668 (2010).
  - [14] G. de Lange, Z. H. Wang, D. Ristè, V. V. Dobrovitski, R. Hanson, *Science* **330**, 60 (2010).
  - [15] E. Togan, Y. Chu, A. S. Trifonov, L. Jiang, J. Maze, L. Childress, M. V. G. Dutt, A. S. Sorensen, P. R. Hemmer, A. S. Zibrov and M. D. Lukin, *Nature* **466**, 730 (2010).
  - [16] Kai-Mei C. Fu, C. Santori, C. Stanley, M.C. Holland, and Y. Yamamoto, *Phys. Rev. Lett.* **95**, 187405 (2005).
  - [17] Kai-Mei C. Fu, W. Yeo, S. Clark, C. Santori, C. Stanley, M. C. Holland, and Y. Yamamoto, *Phys. Rev. B* **74**, 121304(R) (2006).

- [18] T. Wang, R. Rajapakse, and S. Yelin, *Opt. Commun.* **272**, 154 (2007).
- [19] Kai-Mei C. Fu, S. M. Clark, C. Santori, C. R. Stanley, M. C. Holland, and Y. Yamamoto, *Nature Phys.* **4**, 780 (2008).
- [20] S. M. Clark, Kai-Mei C. Fu, Q. Zhang, T. D. Ladd, C. Stanley, and Y. Yamamoto, *Phys. Rev. Lett.* **102**, 247601 (2009).
- [21] M. Sladkov, A. U. Chaubal, M. P. Bakker, A. R. Onur, D. Reuter, A. D. Wieck, and C. H. van der Wal, *Phys. Rev. B* **82**, 121308(R) (2010).
- [22] H. Kosaka, H. Shigyou, Y. Mitsumori, Y. Rikitake, H. Imamura, T. Kutsuwa, K. Arai, and K. Edamatsu, *Phys. Rev. Lett.* **100**, 096602 (2008).
- [23] H. Kosaka, T. Inagaki, Y. Rikitake, H. Imamura, Y. Mitsumori, and K. Edamatsu, *Nature (London)* **457**, 702 (2009).
- [24] M. A. Nielsen and I. L. Chuang, *Quantum Computation and Quantum Information* (Cambridge University Press, Cambridge, 2000).
- [25] V. A. Karasyuk, D. G. S. Beckett, M. K. Nissen, A. Villemaire, T. W. Steiner, and M. L. W. Thewalt, *Phys. Rev. B* **49**, 16381 (1994).
- [26] M. Fleischhauer and A. Imamoglu, *Rev. Mod. Phys.* **77**, 633 (2005).
- [27] J. M. Kikkawa, I. P. Smorchkova, N. Samarth and D. D. Awschalom, *Science* **277**, 1284 (1997).
- [28] For pump power of  $P=1$  mW the density of free excitons generated in the sample is approximately equal to the density of  $D_0$  electrons.
- [29] R. I. Dzhioev, K. V. Kavokin, V. L. Korenev, M. V. Lazarev, B. Y. Meltser, M. N. Stepanova, B. P. Zakharchenya, D. Gammon, and D. S. Katzer, *Phys. Rev. B* **66**, 245204 (2002).
- [30] N. A. Gershenfeld, and I. L. Chuang, *Science* **275**, 350 1997.

## Chapter 7

# Optical time-resolved study of the Landé $g$ factor in $n$ -doped GaAs materials

### Abstract

We present time- and energy-resolved measurements of the electron  $g$  factor in GaAs materials with Si donors at concentrations at and below the metal-insulator transition ( $n \approx 10^{13}$  to  $2 \times 10^{16}$  cm $^{-3}$ ). Results were obtained with optical Kerr readout. We studied the dependence on doping concentration, density of photo-carriers, photon energies and magnetic field. While the widely reported  $g$  factor values for these conditions predict  $g \geq -0.44$ , we systematically find values in the range  $-0.49$  to  $-0.44$  for delocalized electrons at low energies in samples where donor sites form a band. With a wavelet analysis a drift of  $g$  factor values during transient spin precession signals is revealed. The spin dynamics in this regime provides a test for fundamental understanding of semiconductors, and complete characterization is a prerequisite for optical studies of GaAs-based spintronic devices.

## 7.1 Introduction

The Landé  $g$  factor for an electronic state in a semiconductor is highly sensitive to the associated band structure. Detailed studies of  $g$  factor values therefore provide an interesting test for our fundamental understanding and theoretical modeling of these materials [1, 2, 3, 4, 5]. Semiconductor materials are also central in research that aims to develop spintronic functionalities. Here, knowing  $g$  factor values is essential, and it is of interest to understand how material parameters influence the  $g$  factor values. A distribution of  $g$  factor values within a precessing electron spin ensemble can dominate the inhomogeneous loss of spin coherence, and it is interesting to understand how external control on a device can manipulate the  $g$  factor [6].

For direct band-gap semiconductors, optical time-resolved Kerr-rotation (TRKR, as used in this work) and Faraday-rotation measurements have been established as standard techniques for the characterization of electron spin dynamics [7]. By tuning the experimental parameters such as photon energy, external magnetic field, and intensity of the optical pump beam one can study the response in different materials, including complex layered structures [8, 9, 10, 11, 12, 13]. This points to another situation that requires reliable knowledge about  $g$  factors: When the TRKR technique is applied to studies of spin dynamics in GaAs/AlGaAs and GaAs/InGaAs heterostructures, TRKR signals can be a superposition of signal contributions from different layers, which can be unraveled using differences in  $g$  factor [14, 11, 12]. Such studies also require knowledge about the instantaneous  $g$  factor value during intraband kinetic energy relaxation of photo-electrons.

We report here a time- and energy-resolved study of the electron  $g$  factor in GaAs materials with Si donor concentrations  $n$  at and below the metal-insulator transition (MIT), using samples with  $n \approx 10^{13}$  to  $2 \times 10^{16}$  cm $^{-3}$ . GaAs materials with this MIT level of doping ( $n \approx 2 \times 10^{16}$  cm $^{-3}$ ) were extensively studied in recent years, since the spin dephasing time as a function of  $n$  peaks here at an exponentially enhanced value [15, 16, 17]. Despite this large body of earlier work, we found in our studies on this material  $g$  factor values that strongly deviate ( $-0.49 < g < -0.44$ ) from what is commonly reported ( $g \gtrsim -0.44$ ) for MIT materials, or even any GaAs material. We carried out TRKR studies at very low optical intensities and with low photon energies and find that  $g$  factors  $g < -0.44$  originate from delocalized electrons in the donor band. We support this conclusion by studying in parallel ultrapure GaAs samples without a donor

band, but which still have a very low level of intentional doping with Si donors. This allowed us to confirm that the  $g$  factors  $g < -0.44$  do not occur for localized donor-bound electrons ( $D^0$  systems, which have  $g \approx -0.42$ ) or for free electrons in the intrinsic conduction band. Thus, our work includes TRKR studies that directly probe the spin dynamics of such  $D^0$  systems. Previously used techniques were not sensitive to  $D^0$  spins [16], or could not distinguish between the contribution from conduction electrons and these donor-bound electrons [18, 5, 19, 20].

The most widely reported value for the GaAs  $g$  factor is  $g = -0.44$ . In addition, it is well described that  $g > -0.44$  can occur due to a diamagnetic shift of the electronic levels, band filling, and quantum confinement in a GaAs layer. This behavior can be approximated as

$$g = g_0 + \gamma E, \tag{7.1}$$

where  $E$  is the electron kinetic energy  $E$  (with respect to the bottom of the conduction band). The accepted values for bulk GaAs are [1, 21, 22]  $g_0 \approx -0.44$  and  $\gamma \approx 6.3 \text{ eV}^{-1}$ . There were, nevertheless, a few reports that mentioned  $g$  factors  $g < -0.44$  without making a systematic study of this deviation [23]. Only recently, Hübner *et al.* [5] reported for the first time a systematic study with  $g$  factors in the range  $-0.49$  to  $-0.44$  for low-energy electrons in a GaAs sample with  $1.2 \times 10^{15} \text{ cm}^{-3}$  Si doping. These authors suspected these values could be only observed with their low-invasive measurement technique (spin-quantum-beat spectroscopy of photoluminescence signals). We extend this study here by applying TRKR as a fully time- and energy-resolved measurement technique, and by including a wider range of doping concentrations. Our work demonstrates that the  $g$  factors in the range  $-0.49$  to  $-0.44$  can also be observed and studied with TRKR. However, while the authors of Ref. [5] conclude that the  $g$  factors  $g < -0.44$  occur for low-energy electrons in the intrinsic conduction band (rather than delocalized electrons at donor levels), our work points to the opposite conclusion.

We strengthen our analysis by applying a wavelet transform for directly analyzing the role of drifting  $g$  factor values during transient TRKR signals. This allows for getting fully time-resolved measurements of the  $g$  factor for optically induced spin coherence. The results are consistent with the picture that  $g$  factors get closer to zero with increasing kinetic energy for electron populations in bands.

## 7.2 Results

For our experiments we used three GaAs samples with Si doping at different concentrations: sample A and B have donor concentrations  $3 \times 10^{13} \text{ cm}^{-3}$  and  $1 \times 10^{14} \text{ cm}^{-3}$ , respectively (the same materials as in Refs. [24, 25], without epitaxial lift-off). At these low concentrations the donor electrons are localized around the Si sites and neighboring electrons do not interact. Sample C is the MIT sample with  $n \approx 2 \times 10^{16} \text{ cm}^{-3}$  (the same wafer material as in Ref. [26]), in which the donor states form a band. All experiments were performed at a temperature of 4.2 K in an optical cryostat with a superconducting magnet for supplying fields up to 7 T. The applied fields at the sample location were known with a precision better than 1 part in  $10^3$ . For the TRKR measurements we used the Voigt geometry (light propagation perpendicular to the sample plane, while the external magnetic field is in plane of the sample).

A tunable Ti:sapphire laser with  $\sim 150$  fs pulses at 80 MHz repetition rate provided the pump and probe beams for the TRKR technique. The beams were focused into fully overlapping spots on the sample with a diameter of  $120 \mu\text{m}$ . The spectrum of pulses was narrowed down to  $\Delta\lambda = 1.2 \text{ nm}$  by tunable Fabry-Pérot filters. This allowed us to have better energy selectivity while keeping the time resolution in the experiment below 1 ps. Both pump and probe were filtered separately, which gave the possibility to perform single- (pump and probe beam at the same wavelength) and two-color (pump and probe beam at different wavelengths) TRKR experiments with a single laser source. The polarization of the pump pulses was modulated between  $\sigma^+$  and  $\sigma^-$  with a photoelastic modulator at 50 kHz. This ensures that dynamical nuclear polarization effects are negligible in our experiments. While varying the time delay  $t$  between pump and probe pulses the rotation of the reflected probe pulse was recorded. A typical TRKR trace is presented in Fig. 7.1(a).

Figure 7.1(b) presents photoluminescence (PL) data from samples A, B and C. The relative peak strength of the donor-bound exciton emission (labeled  $D^0X$ ) gets more pronounced with increasing doping concentration, while the contribution from free excitons ( $X$ ) gets weaker. Mapping out these PL spectra for all magnetic fields is important for proper selection of the pump and probe photon energies in our TRKR experiments (but for sample C we will also use the spectral dependence of the TRKR signals themselves, as discussed later). Unless stated otherwise, our TRKR studies focused on resonant probing of electrons in the energetically lowest states that appeared in the PL spectra. In sample A and B

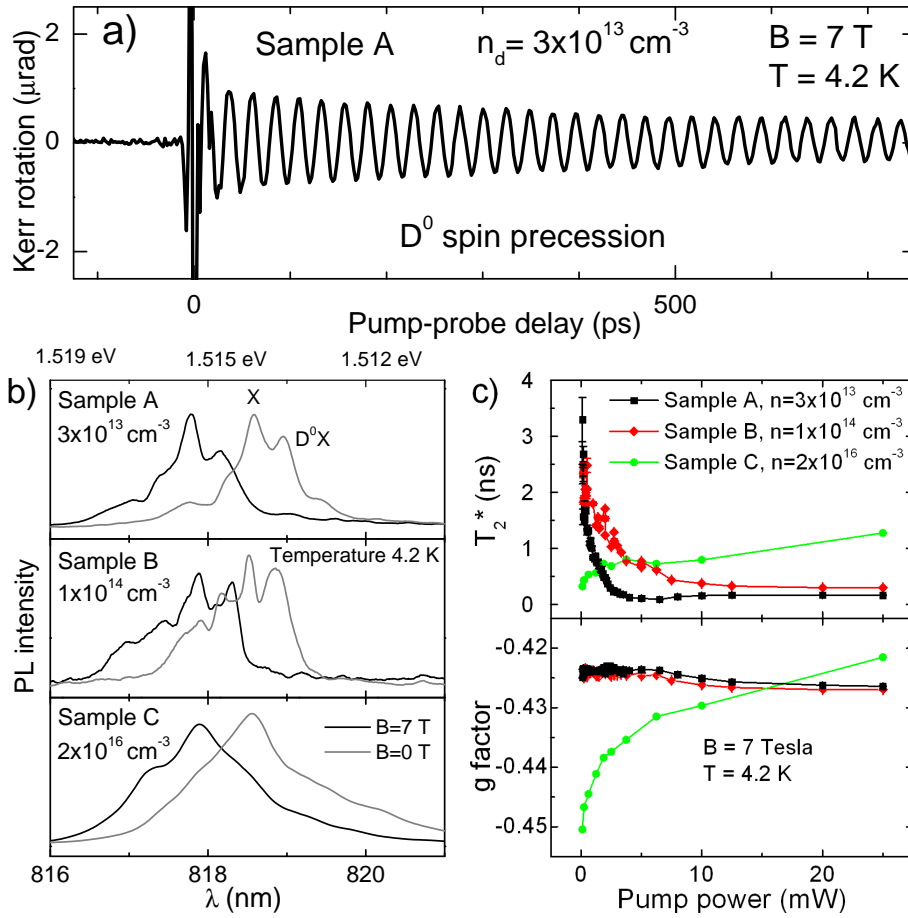


**Figure 7.1:** (a) Typical example of a TRKR signal from  $D^0$  spins in sample A (single-color TRKR with  $\lambda = 818.5 \text{ nm}$  and  $1 \text{ mW}$  pump power). (b) Photoluminescence results from samples A, B and C for  $B = 0 \text{ T}$  (gray) and  $B = 7 \text{ T}$  (black) (the narrowest spectral features correspond to the resolution of the spectrometer). (c) Spin dephasing time ( $T_2^*$ ) and g factors as a function of the pump beam power. The pump and probe wavelengths used in this study were tuned at the donor photoluminescence peak for all three samples.

this concerns the optical transition between the localized  $D^0$  system and the localized donor-bound exciton complex ( $D^0X$  system). However, for sample C the PL peak can not simply be attributed to donor levels. At donor concentrations  $n \approx 10^{15} \text{ cm}^{-3}$  the wave functions of neighboring donor electrons already overlap for a significant portion of the donors. With increasing  $n$  this further develops into a donor band that touches the intrinsic GaAs conduction band. This means that the low-energy PL emission comes from the recombination of delocalized

excitons.

A consequence of the above is that the spin dephasing times  $T_2^*$  and  $g$  factors (as derived from TRKR traces) differ qualitatively for samples with doping below (A and B) and above (C) the donor-band formation point in their dependence on experimental parameters. Figure 7.1(c) shows clearly different behavior for the dependence of  $T_2^*$  and  $g$  on the optical pump power for  $n$ -doping above and below of  $10^{15} \text{ cm}^{-3}$ . Notably, for sample A and B at low pump powers these TRKR results reflect spin precession of  $D^0$  electrons (here preparation and detection occurs via a stimulated Raman process, and the carriers in the  $D^0X$  complex do not contribute to the signal [25]). These show a constant  $g$  factor of  $g = 0.423$  (at  $B = 7 \text{ T}$ ) up to pumping with 7 mW. For stronger pumping sample A and B show very short-lived TRKR signals that also start to reflect spin precession of delocalized electrons (with  $g \approx -0.44$ ), since the excitation of free excitons is no longer negligible. A detailed discussion of this data from sample A and B is presented in Ref. [27].

Sample C, on the other hand, shows a  $g$  factor that sharply increases from  $g = -0.45$  (at  $B = 7 \text{ T}$ ). For such a MIT sample it is difficult to draw a clear line between the donor band and the conduction band. Band filling effects are here responsible for the continuous dependence of the  $g$  factor on pump power. At low pump power the measured  $g$  factor represents the value that corresponds to the electronic levels that are in resonance with the probe photon energy. At higher pump powers, the dependence of  $g$  on pump power is due to the rise of the quasi-Fermi level for photo-electrons, and it thereby reflects the dependence of the  $g$  factor on energy (Eq. (7.1), the energies of the states that dominate the TRKR response increase due to the band filling [22]). The increase of  $T_2^*$  with pump power for sample C is consistent with the theory for spin dephasing in the metal-insulator transition phase [16].

We further explored the sharp decrease in  $g$  to values below  $g = -0.44$ , as observed with sample C while going to very low pump powers [Fig. 7.1(c)]. Our further studies concentrate on behavior in a weaker magnetic field of  $B = 1 \text{ T}$ . Here, the  $g$  factors have less of a diamagnetic shift towards zero, while the precession frequency is still high enough for precise measurements of  $g$ . Since it is for sample C difficult to distinguish between conduction- and donor-band electrons, we first made a detailed TRKR study at low pump powers, with the pump photon energy above the band gap and for different probe photon energies (Fig. 7.2). With the narrow spectral width of the probe beam ( $\Delta\lambda \approx 1.2 \text{ nm}$ ) we thus get TRKR traces for which the response is dominated by electrons from

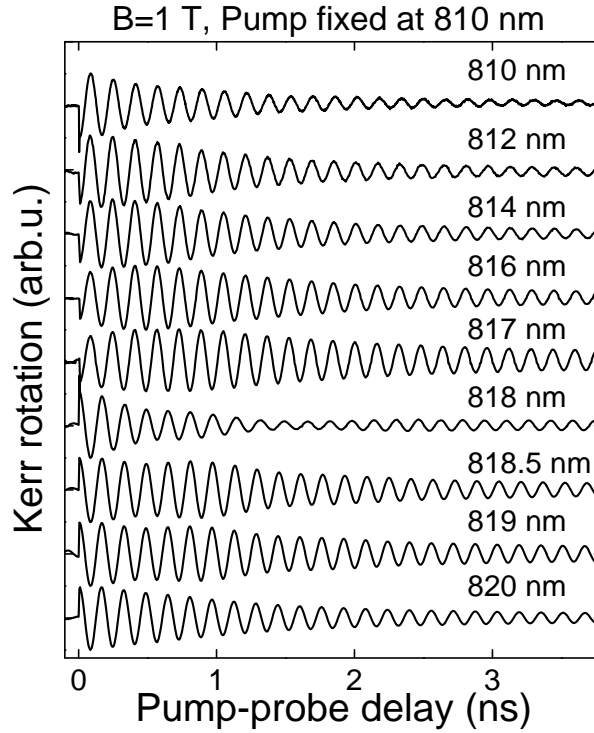


**Figure 7.2:** TRKR signals from Sample C, showing the dependence on probe photon energy (labeled as wavelengths). For all traces pumping occurred with 810 nm light at 1 mW. Probing with light around 818 nm shows TRKR traces with non-monotonous behavior of the envelop function, and this marks the transition from donor-band to conduction-band dominated response.

either the donor-band states or the conduction-band states. For  $B = 1$  T the expected energy for the intrinsic band gap corresponds to  $\sim 818$  nm probe light [28]. We observe indeed a clear transition around 817.5 nm in the series of TRKR traces in Fig. 7.2, as summarized in these points:

- (1) There is a sign flip for the Kerr rotation (consistent with a sign flip for the spin-selective dispersion [29]), associated with a switch from blue-detuned to red-detuned probing of a resonance.
- (2) In particular the trace for 818 nm shows that the TRKR can be sensitive to conduction and donor electrons at the same time, possibly also influenced by relaxation dynamics between these two populations. This signal shows a node in its envelope around 1.8 ns delay, and an overall reduction in amplitude. Similar effects were observed in recent transmission experiments [30, 31].
- (3) Traces with probe photon energies higher than the band gap have a signal

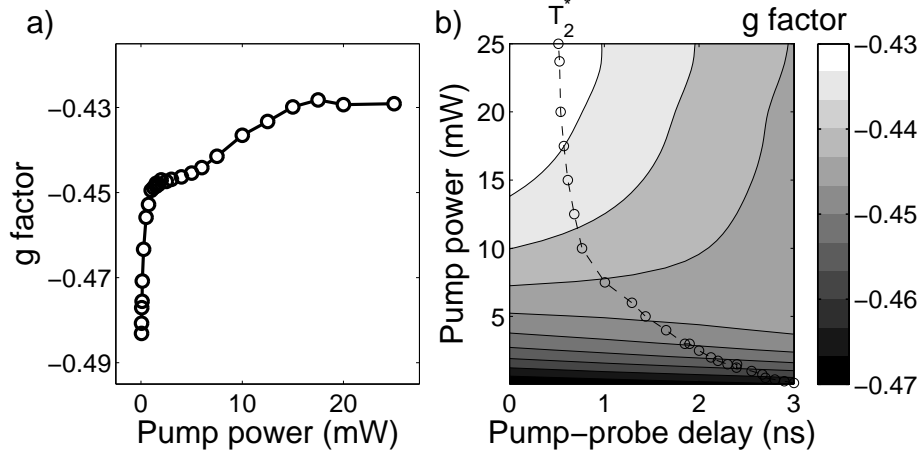


**Figure 7.3:** Values of the  $g$  factor from TRKR signals from sample C. (a) Dependence on pump beam intensity. Here  $g$  factors are determined from a Fourier transform of TRKR data. Pump and probe were at 819 nm and  $B = 1$  T. (b) Dependence of  $g$  factor values (gray scale) on pump beam intensity and pump-probe delay. Here  $g$  factors are derived with a wavelet analysis (see main text). The dashed line indicates the spin dephasing time  $T_2^*$  for the TRKR trace at a particular pump power.

envelope that shows a slow growth during the first few hundred picoseconds due to carrier cooling (intraband relaxation) [30].

(4) Traces with probe photon energies smaller than the band gap show longer  $T_2^*$  values. This is most clearly observed as a residual spin precession signal at negative delays (spin memory effect [15]) that occurs when  $T_2^* \gtrsim T_{rep} = 12.5$  ns (the repetition time for the laser).

We conclude from the study in Fig. 7.2 that for  $B = 1$  T probing with wavelengths  $\lambda_p \geq 819$  nm gives at low pump powers TRKR signals that predominantly represent spin precession of electrons in the donor band. Figure 7.3(a) presents for these conditions and  $\lambda_p = 819$  nm the  $g$  factor values as a function of pump power. Here  $g$  factors decrease to well below  $-0.48$  for the lowest pump powers that we could use. These  $g$  factors were derived from the peak in Fourier transforms of TRKR traces, that show a single narrow peak for the lowest pump powers. However, the data in Fig. 7.2 shows that several of the TRKR traces are clearly sensitive to the interplay between different electron levels and relaxation. This could also manifest itself as drifting  $g$  factors during the TRKR traces. We therefore also carried out a wavelet analysis on the data that underlies Fig. 7.3(a), which can make any relaxation process that influences the observed  $g$  factor directly visible.

The continuous wavelet transform allows to extract instantaneous oscillation frequencies in a signal [32, 33]. Guided by these references, we choose the Morlet wavelet for our analysis to obtain the frequency  $f$  that is most strongly present in the TRKR signal around delay  $t'$ , and then convert to a  $g$  factor with  $g = hf/\mu_B B$ . The wavelet transform of a TRKR signal  $\Theta_k(t)$  is

$$W_\Theta(f, t') = \int_0^\infty \Theta_k(t) \cdot M(t') \cdot dt, \quad (7.2)$$

where  $M(t')$

$$M(t') = \frac{1}{\sqrt{\pi\Delta t^2}} \cdot e^{-2\pi i f t'} \cdot e^{-\frac{(t-t')^2}{\Delta t^2}} \quad (7.3)$$

is the Morlet wavelet. The parameter  $\Delta t$  controls here the trade-off between resolution in time and frequency. We analyzed that  $\Delta t = 250$  ps is a suitable value for our analysis. For this particular wavelet the analysis is equivalent to a sliding-window Fourier transform. Figure 7.3(b) present results of applying this procedure to the data that underlies Fig. 7.3(a). The gray scale represents the extracted  $g$  factor as a function of pump power and delay  $t$ . The spin dephasing time for each pump power is indicated on the plot with a dashed line (estimate based on fitting TRKR oscillations with a mono-exponentially decaying envelope). The plot confirms that intraband relaxation processes influence the instantaneous  $g$  factor values.

For the very lowest pump powers in Fig. 7.3(b), the  $g$  factor is nearly constant at  $g \approx -0.48$ , while the spin dephasing time grows to a value above 3 ns (unlike the data in Fig. 7.1(c) where the high-field causes rapid precessional dephasing due to a small spread in  $g$ -factors). This suggests that the values  $g \lesssim -0.48$  are for electrons in the donor band in the limit of zero pump intensity and low field. For the results with pump powers between  $\sim 1$  mW and  $\sim 6$  mW there is a small increase in the  $g$  factor values during the first 3 ns. For example, the trace for 3 mW shows an increase from  $g \approx -0.455$  to  $g \approx -0.445$ . This behavior is at this stage not fully understood. At the highest pump powers the drift in  $g$  factor values is clearly pointed towards more negative values. Here the density of photoelectrons is much higher than the electron density due to doping, such that the Kerr signal decays over a timescale that is close to the electron-hole recombination time. During this process the quasi-Fermi level goes down, and along with this the  $g$  factor (as for Eq. 7.1). Initially, the donor band is here completely occupied. Therefore, most of the Kerr rotation signal is then coming from conduction band electrons. The values  $g \gtrsim -0.44$  corresponds to the conduction band electrons (which is consistent with most of the earlier observations [1, 26]).

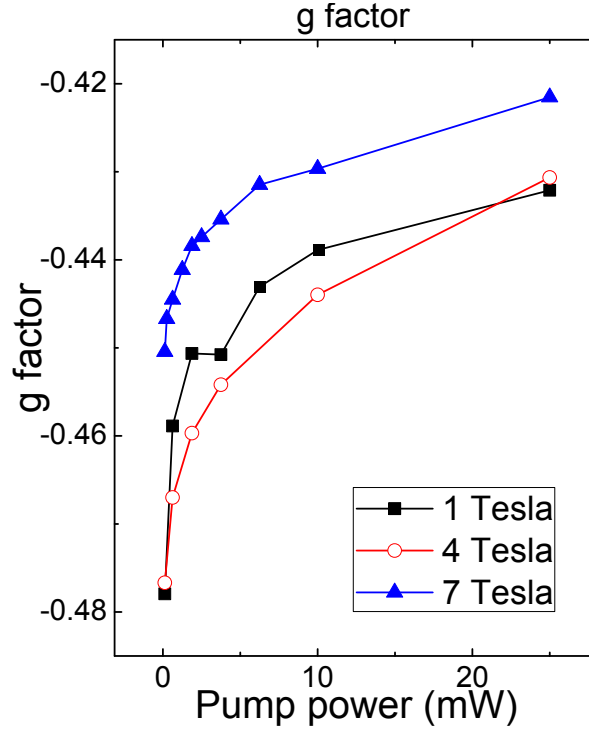


**Figure 7.4:** Values of the  $g$  factor from TRKR signals from sample C, as a function of pump beam intensity at different values for magnetic field. For this data set the probe-wavelength was *not* adjusted for the diamagnetic shift of the band gap energy.

The presented measurements on sample C thus indicate that the values  $-0.49 < g < -0.44$  originate from electrons in the donor band. We used TRKR studies on sample A and B for a test of this hypothesis. In particular, these samples are ultra pure with a low level of  $n$ -doping. This gives an ensemble of  $D^0$  systems that can be addressed with TRKR while not addressing electrons in the intrinsic conduction band at the same time [25]. With these samples we can thus test whether  $g \approx -0.48$  can also be observed on localized  $D^0$  systems, or free excitons in a very pure material. Our studies to this end only showed  $g \approx -0.423$  for the  $D^0$  systems (see Fig. 7.1(c)), while low pump-power studies near resonance with the free exciton transition only showed  $g \approx -0.44$ . Thus, we conclude that  $g$  factor values  $-0.49 < g < -0.44$  only occur for *delocalized* electrons in donor-band states.

Our data does illustrate why the  $g$  factor and  $T_2^*$  values that were reported by the field till now showed such large variation, while  $g$  factors  $g < -0.44$  were almost never reported. Different measurement techniques reported values that

differed more than the reported measurements error [1, 2, 30, 34, 35, 5]. The discrepancy is often hidden in the techniques themselves, meaning that different levels of background doping in samples, photo-excitation power and excitation/detection photon energies result in different results. The measured  $g$  factor value is a function of the experimental parameters, and this restricts the relevance of the reported value.

The data in Fig. 7.3(a) represent a clear example. It shows that the  $g$ -factor value as a function of optical pumping intensity seems to saturate at a value of about  $g = -0.445$  when going to lower pump powers. Only pumping with very low powers (below 1 mW) reveals the sudden trend towards  $g = -0.49$ , and is thus easily overlooked. Another example is the dependence on probe wavelength in Fig. 7.2, which can in a similar manner hamper a study as a function of magnetic field. This is the case for the data set that we present in Fig. 7.4. This plot present  $g$  factors from TRKR traces recorded at different values of the external magnetic field and pump power (single-color TRKR experiments). Here the probe wavelength was *not* adjusted for the small diamagnetic shift of the band gap. This yields a non-monotonous dependence of  $g$  factors on  $B$ , which is hard to interpret without further studies.

## 7.3 Conclusions

In conclusion, we applied the TRKR technique to  $n$ -doped GaAs materials with different doping concentrations. We reproduced the recently reported unconventional  $g$  factor values [5] ( $-0.49 < g < -0.44$ ). Our studies indicate that these  $g$ -factor values originate from delocalized electrons in donor-band states, while localized donor electrons exhibit  $g \approx -0.42$ . Furthermore, our study yields the value  $g \approx -0.44$  for electrons at the bottom of the intrinsic conduction band of GaAs.

We obtained these results by applying the conventional TRKR technique with optimized time- and energy resolution. For our results it was crucial to have the ability to work at weak optical power levels, which we obtained after technical improvements to our detection scheme. We thus showed that the TRKR technique can be applied with about 2 meV energy resolution and at very low optical intensities, such that it is suited for separately studying the spin dynamics of donor electrons and conduction band electrons in samples with very low doping levels. We also extended the standard time-resolved Kerr rotation investigations with a wavelet analysis and this gives access to time-resolved information about

$g$  factor values. The technique can be further extended with the recently reported method for determining the sign of a  $g$  factor from TRKR measurements [36]. TRKR is therefore highly suited for the characterization of the response from substrates or host materials with fully controlled experimental conditions, before analyzing the data from more complex structures [10, 11, 12]. Still, the method should be applied with care since even in a single GaAs layer inter- and intraband relaxation processes can lead to non-trivial TRKR traces (Ref. [30], and Fig. 7.2).

We thank M. Sladkov, B. Wolfs, F. Pei, B. Visser and A. Rudavskiy for help and stimulating discussions, and are grateful for financial support from the Dutch NWO and NanoNed, and the German programs BMBF nanoQUIT, Research school Ruhr-Universität Bochum, DFG-SFB 491 and DFG-SPP 1285.

## References

- [1] C. Weisbuch, and C. Hermann, Phys. Rev. B **15**, 816-822 (1977).
- [2] M. Oestreich, and W. W. Rühle, Phys. Rev. Lett. **74**, 2315 (1995).
- [3] R. Winkler, *Spin-Orbit Coupling Effects in Two-Dimensional Electron and Hole Systems* (Springer, 2003).
- [4] K. Shen, M. Q. Weng, and M. W. Wu, Journal of Applied Physics **104**, 063719 (2008).
- [5] J. Hübner, S. Döhrmann, D. Hägele, and M. Oestreich, Phys. Rev. B **79**, 193307 (2009).
- [6] L. Meier, G. Salis, I. Shorubalko, E. Gini, S. Schon, and K. Ensslin, Nature Phys. **3**, 650 (2007).
- [7] D. Awschalom and N. Samarth, Physics **2** (2009), ISSN 1943-2879.
- [8] I. A. Yugova, A. Greilich, D. R. Yakovlev, A. A. Kiselev, M. Bayer, V. V. Petrov, Yu. K. Dolgikh, D. Reuter, and A. D. Wieck, Phys. Rev. B **75**, 245302 (2007).
- [9] N. Porrasmonegro, C. Perdomoleiva, E. Reyesgomez, H. Brandi, and L. Oliveira, Microelectronics Journal **39**, 390 (2008), ISSN 00262692.
- [10] H. Luo, X. Qian, X. Ruan, Y. Ji, and V. Umansky, Physical Review B **80**, 2 (2009), ISSN 1098-0121.
- [11] P. J. Rizo, A. Pugzlys, A. Slachter, S. Z. Denega, D. Reuter, A. D. Wieck, P. H. M. van Loosdrecht and C. H. van der Wal, New J. Phys. **12** 113040 (2010).

- 
- [12] S. Z. Denega, T. Last, J. Liu, A. Slachter, P. J. Rizo, P. H. M. van Loosdrecht, B. J. van Wees, D. Reuter, A. D. Wieck, C. H. van der Wal, *Phys. Rev. B* **81**, 153302 (2010).
- [13] L. V. Fokina, I. A. Yugova, D. R. Yakovlev, M. M. Glazov, I. A. Akimov, A. Greulich, D. Reuter, A. D. Wieck, and M. Bayer, *Phys. Rev. B* **81**, 195304 (2010).
- [14] I. Malajovich, J. M. Kikkawa, D. D. Awschalom, J. J. Berry, and N. Samarth, *Phys. Rev. Lett.* **84**, 1015 (2000).
- [15] J.M. Kikkawa, and D. D. Awschalom, *Phys. Rev. Lett.* **80**, 4313 (1998).
- [16] R. I. Dzhioev, K. V. Kavokin<sup>1</sup>, V. L. Korenev, M. V. Lazarev, B. Ya. Meltser, M. N. Stepanova, B. P. Zakharchenya, D. Gammon, and D. S. Katzer, *Phys. Rev. B* **66**, 245204 (2002).
- [17] M. Römer, H. Bernien, G. Müller, D. Schuh, J. Hübner<sup>1</sup>, and M. Oestreich, *Phys. Rev. B* **81**, 075216 (2010).
- [18] M. Oestreich, M. Römer, R. J. Haug, and D. Hägele, *Phys. Rev. Lett.* **95**, 216603 (2005).
- [19] S. A. Crooker, L. Cheng, and D. L. Smith, *Phys. Rev. B* **79**, 035208 (2009).
- [20] G. M. Müller, M. Römer, J. Hübner, and M. Oestreich, *Phys. Rev. B* **81**, 121202(R) (2010).
- [21] W. Zawadzki, and P. Boguslawski, *Phys. Rev. Lett.* **31** 1403 (1973).
- [22] M. J. Yang, R. J. Wagner, B. V. Shanabrook, J. R. Waterman, and W. J. Moore, *Phys. Rev. B* **47**, 6807 (1993).
- [23] M. Krapf, H. Pascher, G. Weimann, and W. Schlapp, *Solid State Commun.* **78**, 459 (1991).
- [24] M. Sladkov, A. U. Choubal, M. P Bakker, A. R. Onur, D. Reuter, A. D. Wieck, and C. H. van der Wal, *Phys. Rev. B* **82**, 121308(R) (2010).
- [25] S. Z. Denega, M. Sladkov, D. Reuter, A. D. Wieck, T. L. C. Jansen, C. H. van der Wal, arXiv:1103.4307 (2011).
- [26] P. E. Hohage, G. Bacher, D. Reuter, and A. D. Wieck, *Appl. Phys. Lett.* **89**, 231101 (2006).
- [27] M. Sladkov, PhD thesis (Univeristy of Groningen, 2011).
- [28] L. Viña, S. Logothetidis, and M. Cardona, *Phys. Rev. B* **30**, 1979 (1984).

- [29] A. V. Kimel, F. Bentivegna, V. N. Gridnev, V. V. Pavlov, and R. V. Pisarev, and Th. Rasing, *Phys. Rev. B* **63**, 235201 (2001).
- [30] L. Schreiber, M. Heidkamp, T. Rohleder, B. Beschoten, G. Güntherodt, arXiv:0706.1884 (2007).
- [31] T. Lai, L. Teng, Z. Jiao, H. Xu, L. Lei, J. Wen, and W. Lin, *Appl. Phys. Lett.* **91**, 062110 (2007)
- [32] N. Delprat, B. Escudie, P. Guillemain, R. Kronland-Martinet, P. Tchamitchian, and B. Torresani, *IEEE Transactions on Information Theory* **38**, 644 (1992).
- [33] E. L. Schukin, R. Zamaraev, and L. Schukin, *Mechanical Systems and Signal Processing* **18**, 1315 (2004).
- [34] W. Zawadzki, P. Pfeffer, R. Bratschitsch, Z. Chen, S. Cundiff, B. Murnin, and C. Pidgeon, *Physical Review B* **78**, 1 (2008).
- [35] K. Litvinenko, L. Nikzad, C. Pidgeon, J. Allam, L. Cohen, T. Ashley, M. Emeny, W. Zawadzki, and B. Murnin, *Physical Review B* **77**, 2 (2008).
- [36] C. L. Yang, J. Dai, W. K. Ge, and X. Cui, *Applied Physics Letters* **96**, 152109 (2010).

# Summary

The research presented in this thesis aimed at improving the understanding of, and abilities to control the evolution of spin ensembles in semiconductor device structures. Various fundamental aspects of spin ensemble evolution like dephasing, decoherence, relaxation, diffusion and drift are addressed. All experiments used GaAs or GaAs/AlGaAs-based semiconductor materials and devices that were engineered at the nanoscale for obtaining properties that are advantageous for controlling coherent spin dynamics. These GaAs-based systems provide interesting test systems since they combine the highest available material quality, a very advanced level of possibilities for device processing and engineering, and strong optical transitions across the semiconductor bandgap that obey clear selection rules with respect to optical polarization and spin. Progress with this research is relevant for realizing new spintronic- and quantum-information functionalities.

The work aimed at answering questions and realizing new proof-of-principle demonstrations in this field. The focus was on using the advantages of ultrafast optical pump-probe studies, which was a well-established technique at the start of this thesis work. Thus, the goal was to apply this for the first time to studies of the spin dynamics that is specific for devices structures, rather than studies on bulk materials, and several interesting results in this direction were obtained. However, in the course of this work, several experiments led to observations that pointed out that the fundamental understanding of the underlying physical mechanisms was –despite the large body of earlier work on bulk materials– in fact incomplete, or even to observations that were in conflict with the established descriptions. On these occasions the reported work aimed at characterizing and understanding these new observations.

The research gave results in three areas:

*1) Suppressed spin dephasing for mobile electrons in wire structures*

The research obtained results that showed that spin dephasing due to spin-orbit interactions for electrons in wires can be suppressed by engineering of the var-

ious spin-orbit interaction terms. This effect was predicted for wires made of two-dimensional electron systems, and we demonstrated this effect. An unexpected observation was that it also occurs for wires from materials with a three-dimensional electron system. The work included numerical simulations that show good agreement with the experimental observations, both for the wires with a two- and three-dimensional electron system.

*2) Spin preparation and detection for localized electron spins*

The second topic addressed in this thesis is related to obtaining fully quantum coherent behavior for the interaction between electron spins and optical preparation and detection pulses. This work used the spin state of a donor-bound electron, localized at a Si donor site in low-doped GaAs material. These were addressed as a homogeneous ensemble. The experiments demonstrated a new ultrafast method for spin preparation and spin detection with picosecond laser pulses. Notable, both for preparation and detection the method supports a complete mapping between the quantum states of optical polarization and the quantum state of the electron spins.

*3) Fully time-resolved study of the Landé  $g$  factor in  $n$ -doped GaAs materials*

The final part of this thesis presents a detailed study of the electron  $g$  factor in bulk GaAs. This study was initiated by observations of  $g$  factor values as negative as  $g = -0.48$ , while most of the established literature assumes  $g \geq -0.44$ . Further studies revealed why the observed  $g$  factor values strongly depend on the experimental parameters that are used, and identified that the unconventional  $g$  factor values around  $g = -0.48$  originate from low-energy electrons in GaAs samples where the donor states form a band.

# Samenvatting

Het onderzoek dat in dit proefschrift gepresenteerd wordt heeft tot doel het begrijpen en controleren van de evolutie van spin ensembles in halfgeleider device structuren. Verschillende fundamentele eigenschappen van de evolutie van spin ensembles, zoals defasering, decoherentie, relaxatie, diffusie en drift worden behandeld. In alle experimenten zijn op GaAs of GaAs/AlGaAs gebaseerde devices gebruikt. Deze zijn op nanoschaal bewerkt, opdat ze over eigenschappen beschikken die voordelig zijn voor het controleren van coherente spindynamica. Deze systemen vormen interessante testsystemen, omdat ze de best beschikbare materiaalkwaliteit en een zeer geavanceerd niveau van device fabricage combineren met sterke optische transitie over de bandkloof. Deze transitie zijn onderworpen aan strenge selectieregels met betrekking tot optische polarisatie en spin. Voortgang in deze tak van onderzoek is relevant voor het realiseren van nieuwe functionaliteit in de spintronica en kwantum informatietechnologie.

Dit werk richt zich op het beantwoorden van vragen en het realiseren van nieuwe experimentele ontwerpen in dit veld. De focus ligt op het gebruik van de voordelen van optische studies met ultrasnelle laserpulsen voor preparatie en detectie van spinpolarisatie, wat ten tijde van de aanvang van dit werk reeds een goed ontwikkelde techniek was. Het doel was om dit voor het eerst toe te passen op studies van spindynamica die specifiek optreedt in device structuren, en inzicht te krijgen wanneer dit afwijkt van de spindynamica in bulk materiaal. Verschillende interessante resultaten zijn behaald. Echter, enkele van de gedane experimenten leidden tot observaties die er op duiden dat het begrip van het onderliggende fysische mechanisme –ondanks de vele eerdere studies aan bulk materiaal– incompleet was, en zelfs tot observaties die in conflict zijn met de gangbare beschrijvingen. In deze gevallen heeft dit werk tot doel deze nieuwe observaties te karakteriseren en te begrijpen.

Dit onderzoek heeft tot resultaten geleid in drie deelgebieden:

1) *Onderdrukking van spin defasering van geleidingselektronen in draadstructuren*

Dit onderzoek heeft geleid tot resultaten die aantonen dat spin defasering door

toedoen van spin-orbitaal interactie voor elektronen in draden kan worden onderdrukt door de verschillende spin-orbitaal interactie termen te controleren. Dit effect was voorspeld voor draden van twee-dimensionale elektronensystemen en is door ons gedemonstreerd. Een onverwachte observatie is dat het effect ook optreedt voor draden van drie-dimensionale elektronensystemen. Dit werk bevat numerieke simulaties die goede overeenkomsten vertonen met de experimentele observaties, zowel voor draden van twee- als van drie-dimensionale elektronensystemen.

*2) Spin initialisatie en detectie van gelokaliseerde elektron spins*

Het tweede onderwerp dat in dit proefschrift behandeld wordt is het verkrijgen van volledig kwantumcoherent gedrag van de interactie tussen elektron spins en optische initialisatie en detectie pulsen. In dit deel van het werk wordt de spintoestand van een donorgebonden elektron, gelokaliseerd op een Si-donor positie in lichtgedoteerd GaAs, gebruikt. Deze elektronen worden geadresseerd als een homogeen ensemble. De experimenten demonstreren een nieuwe, ultrasnelle methode voor spin initialisatie en detectie met laserpulsen. Opvallend is dat de methode een complete transformatie tussen optische polarisatie en de kwantumtoestand van de elektronspins uitvoert, voor elke mogelijke polarisatie en spintoestand, en zowel voor initialisatie als detectie

*3) Volledig tijdsopgeloste studie van de Landé g factor in elektron-gedoteerd GaAs materialen*

In het laatste deel van dit proefschrift wordt een gedetailleerde studie van de g-factor van het elektron in bulk GaAs gepresenteerd. Aanleiding voor deze studie waren observaties van g-factorwaarden zo laag als  $g = -0.48$ , terwijl de meeste toonaangevende literatuur uitgaat van  $g \geq -0.44$ . Nader onderzoek toont aan waarom de waargenomen g-factor sterk afhangt van de experimentele parameters, en laat zien dat de onconventionele g-factor waarden van  $g = -0.48$  veroorzaakt worden door elektronen met lage energie in GaAs materialen waar de donortoestanden een band vormen.

## List of publications

1. *Spin-dephasing anisotropy for electrons in a quasi-1D GaAs wire without quantum confinement*  
S. Z. Denega, O. V. Zwier, and C. H. van der Wal,  
in preparation.
2. *Optical time-resolved study of the Landé  $g$  factor in  $n$ -doped GaAs materials*  
S. Z. Denega, D. Reuter, A. D. Wieck, and C. H. van der Wal,  
in preparation.
3. *Ultrafast mapping of optical polarization states onto spin coherence of localized electrons in a semiconductor*  
S. Z. Denega, M. Sladkov, D. Reuter, A. D. Wieck,  
and C. H. van der Wal,  
submitted to Phys. Rev. Lett. (arXiv:1103.4307).
4. *Suppressed spin dephasing for two-dimensional and bulk electrons in GaAs wires due to engineered cancellation of spin-orbit interaction terms*  
S. Z. Denega, T. Last, J. Liu, A. Slachter, P. J. Rizo, P. H. M. van Loosdrecht, B. J. van Wees, D. Reuter, A. D. Wieck, and C. H. van der Wal,  
Phys. Rev. B **81**, 153302 (2010).
5. *Spin-dephasing anisotropy for electrons in a diffusive quasi-1D GaAs wire*  
J. Liu, T. Last, E. J. Koop, S. Denega, B. J. van Wees and C. H. van der Wal,  
J. Supercond. Novel Magn. **23**, 11 (2010).
6. *Optical probing of spin dynamics of two-dimensional and bulk electrons in a GaAs/AlGaAs heterojunction system*  
P. J. Rizo, A. Pugzlys, A. Slachter, S. Z. Denega, D. Reuter, A. D. Wieck,  
P. H. M. van Loosdrecht, C. H. van der Wal,  
New J. Phys. **12**, 113040 (2010).



# Curriculum Vitae

Sergii Zinoviyovych Denega

24-06-1983      Born in Khmelnytskyi, Ukraine

## Education

- 1991–1998      Lyceum 17, Khmelnytskyi, Ukraine
- 1998–2001      Ukrainian physical-mathematical lyceum of  
Taras Shevchenko University of Kiev, Ukraine
- 2001–2005      BSc in physics and applied physics,  
Faculty of Radiophysics,  
Taras Shevchenko University of Kiev, Ukraine
- 2005–2007      MSc in physics and applied physics (*cum laude*),  
Faculty of Radiophysics,  
Taras Shevchenko University of Kiev, Ukraine  
under supervision of dr. E. N. Smirnov and dr. S. O. Kolenov,  
Subject: Spatial spectrum of diffraction in acousto-optic devices  
with frequency modulated driving.
- 2007–2011      PhD research at the University of Groningen in the  
group of prof. dr. ir. B. J. van Wees and prof. dr. ir. C. H. van der Wal,  
under supervision of prof. dr. ir. C. H. van der Wal.  
Subject: Coherent optical control and manipulation of electron spin  
ensembles in semiconductor structures.



# Acknowledgements



